ERDC/GSL TR-20-36

Geotechnical and Structures Laboratory

US Army Corps
of Engineers®
Engineer Research and
Development Center

ERDC
ENGINEER RESEARCH & DEVELOPMENT CENTER

Magnetorheological Composite Materials (MRCMs) for Instant and Adaptable Structural Control

Travis L. Thornell, Charles A. Weiss, Jr., Sarah L. Williams, Jennifer A. Jefcoat, Zackery B. McClelland, Todd S. Rushing, and Robert D. Moser

November 2020

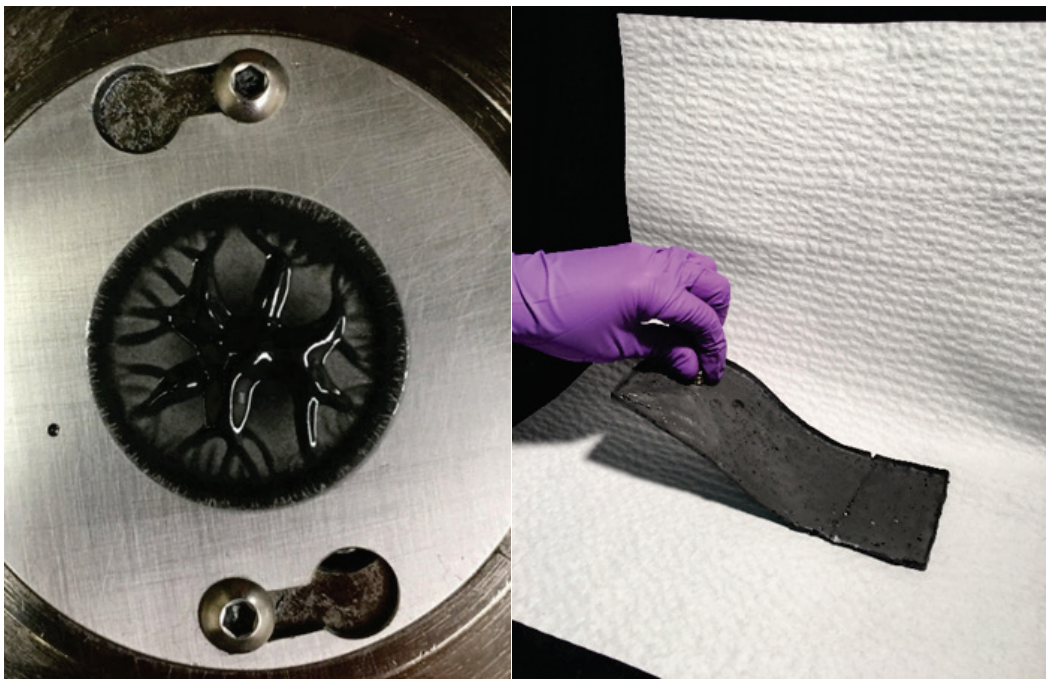

The U.S. Army Engineer Research and Development Center (ERDC) solves the nation's toughest engineering and environmental challenges. ERDC develops innovative solutions in civil and military engineering, geospatial sciences, water resources, and environmental sciences for the Army, the Department of Defense, civilian agencies, and our nation's public good. Find out more at www.erdc.usace.army.mil.

To search for other technical reports published by ERDC, visit the ERDC online library at https://erdclibrary.on.worldcat.org/discovery.

ERDC/GSL TR-20-36
November 2020

Magnetorheological Composite Materials (MRCMs) for Instant and Adaptable Structural Control

Travis L. Thornell, Charles A. Weiss, Jr., Sarah L. Williams, Jennifer A. Jefcoat, Zackery B. McClelland, Todd S. Rushing, and Robert D. Moser

Geotechnical and Structures Laboratory
U.S. Army Engineer Research and Development Center
3909 Halls Ferry Road
Vicksburg, MS 39180-6199

Final report

Prepared for U.S. Army Corps of Engineers
Washington, DC 20314-1000

Under Project 61102/T22/01, "Geological and Structural Materials Science Basic Research"

Abstract

Magnetic responsive materials can be used in a variety of applications. For structural applications, the ability to create tunable moduli from relatively soft materials with applied electromagnetic stimuli can be advantageous for light-weight protection. This study investigated magnetorheological composite materials involving carbonyl iron particles (CIP) embedded into two different systems. The first material system was a model cementitious system of CIP and kaolinite clay dispersed in mineral oil. The magnetorheological behaviors were investigated by using parallel plates with an attached magnetic accessory to evaluate deformations up to 1 T. The yield stress of these slurries was measured by using rotational and oscillatory experiments and was found to be controllable based on CIP loading and magnetic field strength with yield stresses ranging from 10 to 104 Pa. The second material system utilized a polystyrene-butadiene rubber solvent-cast films with CIP embedded. The flexible matrix can stiffen and become rigid when an external field is applied. For CIP loadings of 8% and 17% vol %, the storage modulus response for each loading stiffened by 22% and 74%, respectively.

Contents

Figures and Tables

Figures

Tables

Preface

This study was conducted for the U.S. Army Engineer Research and Development Center (ERDC) Military Engineering Basic Research Program under Project 61102/T22/01, "Geological and Structural Materials Science Basic Research." The technical monitor was Dr. Travis Thornell.

The work was performed by the Concrete and Materials Branch of the Engineering Systems and Materials Division, U.S. Army Engineer Research and Development Center, Geotechnical and Structures Laboratory (ERDC-GSL). At the time of publication of this report, Mr. Christopher M. Moore was Chief, Concrete and Materials Branch; Mr. Justin S. Strickler was Chief, Engineering Systems and Materials Division; and Ms. Pamela G. Kinnebrew was the Technical Director for Military Engineering. The Deputy Director of ERDC-GSL was Mr. Charles W. Ertle II, and the Director was Mr. Bartley P. Durst.

COL Teresa A. Schlosser was the Commander of ERDC, and the Director was Dr. David W. Pittman.

1 Introduction

1.1 Background

Magnetorheological (MR) fluids, composed of ferromagnetic nano- and/or micro-particles suspended in a carrier fluid, are of interest for a broad range of applications because of their ability to transform from a flowable liquid state to a stiff solid state on the order of milliseconds when subjected to an external magnetic field. Application of a magnetic field prompts the suspended magnetic particles to move within the fluid from a relaxed, random distribution and firmly align themselves along the lines of the magnetic flux, which causes an increase in apparent viscosity (Ashour et al. 1996). Several potential applications have been identified for these smart fluids, including MR dampers (Böse and Ehrlich 2012) and MR fluid augmented protective fabric (Son and Fahrenthold 2012).

Recently, magnetorheology has been identified as a possible method to improve infrastructure performance. MR fluid sandwich panels and beams, composed of a thin MR fluid core layer encompassed by traditional face layer materials, such as metals and composites (Lara-Prieto et al. 2010; Manoharan et al. 2014; Joshi 2012), have shown promise in controlling vibration and acoustic properties in structures. Magnetorheological elastomers (MREs), composed of ferromagnetic nano- or micro-particles embedded in a stiff polymeric matrix, have also been used as a core layer to produce smart, adaptive sandwich panels and beams with promising results (Yalcintas and Dai 2004; Lee et al. 2014; Hasheminejad and Shabanimotlagh 2010). Basic composite MR fluids have been produced by adding a small volume of non-magnetic micro-particles, such as polystyrene or glass spheres, to traditional MR fluids (Popplewell and Rosensweig 1996; Powell et al. 2012) to enhance colloidal stability of the fluid and increase yield stress, and set-on-demand concrete has been investigated by adding ferromagnetic particles to cement paste during the mixing process and using an external magnetic field to influence the fresh-state properties (Nair and Ferron 2014). However, while useful for controlling the fresh-state properties of concrete, note that the dispersed magnetic particles cannot be used to influence properties of MR concrete after setting has occurred because the magnetic particles cannot freely rearrange themselves within the stiffened concrete matrix.

Both composite MR fluids and MR concrete could be considered precursors to the slurry type MRCMs proposed in this project, while MREs could be considered precursors to the proposed polymer-based MRCMs. Thus, the current project built upon fundamentals from past work in the literature with fresh, innovative ideas for a new research direction. For example, the slurry MRCMs contained a much higher volume of non-magnetic particles as compared to composite MR fluids such that the slurry MRCMs had a consistency similar to a typical mortar or concrete rather than a fluid. Additionally, infrastructure constituent materials for the non-magnetic particles were used, such as kaolinite clay, which yields an economically scalable material with sufficient workability for rapid, temporary construction and/or repair applications. The polymer-based MRCMs in this project were designed with deformable, lightweight, polymeric matrix materials as opposed to the stiff matrices that have been used for MRE design in the literature such that the polymer-based MRCMs had flexibility in the absence of an external magnetic field. These flexible polymer-based MRCMs could be used for many applications, including lightweight, portable (i.e., roll-out) airfield matting and temporary protective panels.

1.2 Objective

This research employed MR principles to produce first-of-their-kind magnetorheological composite materials (MRCMs) in which the materials' mechanical properties, shape, and position were manipulated in real time by an external magnetic stimulus. Two types of MRCMs were investigated (Table 1).

Table 1. Description of proposed MRCM types: slurry-based and polymer-based.

MRCM Type	Dispersed Phase(s)	Matrix Phase(s)
Slurry-based	Synthetic ferromagnetic nano- and/or micro-particles. Non-magnetic filler particles (e.g., sand and polymer particles).	Lightweight non-aqueous fluid, such as mineral oil. Slurry-based MRCMs have a consistency similar to a freshly mixed mortar or concrete when deactivated.
Polymer-based	Synthetic ferromagnetic nano- and/or micro-particles.	Flexible, lightweight, synthetic and/or bio-based polymer. Polymer-based MRCMs have a consistency similar to a typical polymeric composite when deactivated.

All the MRCMs investigated in this study, regardless of type, were composed of ferromagnetic nano- and/or micro-particles suspended in a non-magnetic matrix. These smart composites were highly tunable by means of an externally applied magnetic field, which prompted the particles to move from a random distribution and align themselves along the lines of the magnetic flux (Ashouret al. 1996). This rapid (on the order of milliseconds) and reversible transformation resulted in a complete reorganization of the material's microstructure, which in turn caused changes in apparent viscosity. Because of this unique ability to adjust the microstructure of the material on demand to manipulate properties, the authors hypothesized that MRCMs could gain sufficient strength and stiffness to act as load-bearing, protective materials in seconds as compared to common materials fabricated in situ (e.g., concrete), which typically require several hours and/or days to gain substantial strength and stiffness.

Impact and significance: This research introduced a novel group of smart materials that could be useful for a wide variety of military engineering applications, such as rapid temporary construction/repair, rapid protection from impact and/or explosives, and lightweight portable (i.e., rollout) airfield matting. Figure 1 shows a typical response of suspended magnetic particles in an MR material to an external magnetic field. In the following figure, it is evident that application of an external magnetic field causes the particles' magnetic dipoles to form linear structures parallel to the applied field.

Figure 1. Schematic showing the response of an MRCM to an external magnetic field.

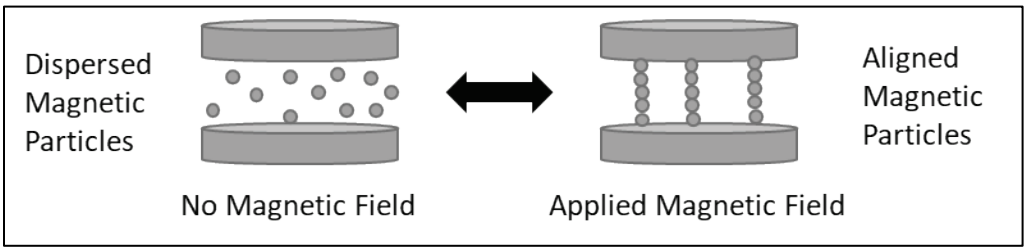

To acquire a fine-tuned understanding of the macro-scale mechanical response of MRCMs subjected to external magnetic stimuli, the team first planned to characterize and model the bonding behavior between individual ferromagnetic nanoparticles in response to changes in magnetic field strength, shape, and/or position on the nano- to micro-scale. Additionally, it is known that properties of the suspended particles in traditional MR

fluids have substantial influence over properties of the aggregate structure (Vereda et al. 2015; Sarkar and Hirani 2015; Shah and Choi 2015); thus, a key focus of this research was to determine the optimum size, gradation, concentration, and mineralogy of the dispersed magnetic nanoparticles to produce the strongest magnetized aggregate structure.

1.3 Approach

Project description: The project was divided into four tasks to be completed in a sequential fashion.

Task 1 involved characterization of candidate materials for MRCMs. This task investigated a wide range of matrix materials, non-magnetic filler particles, and dispersed ferromagnetic particles. The morphology, composition, size distributions, and magnetic properties were assessed for the various materials.

Task 2 focused on the MR behavior of slurry-based MRCMs selected from the best performers in Task 1. The MR testing was conducted by sophisticated, quantitative MR testing of the trial MRCMs using a TA Instruments Discovery Hybrid Rheometer (DHR) with an MR accessory. The MR accessory passes a current through a coil to generate a uniform magnetic field (up to 1 T*), allowing the DHR to capture changes in the material viscoelastic properties as a function of magnetic field strength and temperature. Using a parallel plate geometry, the apparent viscosity and dynamic yield stress of each MRCM, with and without an applied magnetic field of a set magnitude, were obtained from rheograms (i.e., flow curves), and viscoelasticity was characterized by using small angle oscillatory shear testing to quantify the loss modulus (i.e., viscous component) and the storage modulus (i.e., elastic component) of each MRCM with and without a magnetic field.

Task 3 investigated the use of bauxite as a supplementary magnetic material for slurry-based MRCMs. The bauxite was treated to remove

* For a full list of the spelled-out forms of the units of measure used in this document, please refer to *US Government Publishing Office Style Manual*, 31st ed. (Washington, DC: US Government Publishing Office 2016), 248-52, https://www.govinfo.gov/content/pkg/GPO-STYLEMANUAL-2016/pdf/GPO-STYLEMANUAL-2016.pdf.

alumina-based phases and enhance iron-rich phases to potentially produce higher levels of magnetizations.

Task 4 involved using polymer-based MRCM designs using the magnetic candidate selected from Task 2. The magnetic particles were embedded in a polymer matrix and characterized by using scanning electron microscopy (SEM), magnetization behaviors, and MR behaviors from 0 to 1 T, using the DHR and MR accessory. Magneto-sweeps, strain sweeps, and frequency sweeps were performed to understand oscillatory behaviors of the polymer-MRCMs.

2 Experimental Methods

For formulations of MRCMs, initial magnetic and non-magnetic materials were selected to determine optimum particle size, gradation, and mineralogy to yield high performing MRCMs.

2.1 Materials

Candidates for MRCM synthesis and formulations were selected from varying mineralogies and particle sizes. Carbonyl iron particles (CIP) (BASF Grade SM), iron for analysis (IFA) (EMD Millipore Sigma), iron electrolytic powder (IEP) (Fisher Chemical), kaolinite (Fluka Analytical), mineral oil (HyDurance AW NZ fluid 32, Chevron), magnetite, hematite, and sand were used as received. For polymer MRCMs, polystyrene-butadiene rubber (SBR) copolymer (23 wt. % styrene) was purchased from Scientific Polymer Products. National Institute of Standards and Technology (NIST) standard reference material (SRM) of bauxite originating from Arkansas (69b-Ark), Australian (600-Aus), Dominican (697-Dom), Jamaican (698-Jam), and Surinam (696-Sur) were obtained from Sigma Aldrich. Bauxite samples were treated under the following procedure: 20 g of bauxite was mixed in 150 ml of 3M NaOH* solution and autoclaved at 121 °C at 15 psi for 60 min. The mixture was then vacuum filtered through a 0.2 μm filter. The solids collected in the filter were dried at 50 °C for 24 hr before being sieved though a No. 325 sieve.

2.2 Magnetorheological composite material (MRCM) synthesis

Slurry-based MRCMs were formulated to have similar characteristics to a freshly mixed cement paste when under no applied field. To achieve this, formulations were prepared at 60 wt. % solids (CIP + kaolinite) within a 40 wt. % nonmagnetic carrier fluid of mineral oil. Samples were combined into 20 ml speed mixing cups and mixed by using a speed mixer (FlackTek, Inc.) at 3,500 RPM for 3 min.

* For a full list of the spelled-out forms of the chemical elements used in this document, please refer to *US Government Publishing Office Style Manual*, 31st ed. (Washington, DC: US Government Publishing Office 2016), 265, https://www.govinfo.gov/content/pkg/GPO-STYLEMANUAL-2016/pdf/GPO-STYLEMANUAL-2016.pdf.

Polymer-based MRCMs were mixed based on the following procedure. A polymer solution of 15 wt. % was prepared by dissolving polymer in toluene. The solution was mixed by using the same speed mixer as above for 10 cycles of 3 min and 3,500 RPM each. The CIP was then mixed into the polymer solution and speed mixed for 1 cycle of 3 min at 3,500 RPM. The solution was placed into a vacuum oven to remove air bubbles. The solution was cast into a silicon mold or aluminum dish and placed into an oven at 60°C for at least 6 hr. Discs were cut out with diameters of 20 mm and thicknesses of 1 mm.

2.3 Characterization methods

2.3.1 Particle size analysis

Particle size analyses were performed by using a Malvern Mastersizer 3000 with laser diffraction capable of measuring particles with diameters ranging from 0.01 to 3,500 μm. Samples were dispersed in deionized water for testing.

2.3.2 Scanning electron microscopy (SEM)

SEM was performed in this study by using a low-pressure SEM (Nova NanoSEM 630, FEI Co.), which eliminated the needs for sample preparation and application of a conductive coating.

The Nova NanoSEM 630 has a field-emission gun with a tungsten filament. The imaging conditions employed an accelerating voltage of 25 to 30 KeV and 1.69 mA with a resolution of 1.6 nm at 1 kV. Images of these samples were collected over a period of 30 sec and stored as 2 MB TIF files.

2.3.3 X-ray diffraction

The mineralogies of the materials used in this study were determined by using X-ray diffraction (XRD) analysis. Bulk XRD tests were conducted on each of the samples, using the material as received. In preparation for XRD analysis, if needed, a split portion of the sample was ground in a Pulverisette (Fritsch Co., Idar-Oberstein, Germany) and passed through a 45 μm (No. 325) sieve. Random orientation powder mounts of bulk samples were analyzed by using XRD to determine the mineral constituents present in each sample. XRD patterns were collected from an X-Pert Pro Multipurpose Powder Diffractometer system that used standard techniques for phase identification (Panalytical, Inc.). The run conditions included

Co-Kα radiation and scanning from 2 to 70 $^{o}2\theta$ with collection of the diffraction patterns accomplished by using the personal computer-based Windows version of X-Pert Pro Data Collector and analysis of the patterns by using the Jade2010 program (Materials Data, Inc.).

2.3.4 Shear rheology

MR testing was performed on a TA instruments Discovery Hybrid Rheometer Series 2 (DHR-2) with MR accessory. The MR accessory allowed for applied fields of up to 1 T with an external hall probe to monitor real-time magnetic fluxes. Experiments were conducted with a 20 mm top parallel plate test geometry with a gap of 1 mm. To minimize wall slip effects for slurry-based MRCMs, 600-grit sandpaper was adhered to the top plate.

All slurry-based MRCMs samples were pre-sheared at a shear rate ($\dot{\gamma}$) of 1 s^{-1} for 30 sec before testing to create homogenous samples. Testing with polymer-based MRCMs was conducted on discs, with an applied normal force of 4 N to reduce slipping of the samples. For magnetic time sweeps, strain and angular frequency were held constant at 0.1 % and 1 Hz, respectively, while the magnetic flux was ramped from 0 to 1 T. For determination of the linear viscoelastic regime (LVE), strain amplitude sweeps were performed at constant angular frequency of 10 rad/s, and strain was varied from 0.01% to 100%. Frequency sweeps to understand the time-dependent deformation behavior under various fields were performed under strain values within the LVE (determined from amplitude sweeps) with frequency being varied from 100 to 0.01 rad/s. For rotational experiments, flow curves were performed under constant magnetic fields, and the shear rate was varied from 0.1 to 100 s^{-1}.

2.3.5 Magnetic property characterization

The vibrating sample magnetometer (VSM) module on Versalab (Quantum Design) was used to characterize magnetic properties of MRCMs. For candidate materials for MRCM formulation, VSM experiments were conducted in powder cells. VSM experiments on polymer MRCMs were performed by using a small piece of the composite adhered to the brass tube. Magnetic properties were collected from a cycle of $\pm$ 30,000 Oe to determine magnetic moment (emu). Data were then normalized by the weight of each sample to obtain magnetization values in the units of emu/gram.

2.3.6 Thermogravimetric analyses (TGA)

TGA were performed on CIP, control SBR, and 8 and 17 CIP-SBR polymer MRCMs to see the degradation effects of the polymer. Using a Netzsch Simultaneous Thermal Analyzer 449 F1 Jupiter and a Tg sample carrier, samples were weighed into tared aluminum oxide crucibles and exposed to a temperature ramp procedure in a silicon carbide furnace. The test parameters involved a linear temperature increase carried out from ambient temperature to 1,000 °C at a rate of 10 °C/min in an air environment. Results were then analyzed to see effects of degradation due to CIP addition.

3 MRCM Constituent Selection

3.1 Morphological characterization

SEM was used to understand morphological characteristics of candidate MRCMs. For each material, SEM images were taken at 1,500x and 20,000x magnifications to see changes in the size scale of groups of particles and of individual particles. Figure 2 and Figure 3 illustrate the similar size characteristics of CIP and IFA particles. In both materials, the particles had uniform appearance and were spherical in nature. IEP images are presented in Figure 4 and show that these particles had irregular, non-spherical shapes with smooth surfaces. The angular and plate-like characteristics of kaolinite clay are shown in Figure 5. To probe the morphology of sand, magnifications of 150x and 1,000x in Figure 6 were used to capture the large rounded particle characteristics. Hematite was observed to be angular in particle shape and porous, as shown in Figure 7. The iron ore of magnetite shown in Figure 8 had angular shape with a range of observable particle sizes. Table 2 summarizes the characteristics of the materials for preparation of MRCMs.

Figure 2. SEM images of CIP: (left) 1,500x magnification and (right) 20,000x magnification.

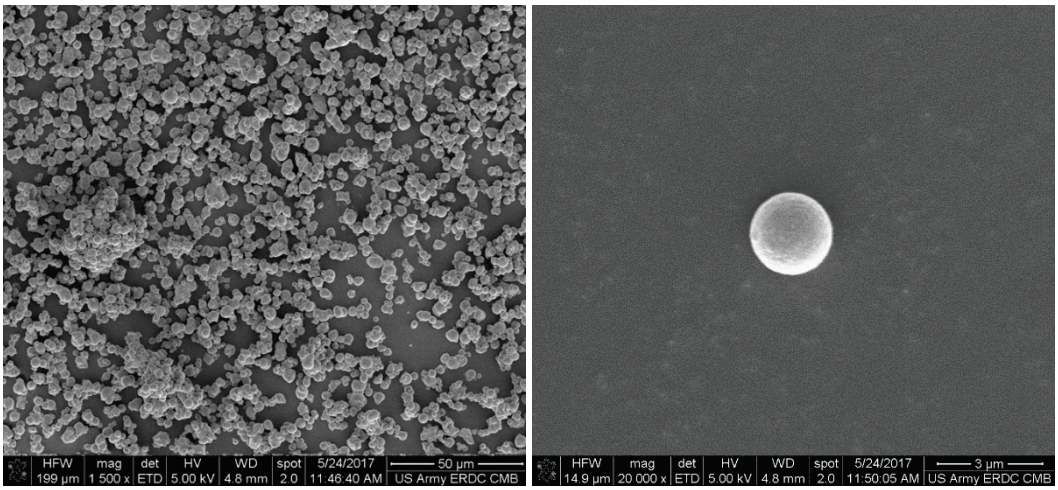

Figure 3. SEM images of IFA: (left) 1,500x magnification and (right) 20,000x magnification.

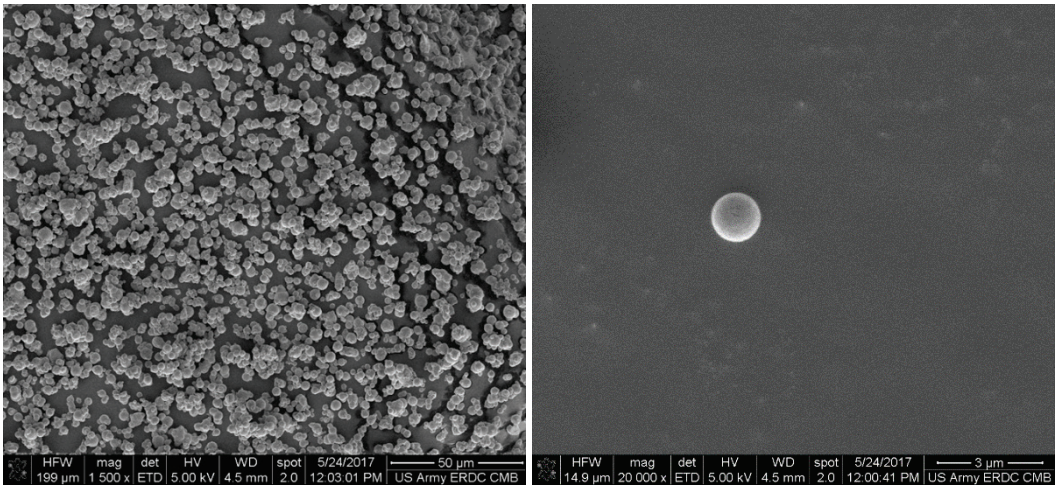

Figure 4. SEM images of iron electrolytic powder: (left) 1,500x magnification and (right) 20,000x magnification.

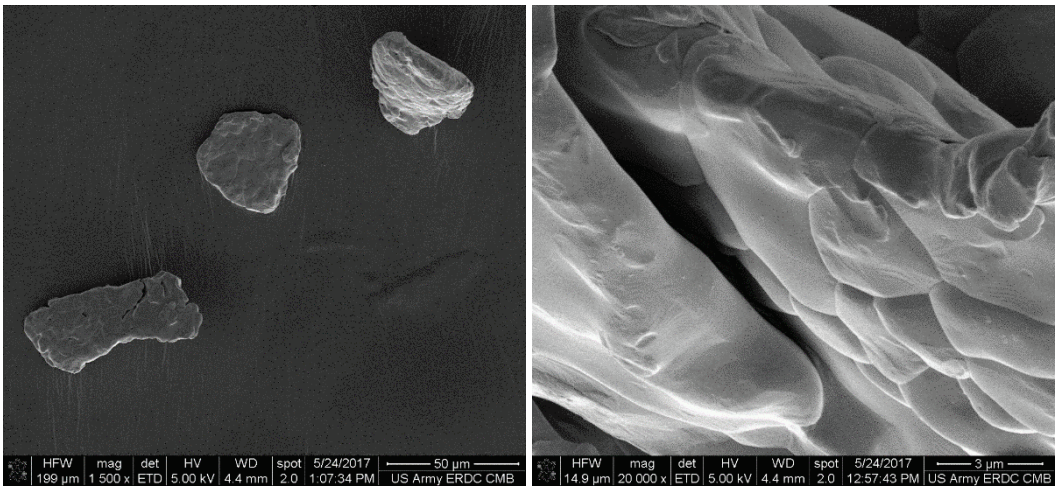

Figure 5. SEM images of kaolinite: (left) 1,500x magnification and (right) 20,000x magnification.

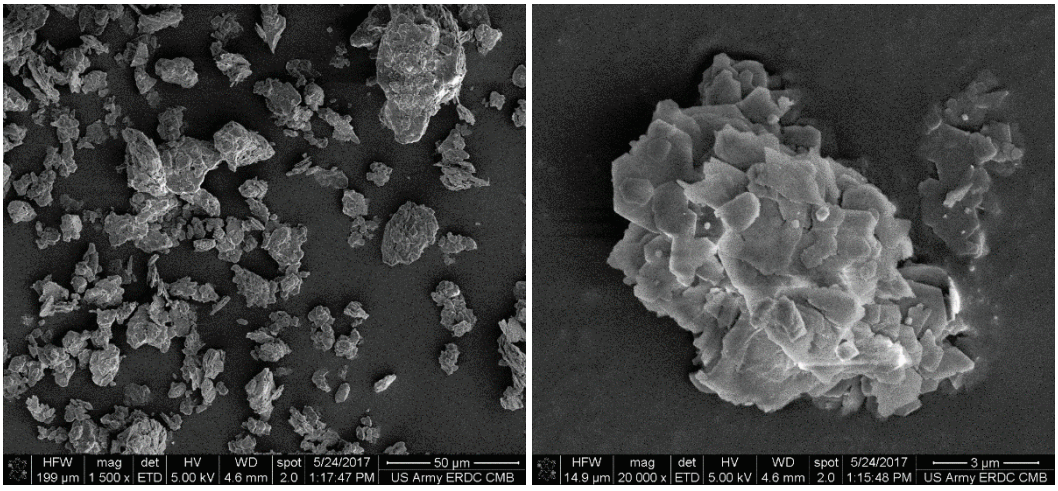

Figure 6. SEM images of sand: (left) 150x magnification and (right) 1,000x magnification.

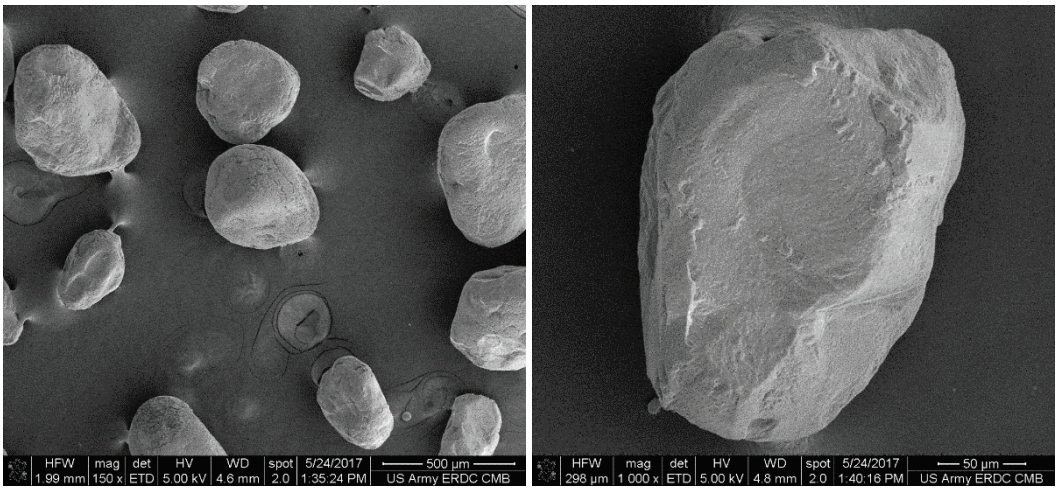

Figure 7. SEM images of hematite: (left) 1,500x magnification and (right) 20,000x magnification.

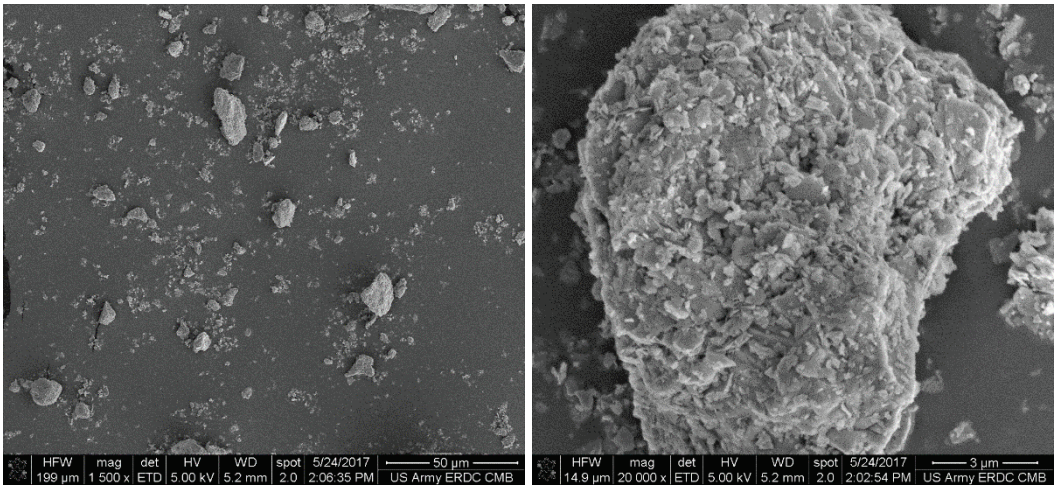

Figure 8. SEM images of magnetite: (left) 1,500x magnification and (right) 20,000x magnification.

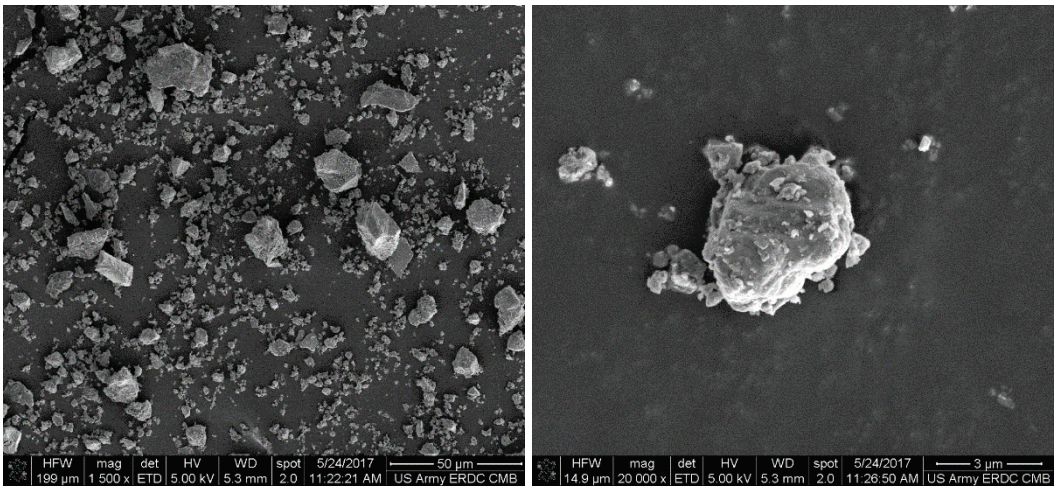

Table 2. Summary of particle characteristics.

Magnetic Powder	Characteristics
CIP	Spherical, uniform
IFA	Spherical, uniform
IEP	Irregular, smooth
Kaolinite	Angular, plate-like
Sand	Rounded, large
Hematite	Angular, porous
Magnetite	Angular, non-porous

3.2 Particle size

Particle size characterization of the candidates for MRCM was performed to understand size distribution of the particles. Figure 9 illustrates the particle sizes of the various materials at median diameter (D50). The particle size distributions of each material can be found in Appendix B. Sand had the largest median particle size at 348.92 ± 17 µm, as expected from SEM observations. IEP had a median size of 79.99 ± 0.78 µm. The other particles that were studied had lower particle sizes, which would be needed for proper MRCM formulation. Hematite, with the angular and porous characteristics, had a very large particle size distribution with a median size of 20.84 ± 2.19 µm. Magnetite had a median size of 11.54 ± 0.50 µm, but large degrees of agglomeration can be seen in both SEM images and size distribution data. Similarly, kaolinite had extensive aggregation but had a median size of 10.37 ± 0.33 µm. The spherical particles of CIP and IFA had very similar median particle sizes of 8.22 ± 0.04 µm and 8.62 ± 0.02 µm, respectively.

Figure 9. Median particle diameters of candidate materials (laser diffraction).

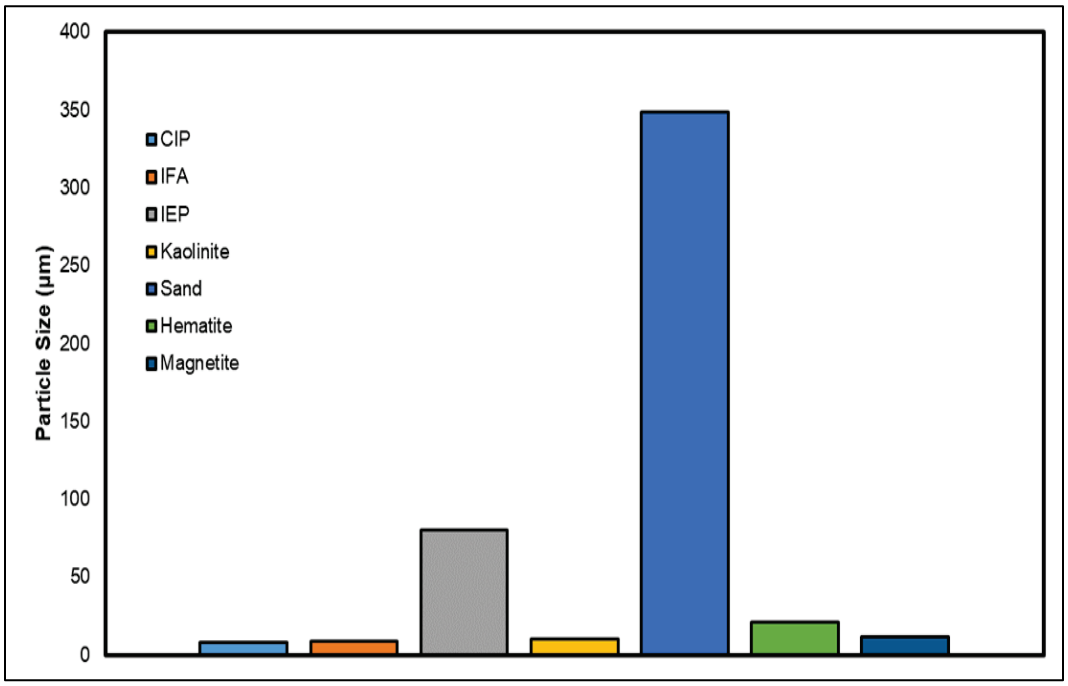

3.3 X-ray diffraction

Quantitative XRD analysis of each material elucidated the amount and type of mineral phases present (Table 3). The analyses were performed to verify the sample mineralogy and to document any accessory minerals present.

The outputs of all the non-metal samples are in Appendix C. XRD patterns on the metal samples (CIP, IFA, and IEP) were run only from 5 to 75 $^{o}2\theta$, and as such, there was only one diffraction peak for the material in this range. Therefore, the patterns were not included in this report.

Table 3. Quantitative X-ray diffraction analysis of samples examined in this study.

Sample	Type	Phases	Amount (%)	Phases	Amount (%)	Phases	Amount (%)	Phases	Amount (%)
A1-1	CIP	Iron	100						
A1-2	CIP	Iron	100						
A2-1	IFA	Iron	100						
A2-2	IFA	Iron	100						
A3-1	IEP	Iron	100						
A3-2	IEP	Iron	100						
A4-1	Hematite	Hematite	74.1	Quartz	15.5	Mica	10.3	Kaolinite	<1
A4-2	Hematite	Hematite	82.1	Quartz	13.4	Mica	4.3	Kaolinite	<1
A5-1	Magnetite	Magnetite	96.4	Hematite	2.1	Quartz	<1	Kaolinite	1.5
A5-2	Magnetite	Magnetite	97.8	Hematite	2.1	Quartz	<1	Kaolinite	<1
A6-1	Kaolinite	Kaolinite	90.3	Quartz	9.7	Mica	<1		
A6-2	Kaolinite	Kaolinite	90.7	Quartz	9.2	Mica	<1		
A7-1	Sand	Quartz	100						
A7-2	Sand	Quartz	100						

3.4 Magnetic characterization

Experiments conducted using the VSM instrument measure the magnetization of a sample over a range of magnetic field strength. In other words, the VSM instrument measures the degree to which a sample material is influenced by the field. VSM data for the candidates for MRCM formulations are presented in Figure 10. IFA and CIP exhibited the highest magnetization values of 218.61 and 216.58 emu/gm, respectively. IEP also had a relatively high magnetization of 192.05 emu/gm. The mineral magnetite had a saturation magnetization of 80.4 emu/gm. The lowest values of magnetization at 300 K were hematite, kaolinite, and sand at 0.813, 0.009 and 0.01 emu/gm, respectively. Higher magnetization values suggest that use of such materials in MRCMs should result in a stronger response to the magnetic stimulus.

Figure 10. Magnetization curves for candidate materials.

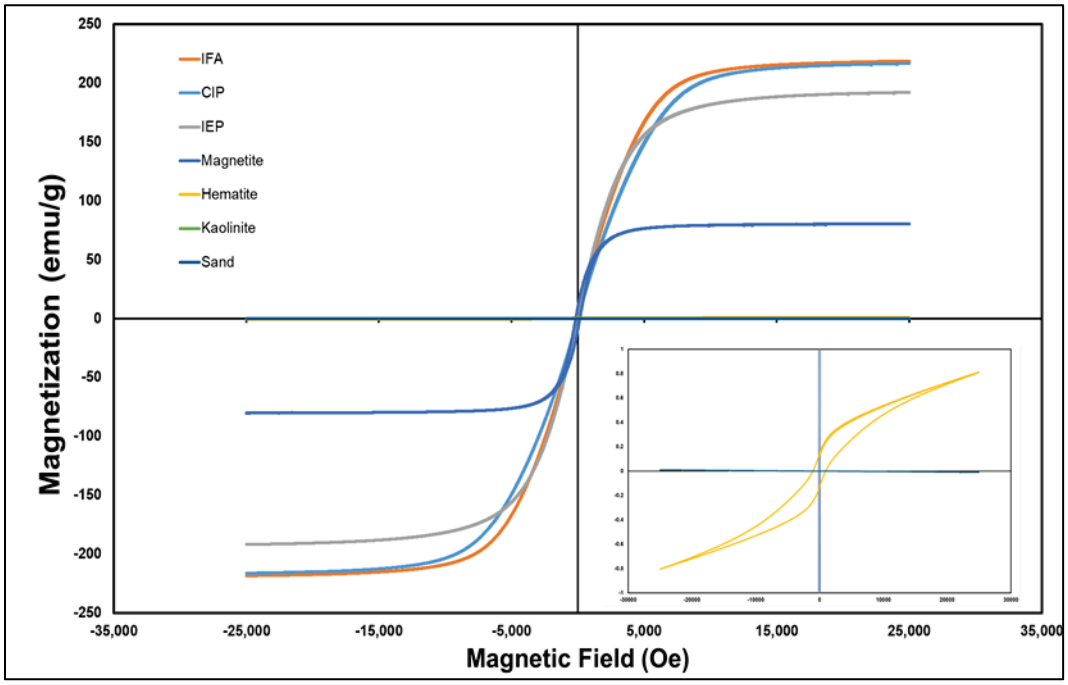

4 Magnetorheological Characterization of Slurry-Based MRCMs

Slurry-based MRCMs have been used for a variety of applications from dampening (Kwon et al. 2015) to on-demand setting concrete (Nair and Ferron 2014). These MRCMs take advantage of fluidlike or pastelike characteristics in ambient conditions. When exposed to an external magnetic field, the dispersed magnetic particles within the suspension or slurry begin to align themselves into chainlike conformations. This alignment creates a second, more ordered structure within the system, as shown in Figure 1 and previously described.

Studies on CIP suspensions in mineral oil or other viscous liquids have been reported throughout the literature. With the high density of CIP compared to the continuous phase, sedimentation and stability have been problematic. Additives such as halloysite (Kwon et al. 2015), sepiolite (Dong et al. 2018), attaapulgite (Chae et al. 2015), and polymers (Chao et al. 2017; Cvek et al. 2015; Chin et al. 2001) have been employed to create more stable and reversible composite materials.

For structural applications, the ability of a material to stiffen quickly without long curing times is highly desirable. For protection and transportation, this can allow for faster construction in expeditionary or temporary situations. The evolution of yield stress is an important characteristic of cement paste and concrete mixtures as it determines how much force is needed for the material to flow at a given time, and the workability is time dependent. A tunable yield stress could be very advantageous; a suspension or paste could be designed to have a low yield stress (high flow) during mixing and delivery operations, then, by application of a magnetic field, be instantly switched to having high yield stress (low or no flow) to retain its shape until solidification occurs via the hydration reaction. Slurry-based MRCMs have yield stress responses that are dependent on magnetic particle content and magnetic fields (Yang et al. 2009; Caballero-Hernandez et al. 2017).

Various models are used to model the shear stress response and yield stress, such as the Bingham model and Herschel-Bulkley (HB) model (Cvek et al. 2016; Seo et al. 2016). The HB model is shown in Equation 1.

$$\tau = \tau_y + \eta\dot{\gamma}^n \quad (1)$$

where

τ = shear stress (Pascals (Pa))
τ_y = yield stress (Pa)
K = consistency index (or η for viscosity) (Pa*s)
$\dot{\gamma}$ = shear rate (s^{-1})
n = power-law exponent.

Clay additives with irregular and angular shapes can be used as surrogate portland cement particles in slurries to help researchers understand how rheological properties change under applied magnetic fields. For the slurries in this study, kaolinite was selected as the clay, CIPs were the magnetic particles, and mineral oil was the continuous phase. To model freshly mixed cement pastes (water-to-cement ratio of 0.4), mineral oil was held constant at 40 wt. % of the total slurry, and kaolinite and CIP were varied from 20-40 wt. % respective to overall slurry weight giving samples of 20 wt. % kaolinite/40 wt. % CIP, 30 wt. % kaolinite/30 wt. % CIP, and 40 wt. % kaolinite/20 wt. % CIP.

4.1 Magnetic time sweeps

The oscillatory behavior from magnetic time sweeps of the slurry-based MRCMs are shown in Figure 11. In these tests, strain and angular frequency were held constant at 0.1% and 10 rad/s, respectively, while the external magnetic field was increased to 1 T. The viscoelasticity of each slurry was observed through the storage modulus (G') and loss modulus (G") for the three formulations of CIP/kaolinite. The storage modulus described the solidlike elastic response, and the loss modulus described the liquidlike viscous response.

Figure 11. Magnetic sweeps of slurry-based MRCMs of 20-40 wt. % CIP at magnetic fields from 0-1 T.

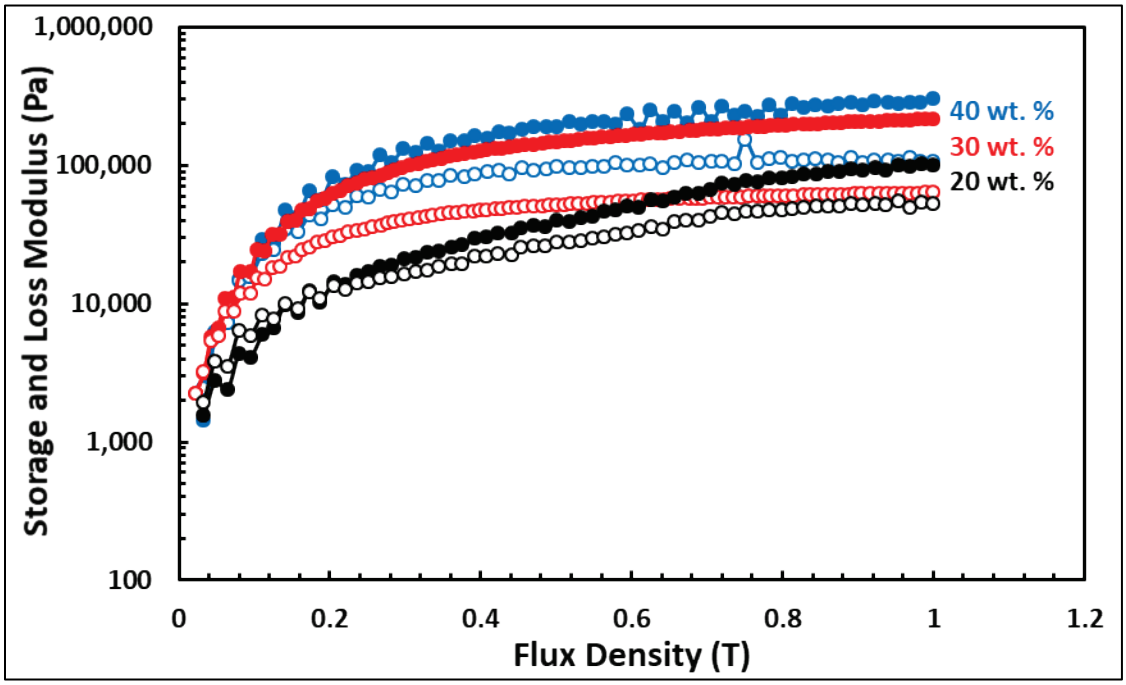

At low flux densities (low magnetic fields), the storage and loss moduli responses followed similar trends among the three formulations with G" > G'. In this regime, the viscous component dominated, and the slurries were pourable and spreadable. As the magnetic field was intensified, both G' and G" increased for all the formulations, and G' eventually became greater than G", indicating slurry stiffening. The crossover in viscoelasticity for the 40 and 30 wt. % CIP slurries occurred before the 20 wt. % CIP slurry, signifying alignment of the CIP within the matrix. The overall magnitude of G' and G" was also shown to be dependent on the amount of CIP within the slurry. The 40 wt. % CIP slurry had the highest modulus responses, as G' increased by almost three orders of magnitude due to the mobility of the CIP within the mineral oil matrix. For the 40 wt. % CIP, the slurries were relatively fluid with only 20 wt. % kaolinite. As the magnetic field was increased, the particles were able to align together to create a stiffened slurry. Similarly, the 30 wt. % CIP slurry with 30 wt. % kaolinite had very large increases in G' and G" responses. The 20 wt. % CIP with 40 wt. % kaolinite illustrated similar trends to the other slurries, but the magnitude of the response was observably lower. The diminished response was due to two factors: (1) higher clay content reduced mobility and alignment of the CIP and (2) lower overall CIP content led to less magnetic character in this slurry.

4.2 Flow curves

The rotational behaviors of the slurry-based MRCMs were investigated by obtaining flow curves using the DHR. Based off work on clay (Rich et al. 2012) and cement rheology (Burroughs et al. 2019), flow curves were measured under increasing (loading) and decreasing (unloading) shear rate conditions while decreasing the shear rate from 100 to 0.01 s^{-1}.

The shear stress response of the lowest CIP content slurry of 20 wt. % CIP and 40 wt. % kaolinite under magnetic fields of 0, 0.1, 0.3, 0. 5, and 1 T are shown in Figure 12 The magnitude of the shear stress response increased as a function of the applied magnetic field. Fitting the HB model to the shear stress response helped to analyze the results. The HB model provided acceptable fits to data at no and low magnetic fields but was only adequate at shear rates greater than 1 s^{-1} for fields greater than 0.3 T. Fitting parameters of the HB model are summarized in Appendix B. The experimental yield stresses from the lowest applied shear rate of 0.01 s^{-1} are shown in Table 4.

Figure 12. Flow curves of 20 wt. % CIP/40 wt. % kaolinite at various magnetic fields.

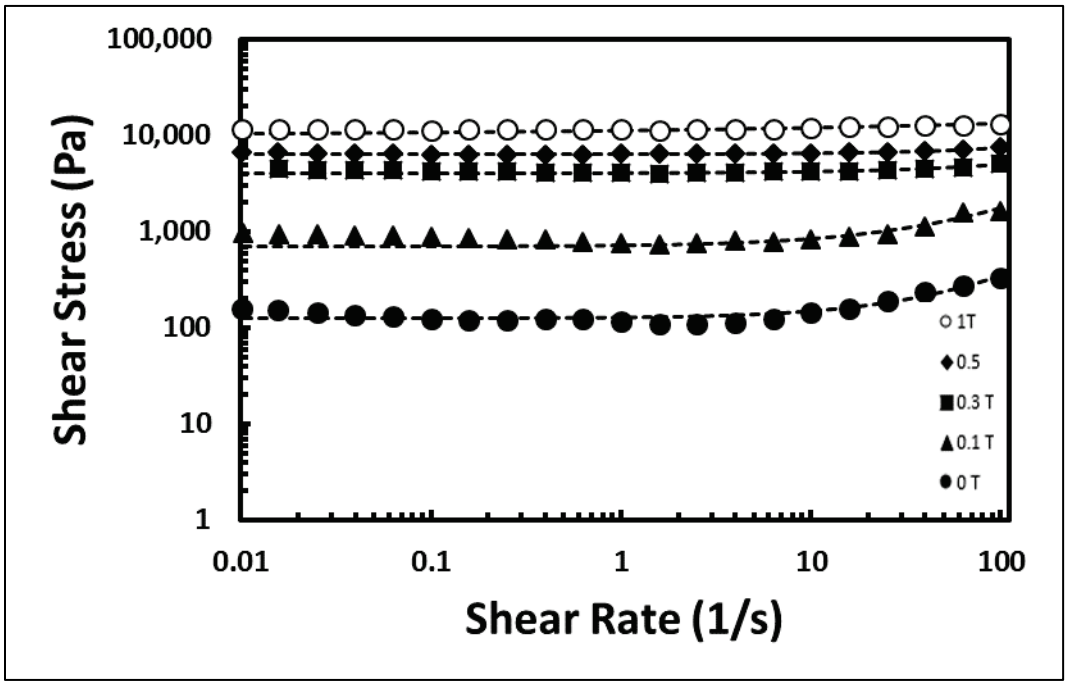

Table 4. Experimental yield stress of 20 wt. % CIP/ 40 wt. % kaolinite at various magnetic flux densities.

Field (T)	Yield Stress (Pa)
0	125
0.1	706
0.3	4,019
0.5	6,422
1	10,005

Figure 13 and Figure 14 show the shear stress response of the 30 wt. % CIP and 30 wt. % kaolinite and 40 wt. % CIP and 20 wt. % kaolinite slurries, respectively, at magnetic fields of 0, 0.1, 0.3, 0.5, and 1 T. Similarly, to the 20 wt. % CIP slurry, large increases in the response from 0 T to 0.1 T were observed as the CIP aligned in the slurry due to the high magnetization of the particles. The stiffening responses continued as increasing magnetic fields were applied. The experimental yield stresses are summarized in Table 5 and Table 6.

Figure 13. Flow curves of 30 wt. % CIP/30 wt. % kaolinite at various magnetic fields.

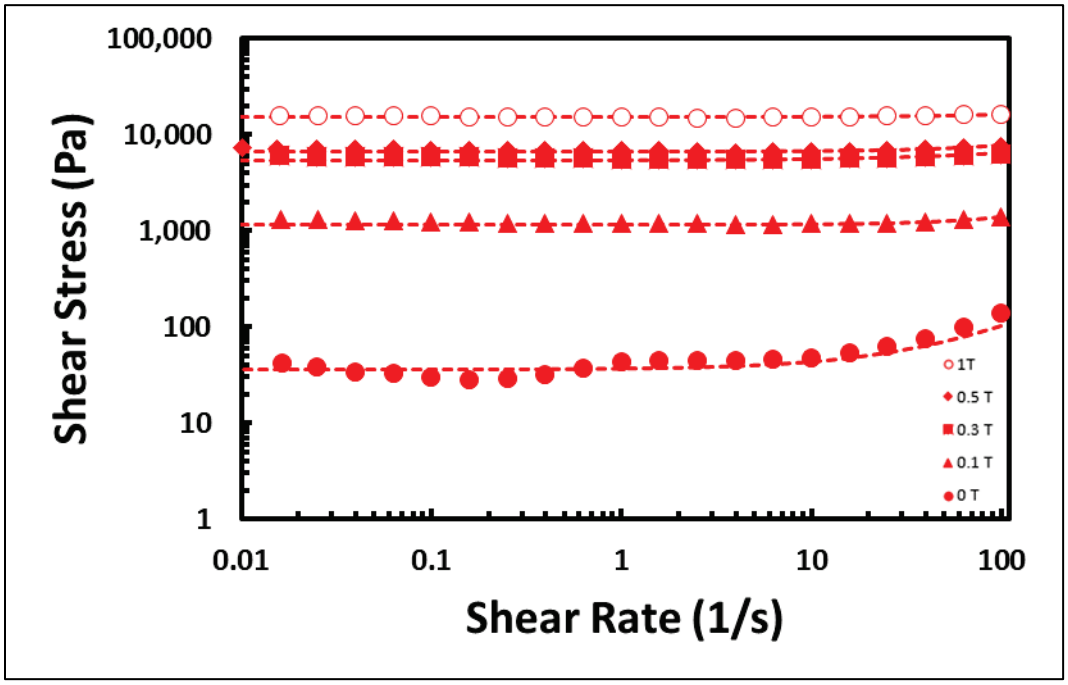

Table 5. Experimental yield stress of 30 wt. % CIP/30 wt. % kaolinite at various magnetic flux densities.

Field (T)	Yield Stress (Pa)
0	36
0.1	1,173
0.3	5,402
0.5	6,607
1	15,119

Figure 14. Flow curves of 40 wt. % CIP/20 wt. % kaolinite at various magnetic fields.

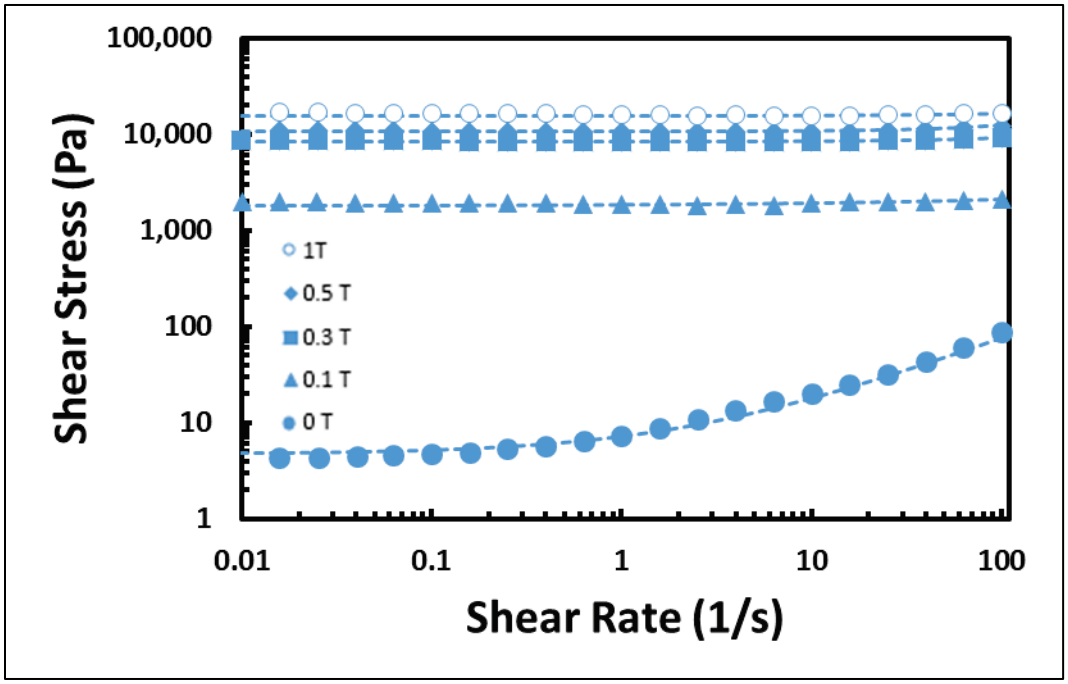

Table 6. Experimental yield stress of 40 wt. % CIP/ 20 wt. % kaolinite at various magnetic flux densities.

Field (T)	Yield Stress (Pa)
0	5
0.1	1,770
0.3	8,294
0.5	10,655
1	15,441

4.3 Yield stress as a function of CIP content

The experimental yield stress as a function of CIP wt. % for the three formulations at magnetic fields of 0, 0.1, 0.3, 0.5, and 1 T are shown in Figure 15. At no magnetic field, the yield stress response was dependent on the amount of kaolinite within the slurry, as indicated by the 20 wt. % CIP (40 wt. % kaolinite) slurry having the highest experimental yield stress. As the magnetic field was applied, the dependence on the clay for the yield stress gave way to the amount of CIP within the slurries. The 40 wt. % CIP slurry had the highest yield stresses under magnetic fields.

Figure 15. Experimental yield stress as a function of CIP loading at various magnetic fields.

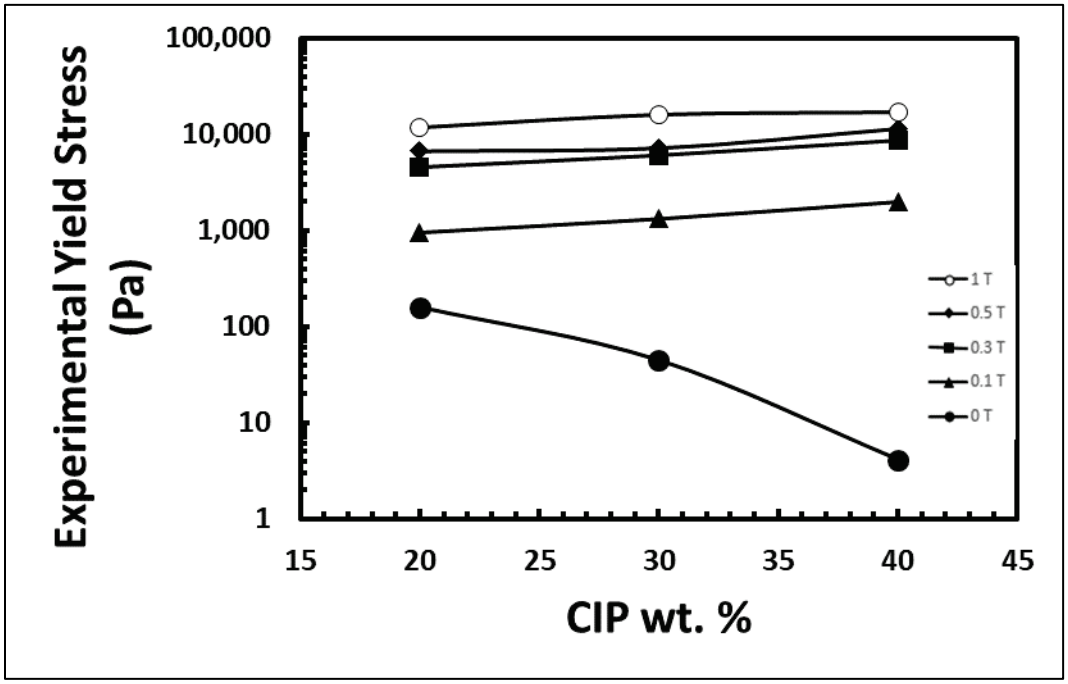

5 Structural and Magnetic Characterization of Bauxite

Bauxite, commonly referred to as red mud, is an industrial waste product from alumina (Al_2O_3) production (Borra et al. 2016). Bauxite is a mixture of various minerals with residual metal oxides of Al, Fe, and Si as characterized through XRD, TGA, and gamma spectroscopy (Earnest et al. 2018; Miller and Voutchkov 2014). Currently, the waste is collected in landfills with environmental concerns of toxicity and pollution of the surrounding soils and rivers (Mayes et al. 2011).

Al-rich phases in bauxite can be removed by washing with base in an adapted Bayer process (Tsamo et al. 2017; Li et al. 2016). The elimination of Al phases within the bauxite enhances the amount of Fe-rich phases present. Fe phases such as magnetite and hematite can be present and separated with a magnetic field (Rao et al. 1997).

Waste products have been previously used as admixtures and supplementary materials in concrete. For example, silica fume (Siddique 2011), fly ash, and other byproducts of industrial processes are widely used and provide benefits in the strengthening of concretes.

This study was performed to understand the magnetic properties of bauxite before and after base treatment to create a magnetic supplementary material in concrete. Chemical composition and magnetic properties were characterized with XRD and VSM for the untreated and treated bauxite samples. As indicated earlier in Section 2.1, the bauxite was treated with NaOH to remove certain constituents in the samples. In particular, NaOH was extremely effective at removing the Al-rich phases such as gibbsite ($Al(OH)_3$) and kaolinite ($Al_2Si_2O_5(OH)_4$) as well as carbonate phases such as calcite ($CaCO_3$) and siderite ($FeCO_3$). After treatment, phases that were not removed, such as Fe-rich phases (Hematite (Fe_2O_3) and Iron Aluminum Oxide Hydroxide (FeAlO(OH)) showed higher concentrations in the treated samples.

5.1 X-ray diffraction

The mineral contents of each sample of NIST 69B-Ark before and after reaction with NaOH are given in Table 7. The reaction lowered the amount of gibbsite, siderite, and muscovite (highlighted in red font);

preferentially enhanced those minerals present; and allowed observation of minerals not observed in the untreated sample. The presence of magnetite was observed in this sample.

Table 7. Quantitative X-ray diffraction analysis of 69b-Ark and 69b-Ark-treated.

Phase	Formula	As received	Treated
Gibbsite	$Al(OH)_3$	67.3	6.9
Kaolinite	$Al_2Si_2O_5(OH)_4$	19.0	54.9
Siderite	$Fe(CO_3)$	11.3	0
Muscovite	$KAl_2(AlSi_3O_{10})(F,OH)_2$	7.8	0.6
Anatase	TiO_2	1.2	5.9
Magnetite	Fe_3O_4	1.2	7.8
Quartz	SiO_2	0.7	6.8
Boehmite	AlO(OH)	0.5	0.1
Sodium Aluminosilicate	$Na_6(Al_6Si_6O_{24})_2NaF_xH_2O$	0	16.9

The mineral contents of each sample of NIST 698-Jam before and after reaction with NaOH are given in Table 8. The reaction lowered the amount of gibbsite and calcite (highlighted in red font) and allowed detection of phases that were at lowered concentration in the untreated sample.

Table 8. Quantitative X-ray diffraction analysis of 698-Jam and 698-Jam-treated.

Phase	Formula	As received	Treated
Gibbsite	$Al(OH)_3$	76.3	6.9
Hematite	Fe_2O_3	11.5	46.7
Iron Aluminum Oxide Hydroxide	$(Fe_{0.83}Al_{0.17})AlO(OH)$	9.7	36.7
Anatase	TiO_2	2.0	6.8
Calcite	$CaCO_3$	0.5	0.1
Boehmite	AlO(OH)	0.5	1.5
Rutile	TiO_2	0.0	1.3

The mineral contents of each sample of NIST 697-Dom before and after reaction with NaOH are given in Table 9. The reaction lowered the amount of gibbsite, kaolinite, and calcite (highlighted in red font) and allowed detection of phases that were at lower concentrations in the untreated sample.

Table 9. Quantitative X-ray diffraction analysis of 697-Dom and 697-Dom-treated.

Phase	Formula	As received	Treated
Gibbsite	$Al(OH)_3$	54.0	0.0
Hematite	Fe_2O_3	16.6	45.6
Boehmite	AlO(OH)	13.0	35.7
Kaolinite	$Al_2Si_2O_5(OH)_4$	7.5	0.0
Aluminum Oxide Hydroxide	AlO(OH)	0.0	8.5
Iron Aluminum Oxide Hydroxide	$(Fe_{0.83}Al_{0.17})AlO(OH)$	5.5	2.2
Anatase	TiO_2	2.6	4.2
Calcite	$CaCO_3$	0.7	0.0
Chlorite	$(Mg,Fe^{2+})_5Al_2Si_3O_{10}(OH)_8$	0.1	0.8
Quartz	SiO_2	0.0	0.4
Goethite	FeO(OH)	0.0	0.0
Periclase	MgO	0.0	2.5

The mineral contents of each sample of NIST 696-Sur before and after reaction with NaOH are given in Table 10. The reaction lowered the amount of gibbsite (highlighted in red font) and allowed detection of phases that were at lower concentrations in the untreated sample.

Table 10. Quantitative X-ray diffraction analysis of 696-Sur and 696-Sur-treated.

Phase	Formula	As received	Treated
Gibbsite	$Al(OH)_3$	93.4	63.8
Iron Aluminum Oxide Hydroxide	$(Fe_{0.83}Al_{0.17})AlO(OH)$	2.9	17.4
Hematite	Fe_2O_3	2.2	11.1
Anatase	TiO_2	1.4	7.5
Kaolinite	$Al_2Si_2O_5(OH)_4$	0.2	0.2

The mineral contents of each sample of NIST 600-Aus before and after reaction with NaOH are given in Table 11. The reaction lowered the amount of gibbsite and the trace of siderophyllite (highlighted in red font) and allowed detection of phases that were at lower concentrations in the untreated sample.

Table 11. Quantitative X-ray diffraction analysis of 600-Aus and 600-Aus-treated.

Phase	Formula	As received	Treated
Gibbsite	$Al(OH)_3$	54.4	0.5
Quartz	SiO_2	20.6	47.3
Iron Aluminum Oxide Hydroxide	$(Fe_{0.83}Al_{0.17})AlO(OH)$	17.1	33.2
Hematite	Fe_2O_3	5.6	16.3
Anatase	TiO_2	2.1	2.6
Siderophyllite	$KFe2.1Al_{2.8}Si_{2.1}O_{10}(OH)_2$	0.1	0.0

5.2 Magnetic characterization

Figure 16 presents the VSM characterization results of the five bauxite samples in the as-received and treated states. Table 12 summarizes the maximum magnetization of the samples at 30,000 Oe (3 T) and compares the difference between treatments on each type. Arkansas bauxite, when treated, had the largest magnetization of ~1.9 emu/g and showed an increase of 90% over the untreated sample. Australian bauxite had the second highest magnetization at 0.99 emu/gm and a ~55% change. Samples from Jamaica and Surinam exhibited the second and third highest magnetization differences of 71% and 69%, respectively. Dominican bauxite showed a decrease in magnetization when treated with a -22% change in maximum magnetization.

Based on XRD and VSM characterization, bauxite samples do change phases and magnetization, but the magnetizations are very low compared to typical magnetic particles. Compared to CIP with magnetization at 216 emu/gm, bauxite would not be able to provide substantial magnetic effects towards stiffening a slurry-based MRCM.

Figure 16. Magnetization curves of as-received and treated NIST bauxite samples.

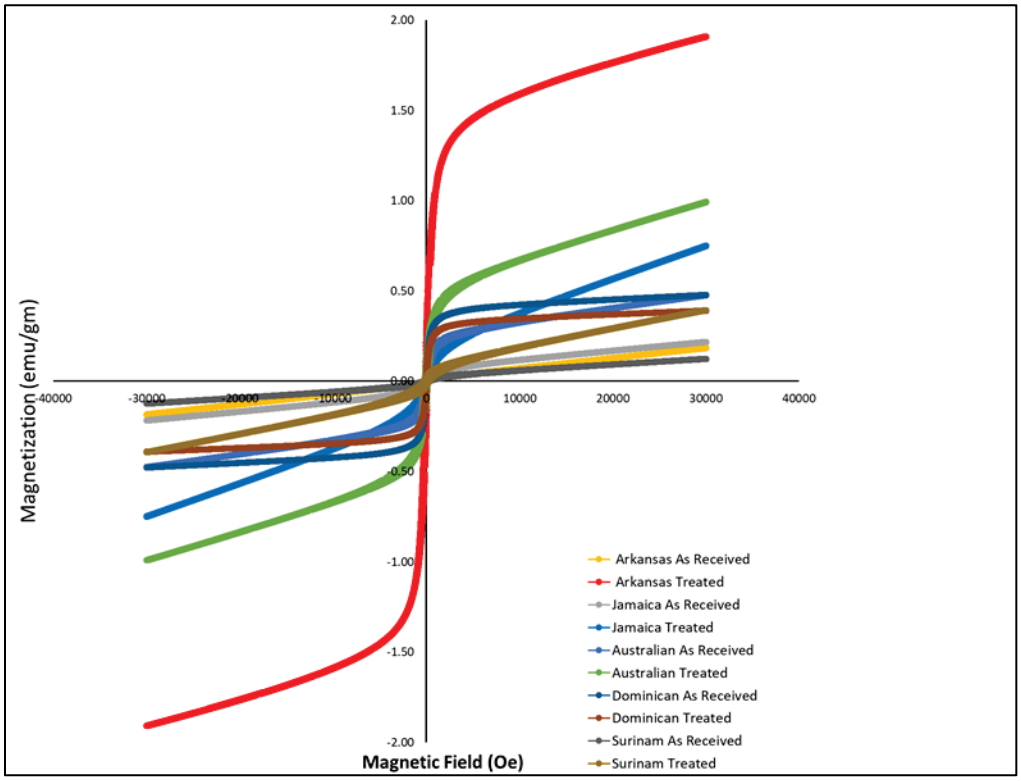

Table 12. Summary of magnetization values of as-received untreated and treated NIST bauxite samples.

Bauxite Sample	As-received (emu/gm)	Treated (emu/gm)	% Difference
Arkansas	0.1844	1.9091	90.34
Jamaica	0.2175	0.7495	70.99
Australian	0.4764	0.9923	54.99
Dominican	0.4779	0.3906	-22.34
Surinam	0.1240	0.3939	68.51

6 Characterization of Styrene-Butadiene Rubber/Carbonyl Iron Particle Elastomer Composites

MREs are a special class of smart composite materials. Similar to other smart materials that operate with an applied stimulus, MREs respond to applied external magnetic fields to create tunable mechanical and rheological properties. MREs typically consist of an elastomeric material or rubber matrix component with magnetic particles dispersed throughout. Various materials have been used as the matrix material, such as polydimethylsiloxane (Cvek et al. 2017; Mordina et al. 2014), silicone rubber (Shabdin et al. 2019; Aziz et al. 2019), natural rubber, SBR, styrene-ethylene-co-butylene-styrene (Lu et al. 2012; An et al. 2010), and polyurethanes(Zhu et al. 2012; Boczkowska and Awietjan 2009).

MREs have the advantage over MR fluids in the stability of the magnetic fillers, since the fillers are entrained and mobility is restricted in the rubber matrix. In MR fluids, the magnetic fillers tend to sediment over time and continued use. The MREs, with solidlike characteristics, do not exhibit particle settling since there is no fluid phase to allow particles to move as freely.

CIPs are the most common magnetic particles used in the synthesis of MREs. CIPs have many advantageous properties, such as high saturation magnetization and low remnant magnetization. The micron-sized CIPs also have a spherical particle shape that helps in mixing into the various matrices to create MREs. To enhance the incorporation of CIP as a filler, researchers have used chemical functionalization to promote better inclusion. Cvek and coworkers used polymer-grafting strategies to attach poly(trimethylsiyloxyethyl methacrylate) to CIP (Cvek et al. 2017). The covalent attachment of polymer chains did not greatly alter the magnetic properties of the CIP and was able to enhance particle and polymer matrix compatibility of the MRE, thereby increasing the magnetorheology.

The ability to change rheological behaviors under various magnetic stimuli gives MREs potential benefits in a variety of applications ranging from shock-dampeners to sensors. Shabdin and coworkers formulated MREs from silicone rubber with CIP and graphite for use as force sensors (Shabdin et al. 2019). The MR properties of the MRE were coupled with

experimental data, and modeling of resistance measurements that indicated inclusion of graphite into the MRE increased the conductivity of the composite material.

SBR is a common-use rubber that has been implemented into a variety of applications in asphalt (Lv et al. 2018). SBR composites have been formulated with carbon black/clay (Ayippadath Gopi et al. 2011), graphene oxide (Mao et al. 2013), and silica (Baeza et al. 2013) to increase mechanical and thermal properties. Magneto-active, filled SBR systems have been previously studied for thin film electronic applications (Chipara et al. 2004; Saleh Medina et al. 2015). Spin-coating and solvent casting to create thin film composites provided facile ways to create SBR composites.

In this study, isotropic CIP-filled SBR polymer composites were formulated with different magnetic particle loadings via solvent casting, and the MR responses were investigated under various magnetic fields. SEM, VSM analysis, and TGA were conducted to increase understanding of the morphological, magnetic, and structural properties of the composites. MR behaviors were studied using parallel plates to determine the relationship of magnetic particle loading on the deformation and time-dependent viscoelastic properties.

6.1 Microstructural characterization

A representative dispersion of CIP within a polymer MRCM, ascertained by micro-computed tomography (micro CT), is shown in Figure 17. The density of the CIP allowed for good contrast between the particles and the polymer matrix, as shown by the white spots. In the left-side image, the contrast was set to capture the dimensions of the 8 mm disc (polymer and CIP), and in the right-side image, the contrast was adjusted to highlight the CIP dispersion only. Since the MRCMs were synthesized from solvent casting under no magnetic field, the CIPs were randomly distributed throughout the matrix and oriented isotropically.

Figure 17. Representative micro CT scan of polymer-based MRCM.

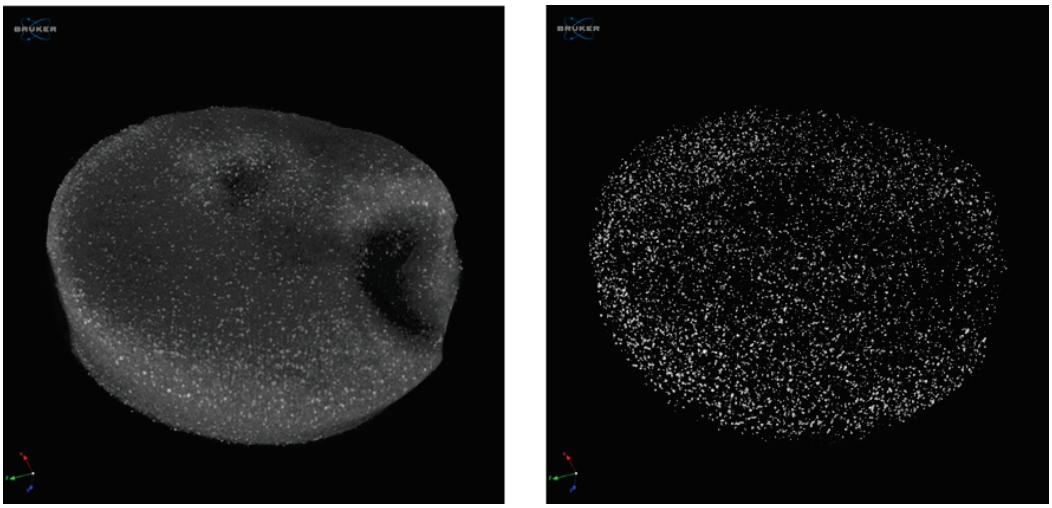

Figure 18 and Figure 19 illustrate CIP dispersions of 8 and 17 vol. %, respectively, as characterized by SEM at 1,000x magnification. In both loadings, the CIPs were dispersed throughout the matrix, but local aggregation of the particles was observed. In the samples with 8 vol. % CIP, the particles were arranged such that the CIP aggregates may not interact with one another. For the higher loading of 17 vol. %, the spacing among CIP aggregates was small enough that responses under magnetic fields were influenced by aggregate interactions throughout the matrix.

Figure 18. SEM image of 8 vol. % CIP.

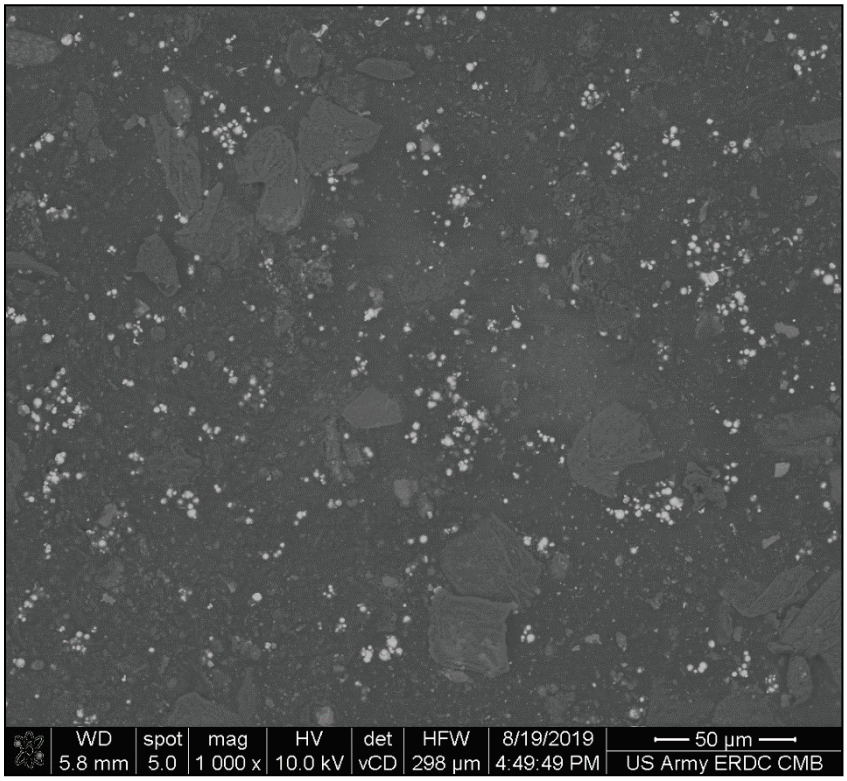

Figure 19. SEM image of 17 vol. % CIP.

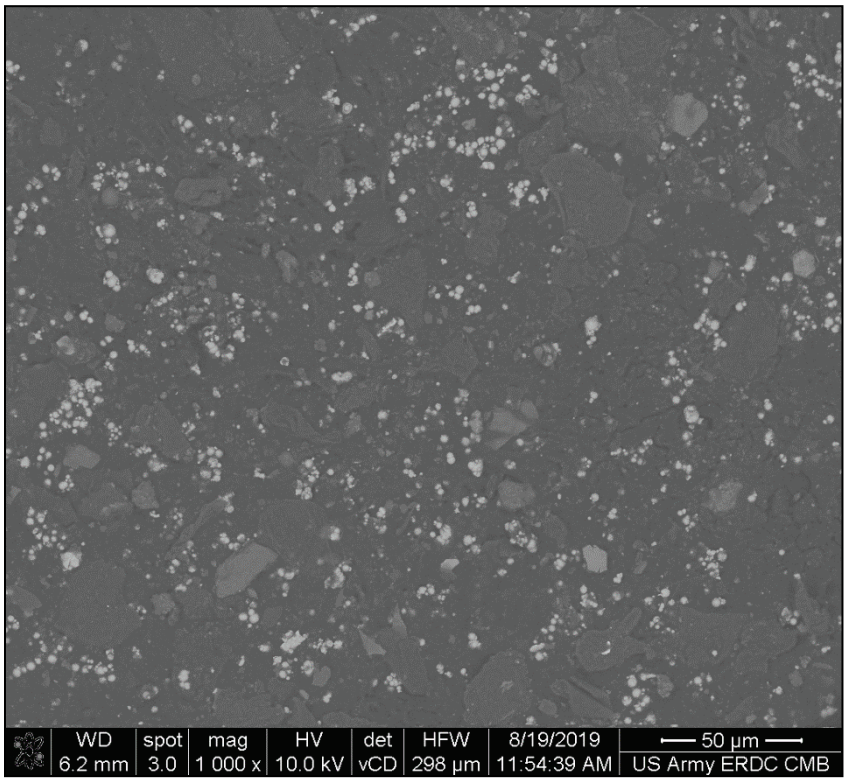

6.2 Thermal characterization

TGA was conducted to confirm incorporation of magnetic CIP into the polymer matrix, with raw thermal degradation curves of CIP, SBR polymer, and 8 and 17 vol. % CIP in SBR as shown in Figure 20. Incorporating the CIP particles into the polymer matrix at both loading levels shifted the onset of polymer degradation from about 370 °C (neat polymer) to approximately 410 °C (CIP-filled polymers). The largest weight change was observed over the range of approximately 400–500 °C. For the control polymer, only ~1.1% remained after approximately 480 °C.

The neat CIP sample showed an increase in mass starting at 200°C and reached 130% mass at 1000 °C. This increase in weight has been reported elsewhere and is attributed to pure Fe forming oxides such as FeO and Fe_2O_3 (Zhu et al. 2012; Cvek et al. 2017). The 8 and 17 vol. % CIP samples also showed weight gains due to Fe oxidation, but the phenomena onset at much higher temperatures in these samples at approximately 480 °C. The dramatic increase in the onset temperature of Fe oxidation makes sense regarding the presence of the polymer. At lower temperatures, the CIP was embedded in the polymer matrix and thus protected from the atmosphere. At approximately 480 °C, the polymer was almost completely burned off, exposing the CIP surfaces for oxidation.

At 1,000 °C, the 8 vol. % CIP sample retained approximately 52% of its initial weight, and the 17 vol. % CIP sample retained approximately 70% of its weight. This result must be examined on a mass or weight basis. Based on the specific gravities of CIP (7.9) and SBR (0.94), 8 and 17 vol. % CIP loadings by volume equate to 42 and 60 wt. % CIP, respectively. One should expect that, at approximately 480 °C, the temperature at which the polymer should be gone, only the CIP would remain and that the 8 and 17 vol. % samples would show approximately 40 and 60 wt. % remaining, respectively. The discrepancies arise from the CIP mass gain being at 10% around the temperatures of highest decomposition for the composites.

Figure 20. TGA results of CIP, polymer, 8 vol. % and 17 vol. % CIP in air.

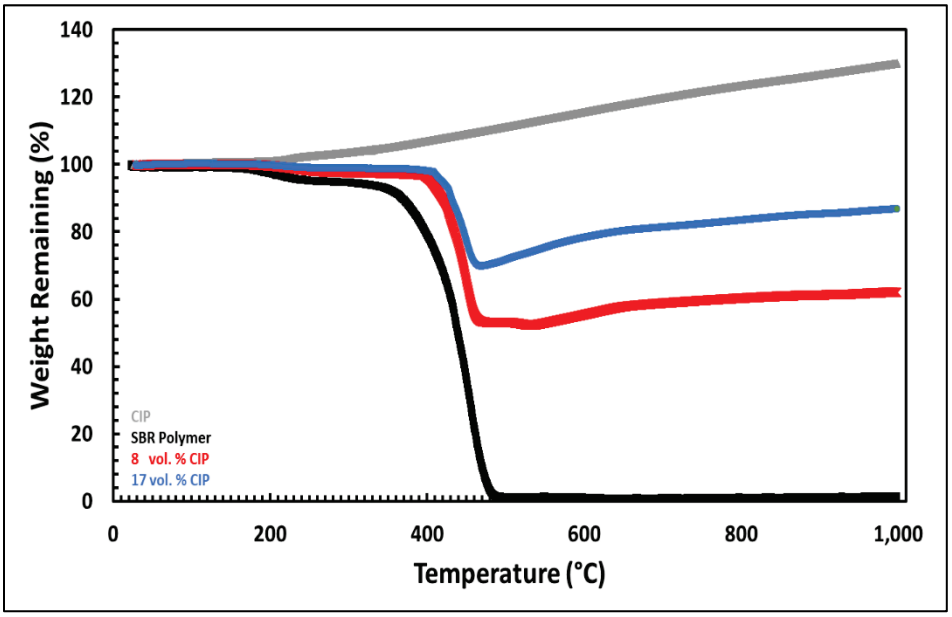

6.3 Magnetic characterization vibrating sample magnetometer (VSM)

The magnetic characteristics of the polymer MRCMs are summarized in Figure 21. The polymer is non-magnetic, as expected. The CIP had a magnetization of 216 emu/gm. The polymer-based MRCMs of 8 and 17 vol. % (42 and 60 wt. %) CIP had magnetizations of 91.83 and 139.02 emu/gm, respectively. As expected, the magnetizations of the composites follow a basic rule of mixtures based on CIP loading by weight.

Figure 21. Magnetization curves of polymer, CIP, and 8 and 17 vol. % CIP samples.

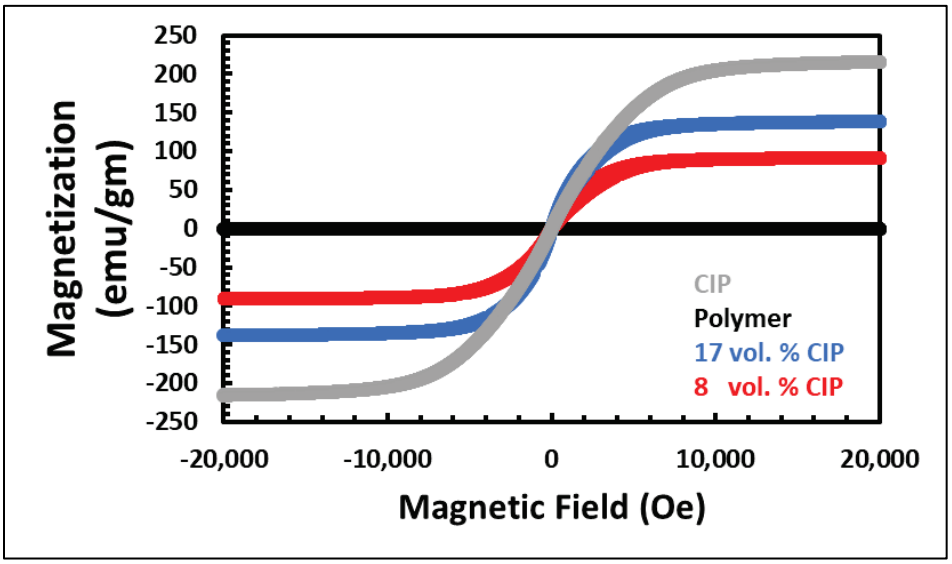

6.4 Magnetorheological characterization

6.4.1 Magnetic sweeps

The magnetic sweeps of the polymer-based MRCM are summarized in Figure 22. The storage modulus was monitored as function of the applied magnetic flux up to 1 T for the control (neat polymer) and 8 and 17 vol. % samples. The addition of the dense CIP to the polymer matrix increased the zero field modulus when compared to the control sample. The zero modulus (G'_0) of the control polymer was 111,577 Pa while the 8 vol. % and 17 vol. % composites had G'_0 of 365,449 Pa and 594,031 Pa, respectively.

Figure 22. Magnetic sweeps of polymer, 8 vol. % CIP, and 17 vol % CIP.

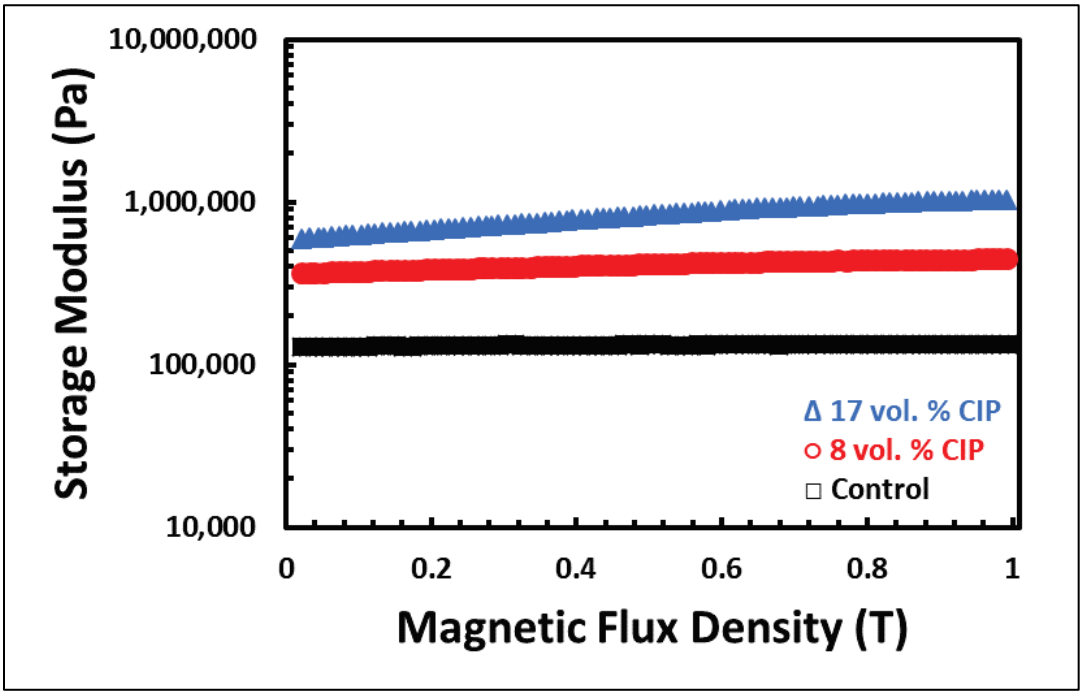

To understand the MR of increasing magnetic fields, Equation 2 was used to capture the change in G' throughout the magnetic sweep.

$$\text{Magnetorheological Effect: MR} = \left(\frac{G'_{max}-G'_0}{G'_0}\right) \times 100 \quad (2)$$

where

G'_0 = storage modulus at zero magnetic field

G'_{max} = storage modulus at maximum magnetic field (1 T).

Table 13 summarizes the results of the magnetic sweeps with the MR effect calculated. The control had a small MR effect of 3.72% from a change in G' of 4,306 Pa. The 8 vol. % CIP MRCM showed a 22.11% MR effect with a ΔG' of 80,805 Pa. The loading of CIP corresponded to 42 wt. %, so the dispersion of the magnetic filler within the polymer matrix caused a stiffening response under magnetic fields. The stiffening was further observed in the 17 vol. % sample as the MR effect was increased to 74.31%. The ΔG' for this CIP loading was 441,409 Pa. The higher loading of CIP at 60 wt. % increased the MR effect due to the inclusion of more magnetic filler and rigid contact between CIP particles. Increasing the loading of CIP beyond 17 vol. % created very brittle samples that were not able to be tested at the time of this writing.

Table 13. Magnetorheological effects on storage modulus of polymer, 8 vol. % CIP and 17 vol. % CIP.

Sample	G'_o (Pa)	G'_{Max} (Pa)	ΔG' (Pa)	MR Effect (%)
Control	111,577	115,883	4,306	3.72
8 vol. %	365,449	446,254	80,805	22.11
17 vol. %	594,031	1,035,440	441,409	74.31

6.4.2 Strain amplitude sweeps

Strain amplitude sweeps were conducted on the samples to observe changes in deformation-based viscoelastic oscillation behaviors with and without magnetic fields. The amplitude sweep of the control polymer sample is shown below in Figure 23. The LVE was present throughout this sample and indicated that the material's response was independent of the applied strain to a certain value. The modulus responses approached a critical crossover strain where G" became greater than G', but crossover did not occur under these testing conditions.

Figure 23. Strain sweep of control polymer sample under no magnetic field.

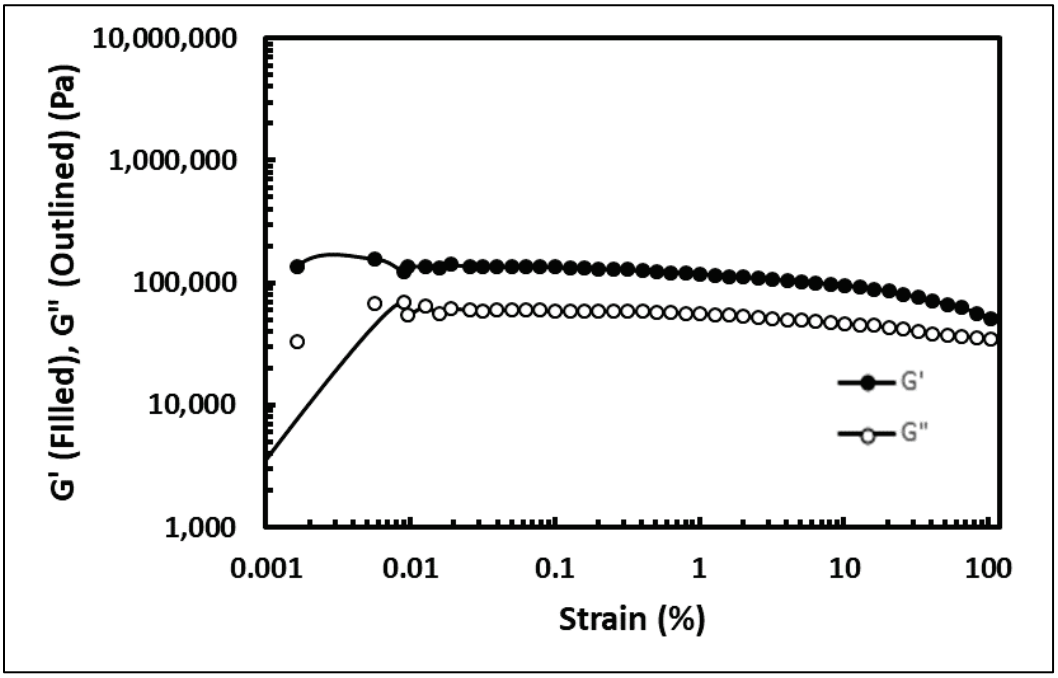

Figure 24 (top) shows the G' and G" results as a function of strain for the 8 vol. % CIP MRCM. For all conditions, the LVE appeared as the G' and G" were constant and then reached a level of strain where a decrease in the modulus responses was observed. A critical crossover strain where G" overtook G' was present for tests at approximately 10% strain, which was not observed in the control sample. This indicated yielding of the matrix material with the inclusion of the micron-sized magnetic filler. A semi-logarithmic plot of the G' data is presented in Figure 24 (bottom) to illustrate the stiffening effects under magnetic fields. The zero-field amplitude sweep had the lowest G' values, and the intermediate magnetic fields of 0.1, 0.3, and 0.5 had very similar modulus responses. Comparing these results to the magnetic sweep, the 8 vol. % (42 wt. %) composite had only a 22% MR effect; therefore, at those magnetic fields, high levels of dynamic stiffening were not occurring. For the 1 T field, the stiffening was seen, as the response at that field was much higher due to the activity of the CIP throughout the polymer matrix.

Figure 24. Amplitude strain sweep of 8 vol. % CIP at various magnetic fields: (top) logarithmic representation of G' and G" as a function of strain and (bottom) semi-logarithmic plot of G'.

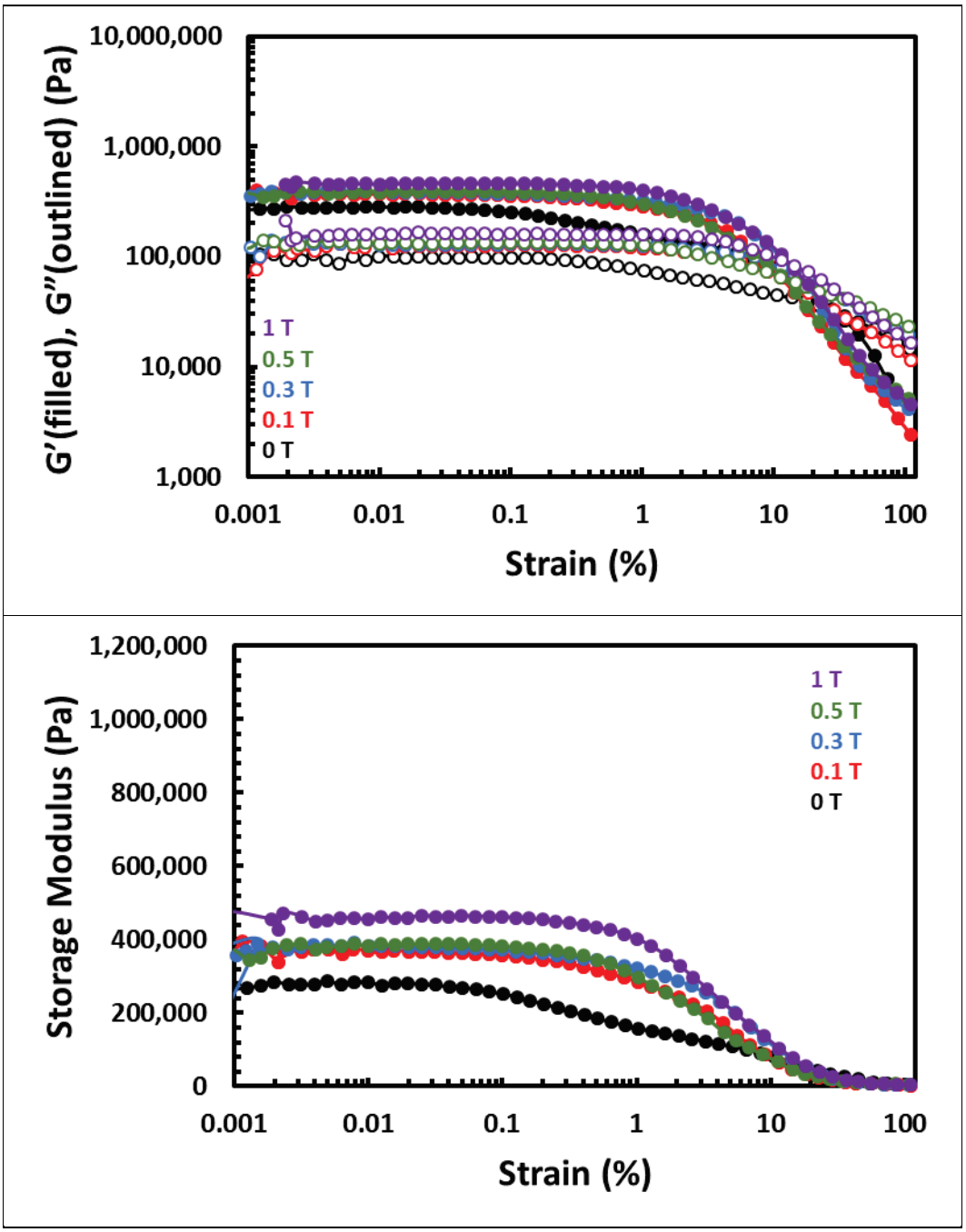

Stress amplitude sweeps for the 17 vol. % composite are shown in Figure 25. For all conditions, LVE was observed, and critical crossover between G" and G' occurred at approximately 10% strain. The semi-logarithmic plot of G' values (Figure 25 [bottom] below) captured the stiffening of the MRCM with various magnetic fields. The zero magnetic field showed the

lowest G' response, and due to the large MR effect, the magnetic field effect on G' indicated the clear differences in G' under those conditions. The responses at 0.3 and 0.5 T were similar, but at increasing strain, the 0.5 T result did not exhibit as sharp a decrease in G' until later strain values. The 1 T magnetic field imparted the highest degree of stiffening: increase of G'.

Figure 25. Amplitude strain sweep of 17 vol. % CIP at various magnetic fields : (top) logarithmic representation of G' and G" as a function of strain and (bottom) semi-logarithmic plot of G'.

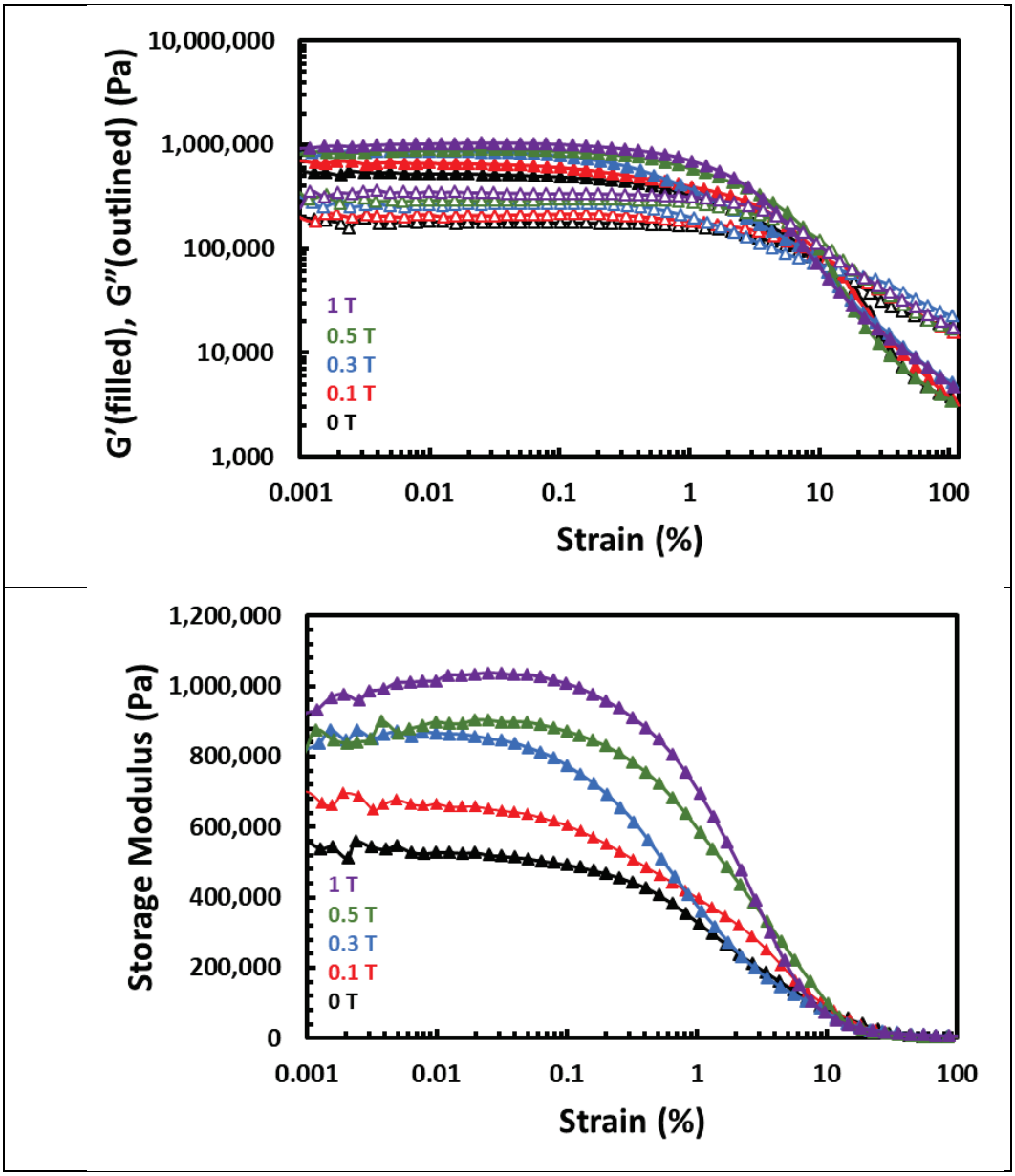

6.4.3 Frequency sweeps

The time-dependent behaviors of the polymer MRCMs were studied by using frequency sweeps. Figure 26 represents the control polymer without magnetic particles. For all angular frequencies tested, G' remained greater than G", and no modulus crossover was observed.

Figure 26. Frequency sweep of control polymer sample under no magnetic field with G' as filled-in symbols and G" as outlined symbols.

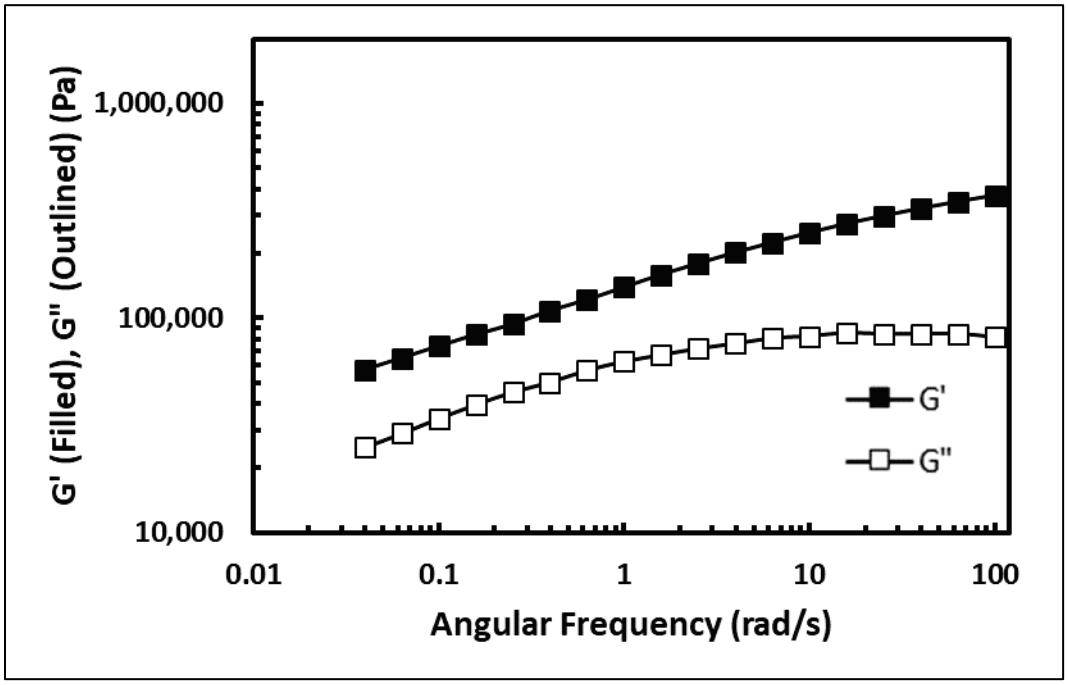

Figure 27 summarizes the frequency sweeps of 8 vol. % CIP MRCM under magnetic fields from 0 to 1 T. The elastomer viscoelasticity was not altered as the magnetic fields were increased. The G' responses as a function of magnetic field did not stiffen greatly due to the MR effect of the 8 vol. % composite being only 22%.

Figure 27. Frequency sweeps of 8 vol. % CIP samples at various magnetic fields with G' as filled-in symbols and G" as outlined symbols.

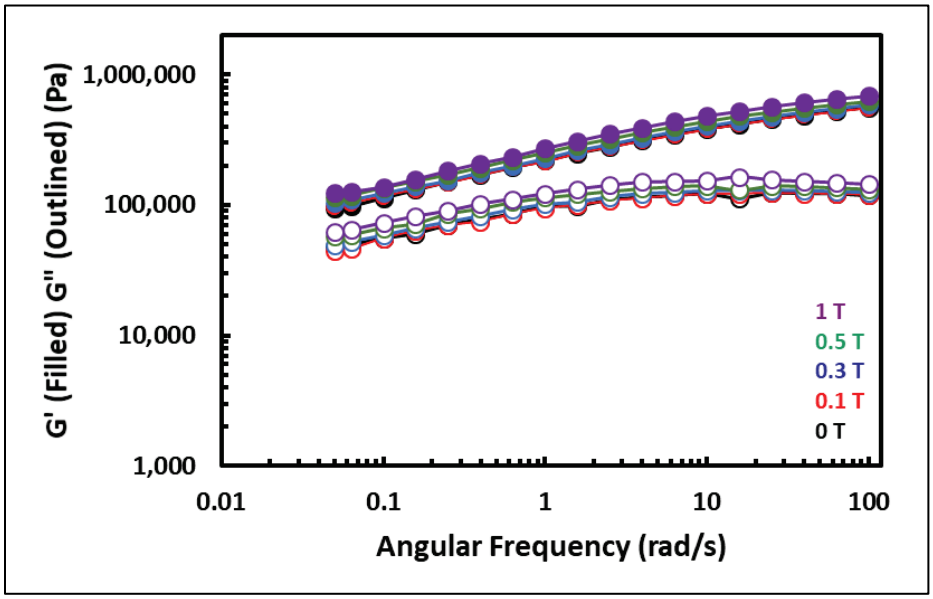

The 17 vol. % CIP composite frequency sweeps are shown in Figure 28 for magnetic fields varying from 0 to 1 T. The viscoelastic behaviors did not change, and no modulus crossovers were observed similar to the control and 8 vol. %. For these samples, stiffening of the composites was noticeable as the G' responses increased significantly with increasing magnetic field strength.

Figure 28. Frequency sweeps of 17 vol. % CIP samples at various magnetic fields with G' as filled-in symbols and G" as outlined symbols.

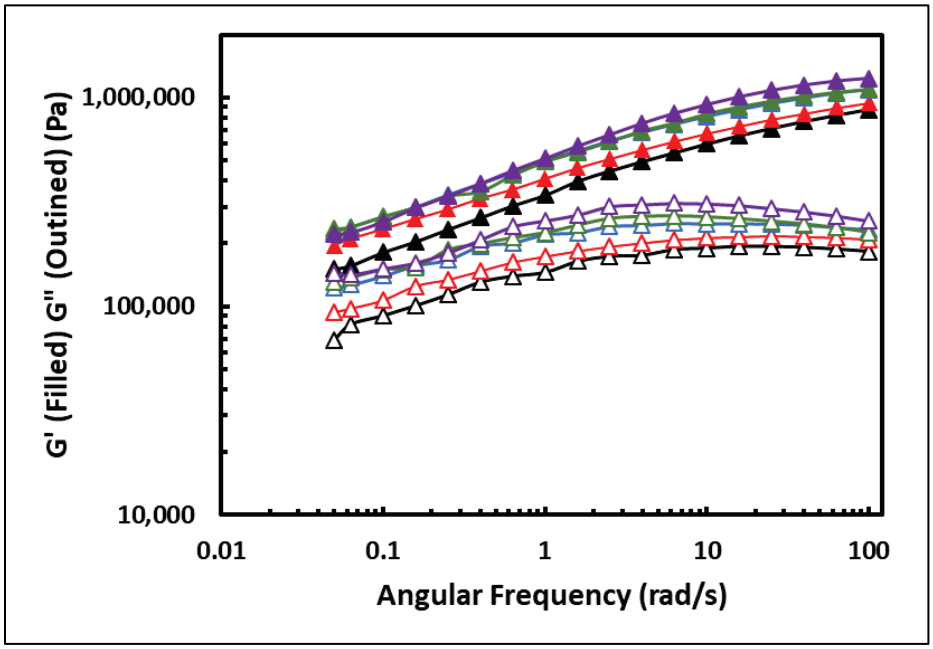

The loss factor tan δ is the ratio of G" to G' and can describe the bonding energy of the CIP to the polymer elastomer matrix (Kwon and Lee 2018). Figure 29 shows the loss factors for 0 and 1 T experiments for 8 and 17 vol. % CIP MRCMs. The loss factor relationships for the 0 T conditions indicated that energy dissipation was independent of filler content. The 1 T, 8 vol. % result also showed a similar loss factor to the 0 T conditions. For 17 vol. %, the 1 T experiment indicated an increase in the loss factor at low frequencies, resulting in a higher degree of CIP mobility in the polymer matrix. This increase in mobility is a result of the uncrosslinked matrix and strong magnetization of the CIP at the high magnetic field.

Figure 29. Loss factor comparisons of 8 and 17 vol. % at 0 and 1 T.

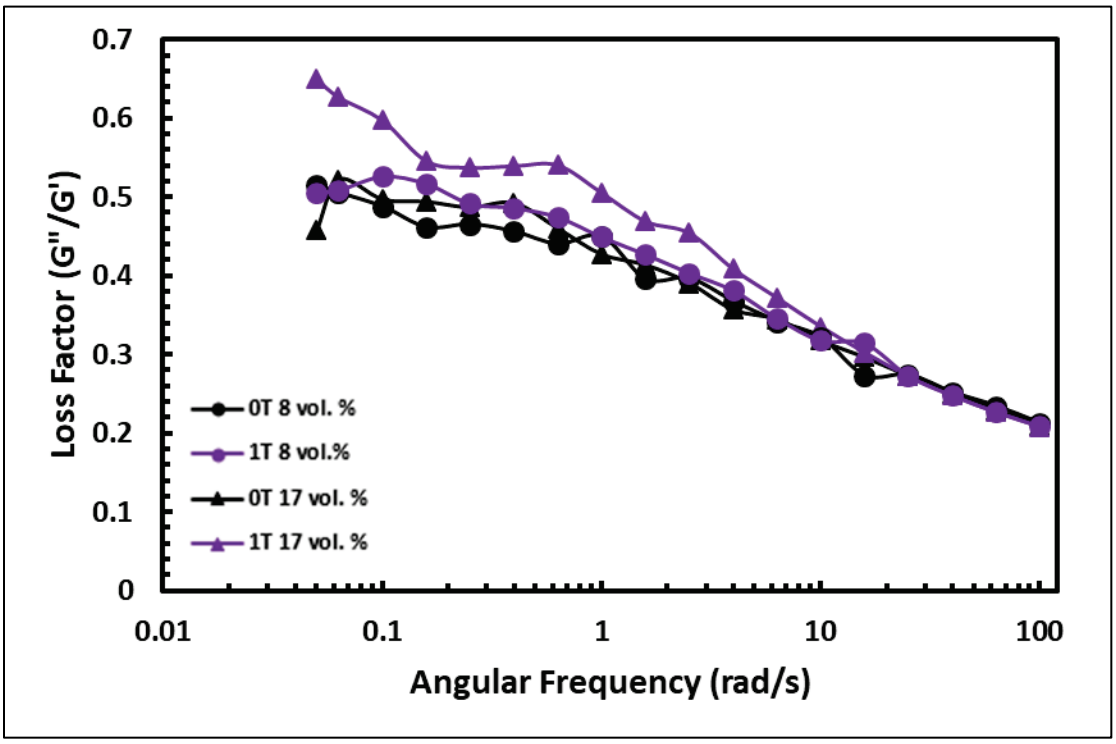

7 Conclusions

MRCMs were synthesized from slurry-based and polymer-based systems. The goal of this project was to create rapidly stiffening materials for use in deployable force protection and projection systems with tunable properties.

Slurry-based MRCMs were formulated to be similar in consistency to a freshly mixed cement mortar to mimic uses in construction applications. From magnetic sweeps, the three formulations ranging from 20 to 40 wt. % magnetic CIP content were able to stiffen by orders of magnitude when an applied magnetic field was increased. The shear stress responses of these slurries were also shown to increase as a function of magnetic field and CIP content. Modeling of flow curve data using common models was difficult to fit at low shear rates at higher magnetic fields. Experimentally observed yield stresses for the slurries showed that the yield stress could be tuned from as low as 9 Pa at no magnetic fields to more than 15,000 Pa at 1 T. At no magnetic fields, the amount of kaolinite clay had the highest effect on the shear stress response and yield stress. For applied magnetic fields, the CIP content dictated the shear stress responses as 40 wt. % CIP slurries had the highest responses when under magnetic fields. With these tunable shear stresses and yield stress, the slurry-based MRCMs are promising in the area of three-dimensional printing of structures from cementitious materials. The slurries with high shear stress responses under magnetic fields can be self-supporting, allowing for rapid printing.

The use of bauxite waste material was investigated to determine whether these materials could be used as supplementary magnetic materials in slurry-based MRCMs. NIST standard bauxites were base-treated and filtered. XRD of each bauxite sample was performed on as-received and base-treated powders. Phase compositions were compared to understand how Al phases and Fe-rich phases were affected. VSM captured changes in magnetic behavior among the bauxite samples with Arkansas bauxite exhibiting the highest magnetization behavior. Bauxite mineral phases and magnetization behaviors were changed by chemical treatment, but magnetic response remained very low compared to the responses of more traditional magnetic materials; therefore, the bauxite materials were not formulated into MRCMs.

Polymer-based MRCMs were synthesized from SBR with CIP embedded within the rubber matrix to explore their response mechanisms and behaviors. CIP content was set at 8 and 17 vol. %. SEM images illustrated that CIPs were dispersed throughout the matrix, but aggregation did occur. Magnetization of the polymer-based samples followed a rule of mixtures relationship between the amount of non-magnetic polymer and magnetic CIP on a weight basis. Magnetic sweeps of the polymer-based MRCMs indicated that the MR effect was dependent on the amount of CIP. The control polymer sample had a negligible increase in modulus with applied magnetic field, but the 8 vol. % CIP MRCM had an MR increase of 22%, and the 17 vol. % CIP MRCM showed a 74% in MR effect. Strain amplitude sweeps indicated that modulus crossover was present for all samples and magnetic field conditions. Modulus stiffening was observed in both amplitude and frequency sweeps.

Future work in this area will address stability of the slurry-based MRCMs and formulation of more uniformly dispersed polymer-based MRCMs. Polymeric admixtures at low dosages could potentially be added to the slurries to create more stable suspensions without lowering magnetization greatly. For polymer-based MRCMs, novel crosslinking and fillers can now be investigated to create more durable materials for force protection and projection applications.

The lessons learned through this research can be transitioned to various basic and applied research programs such as “Effects of an External Electromagnetic Field on Magnetosome Biomineralization and Biogenesis” and “Hyper Performance Composites Using Directed Colloidal Crystallization.”

References

An, H., S. J. Picken, and E. Mendes. 2010. "Enhanced Hardening of Soft Self-Assembled Copolymer Gels under Homogeneous Magnetic Fields." *Soft Matter* 6 (18): 4497. https://doi.org/10.1039/c0sm00216j.

Ashour, O., C. A. Rogers, and W. Kordonsky. 1996. "Magnetorheological Fluids: Materials, Characterization, and Devices." *Journal of Intelligent Material Systems and Structures* 7 (2): 123–30. https://doi.org/10.1177/1045389X9600700201.

Ayippadath Gopi, J., S. K. Patel, A. K. Chandra, and D. K. Tripathy. 2011. "SBR-Clay-Carbon Black Hybrid Nanocomposites for Tire Tread Application." *Journal of Polymer Research* 18 (6): 1625–34. https://doi.org/10.1007/s10965-011-9567-9.

Aziz, S. A. B. A., S. A. Mazlan, N. A. Nordin, N. A. N. A. Rahman, U. Ubaidillah, S.-B. Choi, and N. Mohamad. 2019. "Material Characterization of Magnetorheological Elastomers with Corroded Carbonyl Iron Particles: Morphological Images and Field-Dependent Viscoelastic Properties." *International Journal of Molecular Sciences* 20 (13): 3311. https://doi.org/10.3390/ijms20133311.

Baeza, G. P., A.-C. Genix, C. Degrandcourt, L. Petitjean, J. Gummel, M. Couty, and J. Oberdisse. 2013. "Multiscale Filler Structure in Simplified Industrial Nanocomposite Silica/SBR systems Studied by SAXS and TEM." *Macromolecules* 46 (1): 317–29. https://doi.org/10.1021/ma302248p.

Boczkowska, A., and S. F. Awietjan. 2009. "Smart Composites of Urethane Elastomers with Carbonyl Iron." *Journal of Materials Science* 44 (15): 4104–11. https://doi.org/10.1007/s10853-009-3592-7.

Borra, C. R., B. Blanpain, Y. Pontikes, K. Binnemans, and T. Van Gerven. 2016. "Recovery of Rare Earths and Other Valuable Metals from Bauxite Residue (red mud): A Review." *Journal of Sustainable Metallurgy* 2 (4): 365–86. https://doi.org/10.1007/s40831-016-0068-2.

Böse, H., and J. Ehrlich. 2012. "Magnetorheological Dampers with Various Designs of Hybrid Magnetic Circuits." Edited by Prof Rongjia Tao and Prof Norman M. Wereley. *Journal of Intelligent Material Systems and Structures* 23 (9): 979–87. https://doi.org/10.1177/1045389X11433497.

Burroughs, J. F., J. Weiss, and J. E. Haddock. 2019. "Influence of High Volumes of Silica Fume on the Rheological Behavior of Oil Well Cement Pastes." *Construction and Building Materials* 203 (April): 401–7. https://doi.org/10.1016/J.CONBUILDMAT.2019.01.027.

Caballero-Hernandez, J., A. Gomez-Ramirez, J. D.G. Duran, F. Gonzalez-Caballero, A. Y. Zubarev, and M. T. Lopez-Lopez. 2017. "On the Effect of Wall Slip on the Determination of the Yield Stress of Magnetorheological Fluids." *Applied Rheology* 27 (1): 1–8. https://doi.org/10.3933/APPLRHEOL-27-15001.

Chae, H. S., S. H. Piao, A. Maity, and H. J. Choi. 2015. "Additive Role of Attapulgite Nanoclay on Carbonyl Iron-Based Magnetorheological Suspension." *Colloid and Polymer Science* 293 (1): 89–95. https://doi.org/10.1007/s00396-014-3389-3.

Chao, C.-G., M. P. Kumar, N. Riaz, R. T. Khanoyan, S. T. Madrahimov, and D. E. Bergbreiter. 2017. "Polyisobutylene Oligomers as Tools for Iron Oxide Nanoparticle Solubilization." *Macromolecules* 50 (4): 1494–1502. https://doi.org/10.1021/acs.macromol.6b02407.

Chin, B. D., J. H. Park, M. H. Kwon, and O. O. Park. 2001. "Rheological Properties and Dispersion Stability of Magnetorheological (MR) Suspensions." *Rheologica Acta* 40 (3): 211–19. https://doi.org/10.1007/s003970000150.

Chipara, M., D. Hui., J. Sankar, D. Leslie-Pelecky, A. Bender, L. Yue, R. Skomski, and D. J. Sellmyer. 2004. "On Styrene–Butadiene–Styrene–Barium Ferrite Nanocomposites." *Composites Part B: Engineering* 35 (3): 235–43. https://doi.org/10.1016/S1359-8368(03)00054-4.

Cvek, M., M. Mrlík, M. Ilčíková, J. Mosnáček, L. Münster, and V. Pavlínek. 2017. "Synthesis of Silicone Elastomers Containing Silyl-Based Polymer-Grafted Carbonyl Iron Particles: An Efficient Way to Improve Magnetorheological, Damping, and Sensing Performances." *Macromolecules* 50 (5): 2189–2200. https://doi.org/10.1021/acs.macromol.6b02041.

Cvek, M., M. Mrlík, M. Ilcikova, T. Plachy, M. Sedlacik, J. Mosnacek, and V. Pavlínek. 2015. "A Facile Controllable Coating of Carbonyl Iron Particles with Poly(glycidyl methacrylate): A Tool for Adjusting MR Response and Stability Properties." *Journal of Materials Chemistry C* 3 (18): 4646–56. https://doi.org/10.1039/c5tc00319a.

Cvek, M., M. Mrlík, and V. Pavlínek. 2016. "A Rheological Evaluation of Steady Shear Magnetorheological Flow Behavior Using Three-Parameter Viscoplastic Models." *Journal of Rheology* 60 (4): 687–94. https://doi.org/10.1122/1.4954249.

Dong, Y. Z., S. H. Piao, and H. J. Choi. 2018. "Fe3O4/sepiolite Magnetic Composite Particles and Their Magneto-Responsive Characteristics." *Colloid and Polymer Science* 296 (1): 11–19. https://doi.org/10.1007/s00396-017-4221-7.

Earnest, C. M., K. Gann, and B. Stong. 2018. "Improved Quantification of Gibbsite in Bauxite Ores by Thermogravimetric Methods (TGA and DTG)." *Advances in Applied Chemistry and Biochemistry* 1 (1): 9–17. https://doi.org/10.33513/ACBC/1801-02.

Hasheminejad, S. M., and M. Shabanimotlagh. 2010. "Magnetic-Field-Dependent Sound Transmission Properties of Magnetorheological Elastomer-Based Daptive Panels." *Smart Materials and Structures* 19 (3). https://doi.org/10.1088/0964-1726/19/3/035006.

Joshi, S. B. 2012. "Vibration Study of Magnetorheological Fluid Filled Sandwich Beams." *International Journal of Applied Research in Mechanical Engineering* 2(2): 100–104.

Kwon, S. H., C. H. Hong, P. X. Do, S.-B. Choi, and H. J. Choi. 2015. "Magnetorheology of a Carbonyliron Microsphere Suspension with a Halloysite Additive and Its Damping Force Characteristics." *Industrial & Engineering Chemistry Research* 54 (16): 4655–63. https://doi.org/10.1021/acs.iecr.5b00233.

Kwon, S. H., J. H. Lee, and H. J. Choi. 2018. "Magnetic Particle Filled Elastomeric Hybrid Composites and Their Magnetorheological Response." *Materials* 11(6): 1040. https://doi.org/10.3390/ma11061040.

Lara-Prieto, V., R. Parkin, M. Jackson, V. Silberschmidt, and Z. Kęsy. 2010. "Vibration Characteristics of MR Cantilever Sandwich Beams: Experimental Study." *Smart Materials and Structures* 19 (1): 015005. https://doi.org/10.1088/0964-1726/19/1/015005.

Lee, D., M. Lee, N. Jung, M. Yun., J. Lee, T. Thundat, and S. Jeon. 2014. "Modulus-Tunable Magnetorheological Elastomer Microcantilevers." *Smart Materials and Structures* 23 (5): 055017. https://doi.org/10.1088/0964-1726/23/5/055017.

Li, G., J. Luo, T. Jiang, Z. Li, Z. Peng, and Y. Zhang. 2016. "Digestion of Alumina from Non-Magnetic Material Obtained from Magnetic Separation of Reduced Iron-Rich Diasporic Bauxite with Sodium Salts." *Metals* 6(11): 294. https://doi.org/10.3390/met6110294.

Lu, X., X. Qiao, H. Watanabe, X. Gong, T. Yang, W. Li, K. Sun, et al. 2012. "Mechanical and Structural Investigation of Isotropic and Anisotropic Thermoplastic Magnetorheological Elastomer Composites Based on Poly (Styrene-b-Ethylene-Co-Butylene-b-Styrene) (SEBS)." *Rheologica Acta* 51: 37–50. https://doi.org/10.1007/s00397-011-0582-x.

Lv, S., S. Wang, T. Guo, C. Xia, J. Li, and G. Hou. 2018. "Laboratory Evaluation on Performance of Compound-Modified Asphalt for Rock Asphalt/Styrene–Butadiene Rubber (SBR) and Rock Asphalt/nano-CaCO3." *Applied Sciences* 8 (6): 1009. https://doi.org/10.3390/app8061009.

Manoharan, R., R. Vasudevan, and A. K. Jeevanantham. 2014. "Dynamic Characterization of a Laminated Composite Magnetorheological Fluid Sandwich Plate." *Smart Materials and Structures* 23 (2): 025022. https://doi.org/10.1088/0964-1726/23/2/025022.

Mao, Y., S. Wen, Y. Chen, F. Zhang, P. Panine, T. W. Chan, L. Zhang, Y. Liang, and L. Liu. 2013. "High Performance Graphene Oxide Based Rubber Composites." *Scientific Reports* 3 (1): 2508. https://doi.org/10.1038/srep02508.

Mayes, W. M., A. P. Jarvis, I. T. Burke, M. Walton, V. Feigl, O. Klebercz, and K. Gruiz. 2011. "Dispersal and Attenuation of Trace Contaminants Downstream of the Ajka Bauxite Residue (red mud) Depository Failure, Hungary." *Environmental Science & Technology* 45 (12): 5147–55. https://doi.org/10.1021/es200850y.

Miller, M., and M. Voutchkov. 2014. "The Impact of Uncertainty in the Elemental Composition of the Certified Reference Material on Gamma Spectrometry." *Journal of Radioanalytical and Nuclear Chemistry* 299 (1): 551–58. https://doi.org/10.1007/s10967-013-2781-7.

Mordina, B., R. K. Tiwari, D. K. Setua, and A. Sharma. 2014. "Magnetorheology of Polydimethylsiloxane Elastomer/FeCo 3 Nanocomposite." *The Journal of Physical Chemistry C* 118 (44): 25684–703. https://doi.org/10.1021/jp507005s.

Nair, S. D., and R. D. Ferron. 2014. "Set-on-Demand Concrete." *Cement and Concrete Research* 57: 13–27. https://doi.org/10.1016/j.cemconres.2013.12.001.

Popplewell, J., and R. E. Rosensweig. 1996. "Magnetorheological Fluid Composites." *Journal of Physics D: Applied Physics* 29 (9): 2297–2303. https://doi.org/10.1088/0022-3727/29/9/011.

Powell, L. A., N. M. Wereley, and J. Ulicny. 2012. "Magnetorheological Fluids Employing Substitution of Nonmagnetic for Magnetic Particles to Increase Yield Stress." *IEEE Transactions on Magnetics* 48 (11): 3764–67. https://doi.org/10.1109/TMAG.2012.2202885.

Rao, R. B., L. Besra, B. R. Reddy, and G. N. Banerjee. 1997. "The Effect of Pretreatment on Magnetic Separation of Ferruginous Minerals in Bauxite." *Magnetic and Electrical Separation* 8 (2): 115–23. https://doi.org/10.1155/1997/53574.

Rich, J. P., P. S. Doyle, and G. H. McKinley. 2012. "Magnetorheology in an Aging, Yield Stress Matrix Fluid." *Rheologica Acta* 51 (7): 579–93. https://doi.org/10.1007/s00397-012-0632-z.

Salen Medina, L. M., G. A Jorge, D. Rubi, N. D'Accorso, and R. M. Negri. 2015. "SBR/BiFeO3 Elastomer Capacitor Films Prepared under Magnetic and Electric Fields Displaying Magnetoelectric Coupling." *Journal of Physical Chemistry C* 119 (41): 23319–28. https://doi.org/10.1021/acs.jpcc.5b06056.

Sarkar, C., and H. Hirani. 2015. "Effect of Particle Size on Shear Stress of Magnetorheological Fluids." *Smart Science* 3 (2): 65–73. https://doi.org/10.6493/SmartSci.2015.317.

Seo, Y. P., S. Kwak, H. J. Choi, and Y. Seo. 2016. "Static Yield Stress of a Magnetorheological Fluid Containing Pickering Emulsion Polymerized Fe 2 O 3 /polystyrene Composite Particles." *Journal of Colloid and Interface Science* 463 (February): 272–78. https://doi.org/10.1016/j.jcis.2015.11.002.

Shabdin, M., M. A. Rahman, S. M. Ubaidillah, N. Hapipi, D. Adiputra, S. A. Aziz, I. Bahiuddin, and S.-B. Choi. 2019. "Material Characterizations of Gr-Based Magnetorheological Elastomer for Possible Sensor Applications: Rheological and Resistivity Properties." *Materials* 12 (3): 391. https://doi.org/10.3390/ma12030391.

Shah, K., and S.-B. Choi. 2015. "The Influence of Particle Size on the Rheological Properties of Plate-Like Iron Particle Based Magnetorheological Fluids." *Smart Materials and Structures* 24 (1): 015004. https://doi.org/10.1088/0964-1726/24/1/015004.

Siddique, R. 2011. "Utilization of Silica Fume in Concrete: Review of Hardened Properties." *Resources, Conservation and Recycling* 55 (11): 923–32. https://doi.org/10.1016/j.resconrec.2011.06.012.

Son, K. J., and E. P. Fahrenthold. 2012. "Evaluation of Magnetorheological Fluid Augmented Fabric as a Fragment Barrier Material." *Smart Materials and Structures* 21 (7): 075012. https://doi.org/10.1088/0964-1726/21/7/075012.

Tsamo, C., G. P. Kofa, and R. Kamga. 2017. "Decreasing Yield and Alumina Content of Red Mud by Optimization of the Bauxite Processing Process." *International Journal of Metallurgical Engineering* 6 (1): 1–9. https://doi.org/10.5923/j.ijmee.20170601.01.

Vereda, F., J. P. Segovia-Gutiérrez, J. De Vicente, and R. Hidalgo-Alvarez. 2015. "Particle Roughness in Magnetorheology: Effect on the Strength of the Field-Induced Structures." *Journal of Physics D: Applied Physics* 48 (1): 15309. https://doi.org/10.1088/0022-3727/48/1/015309.

Yalcintas, M., and H. Dai. 2004. "Vibration Suppression Capabilities of Magnetorheological Materials Based Adaptive Structures." *Smart Materials and Structures* 13 (1): 1–11. https://doi.org/10.1088/0964-1726/13/1/001.

Yang, Y., L. Li, and G. Chen. 2009. "Static Yield Stress of Ferrofluid-Based Magnetorheological Fluids." *Rheologica Acta* 48 (4): 457–66. https://doi.org/10.1007/s00397-009-0346-z.

Zhu, J., S. Wei, I. Y. Lee, S. Park, J. Willis, N. Haldolaarachchige, D. P. Young, Z. Luo, and Z. Guo. 2012. "Silica Stabilized Iron Particles toward Anti-Corrosion Magnetic Polyurethane Nanocomposites." *RSC Adv.* 2 (3): 1136–43. https://doi.org/10.1039/C1RA00758K.

Appendix A: Laser Diffraction and X-ray Diffraction Data of MRCM Candidate Materials

Figure A-1. Particle size analysis of CIP.

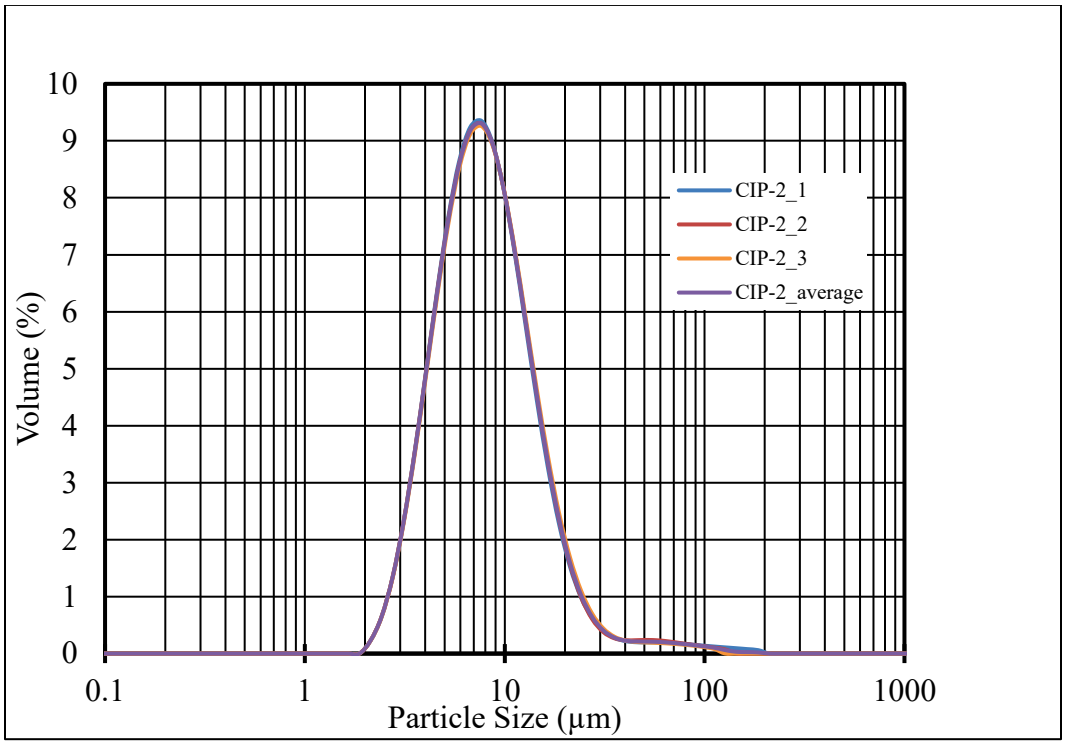

Figure A-2. Particle size analysis of iron for analysis.

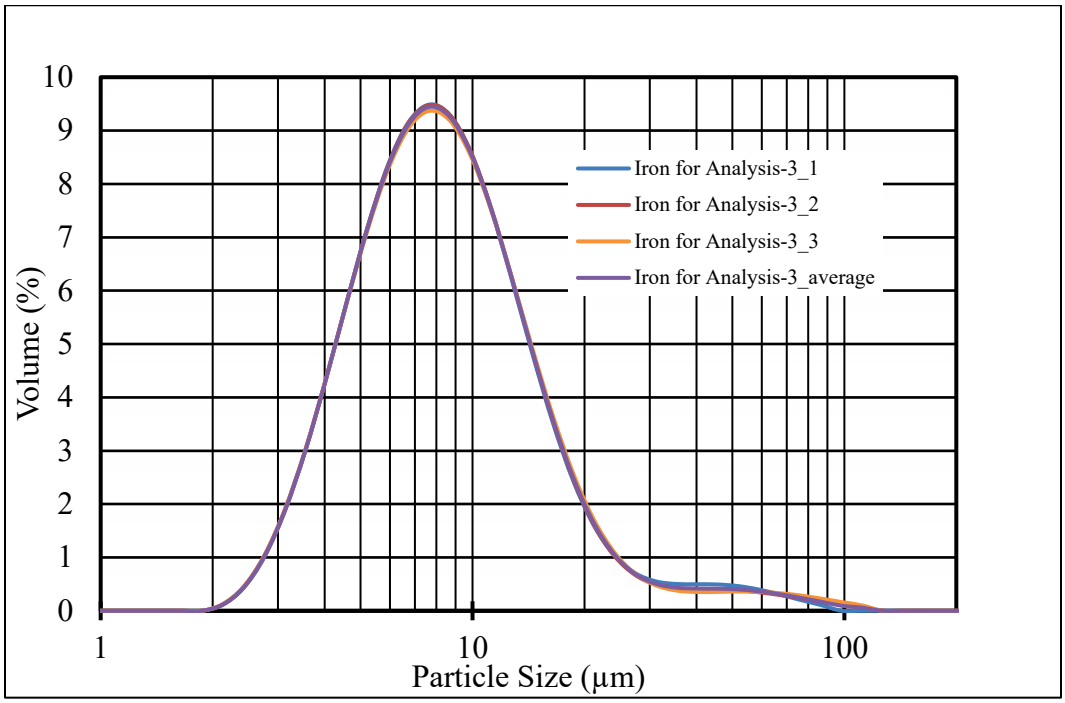

Figure A-3. Particle size analysis of iron electrolytic powder.

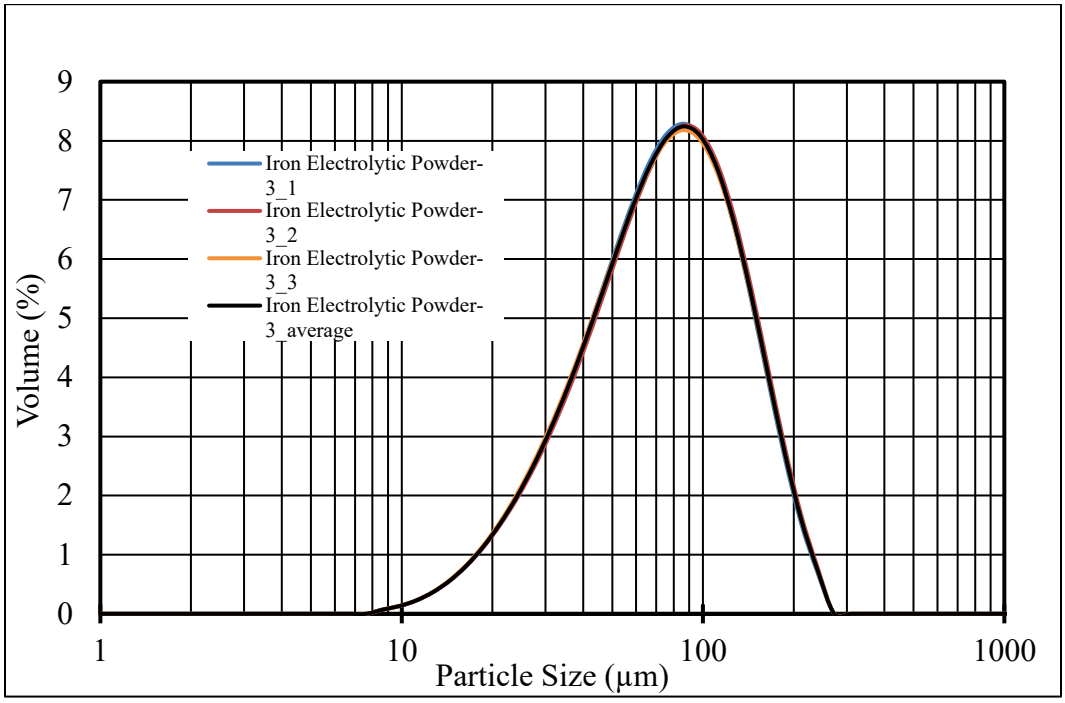

Figure A-4. Particle size analysis of kaolinite.

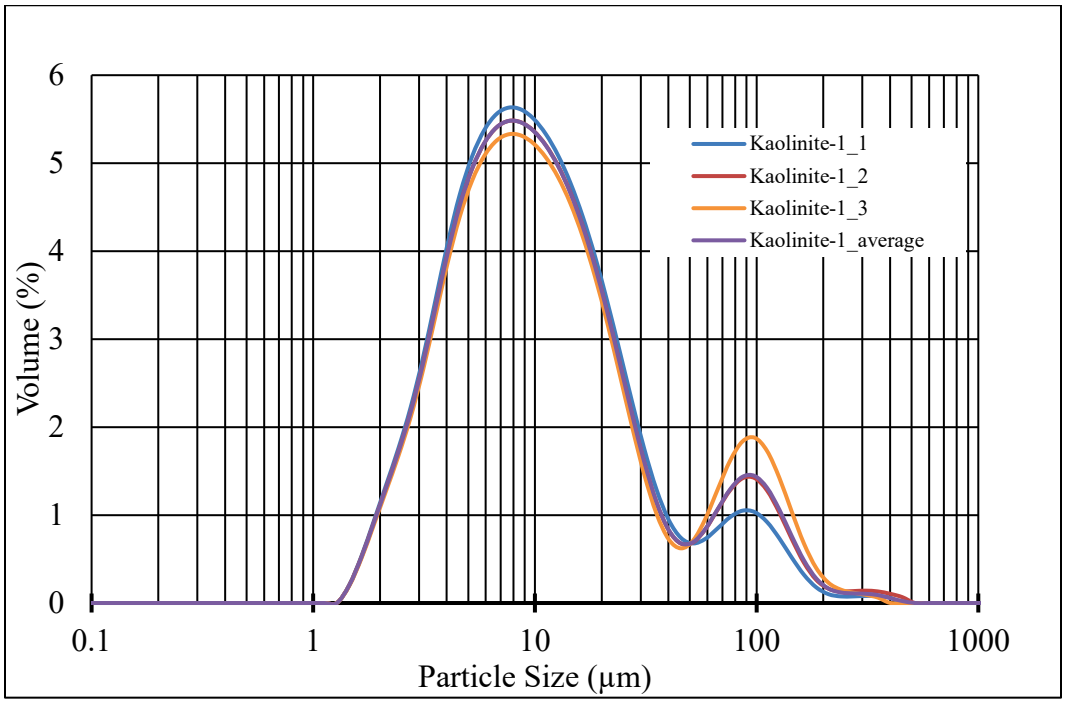

Figure A-5. Particle size analysis of sand.

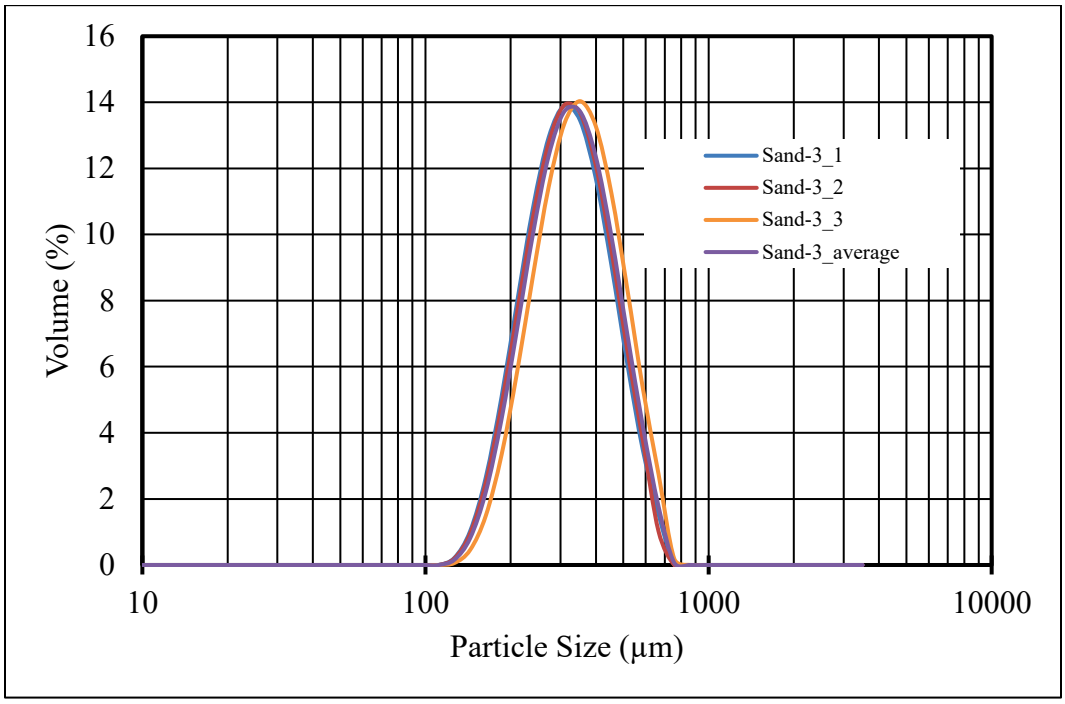

Figure A-6. Particle size analysis of hematite.

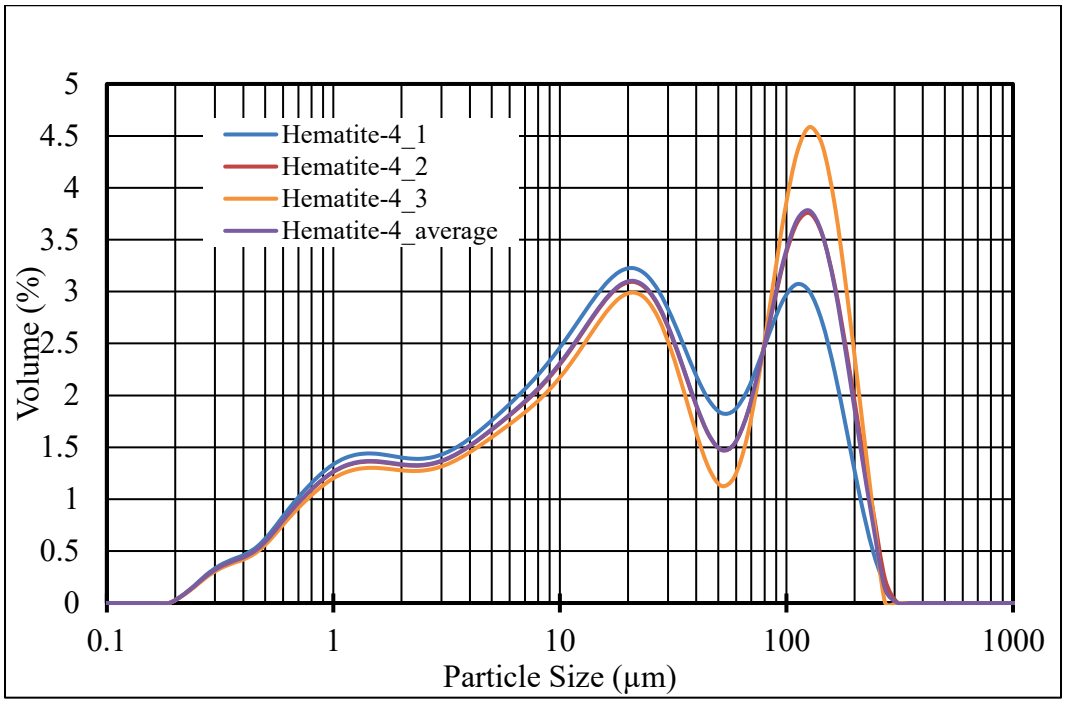

Figure A-7. Particle size analysis of magnetite.

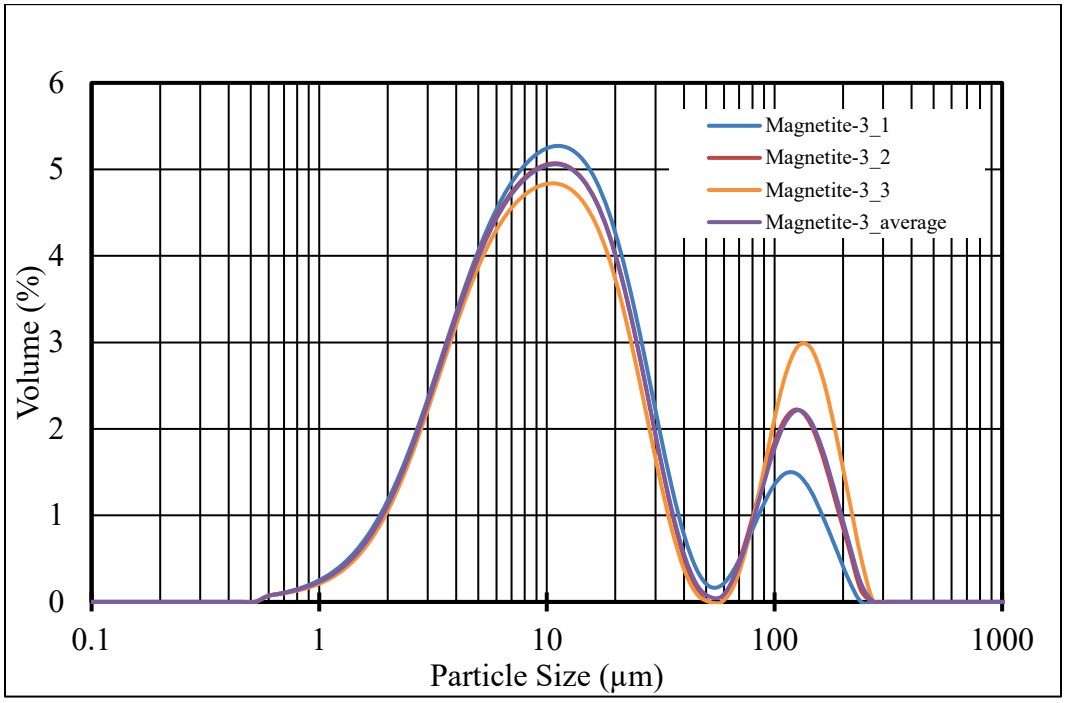

Figure A-8. XRD pattern of hematite.

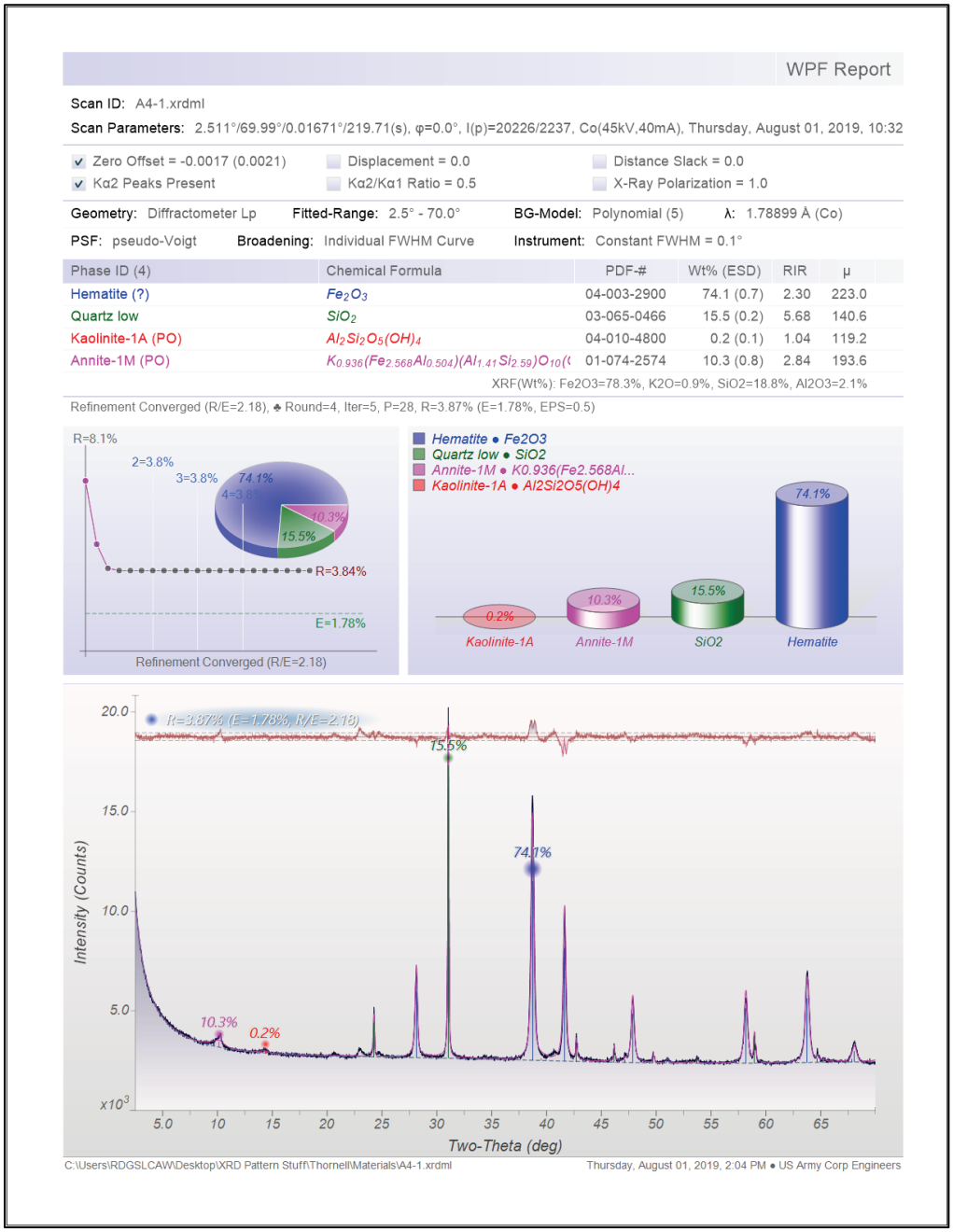

Figure A-9. XRD pattern of hematite.

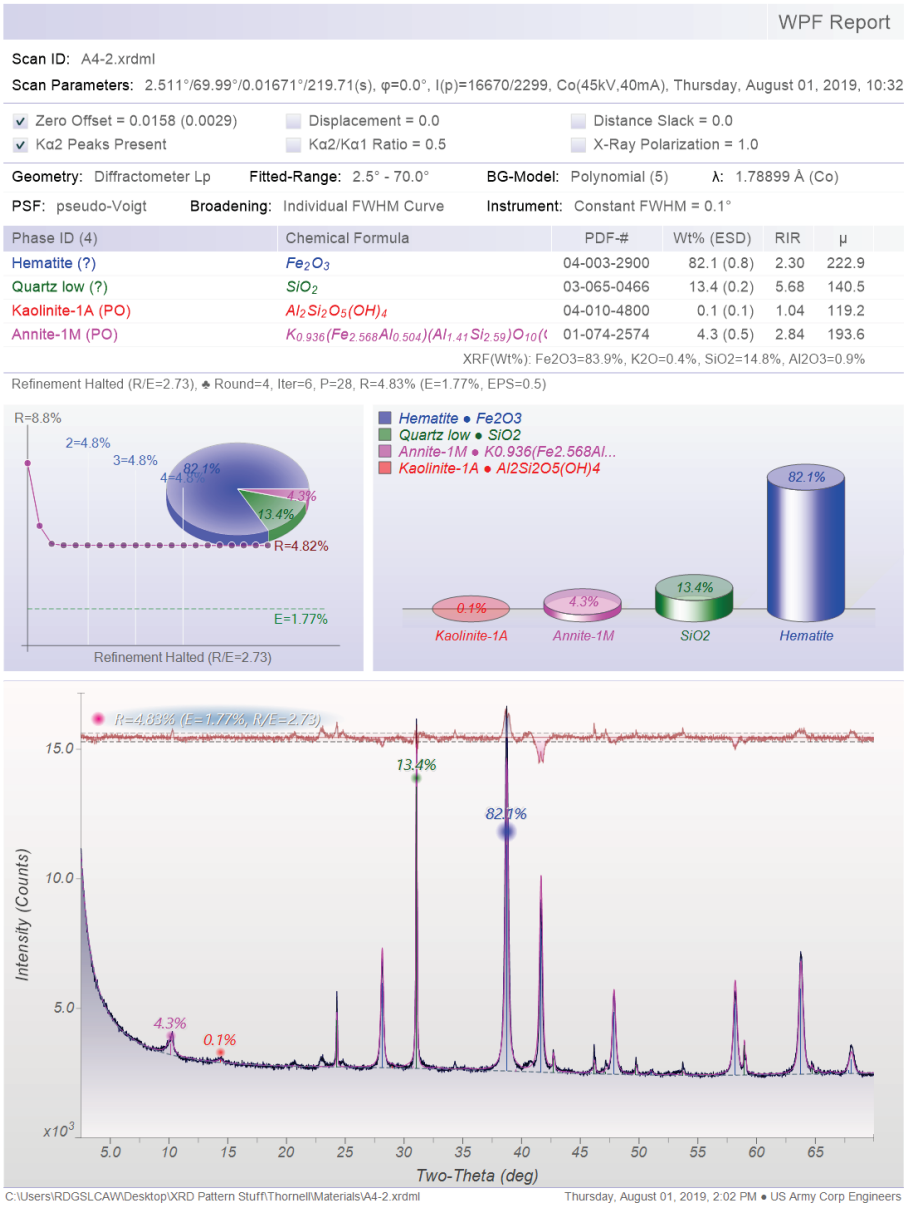

Figure A-10. XRD pattern of magnetite.

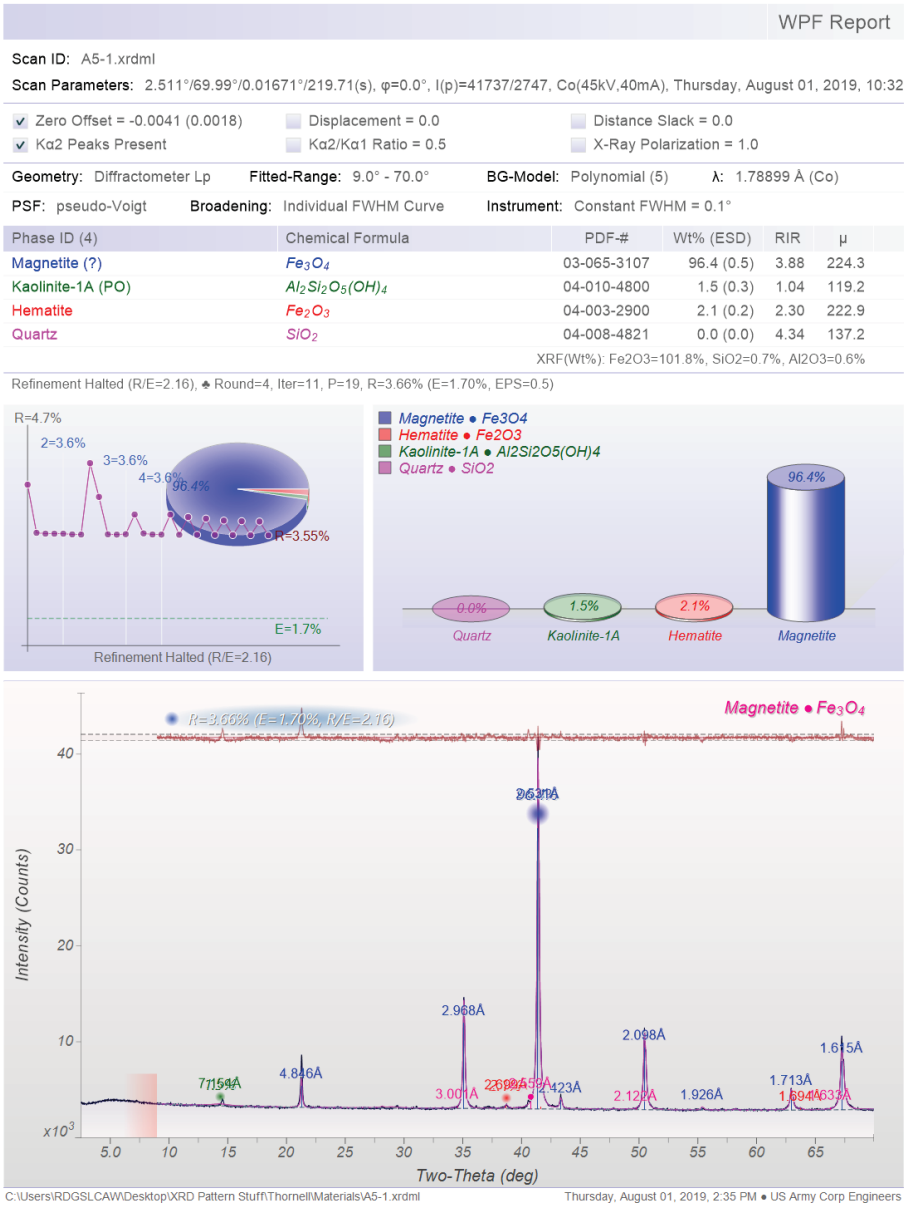

Figure A-11. XRD pattern of magnetite.

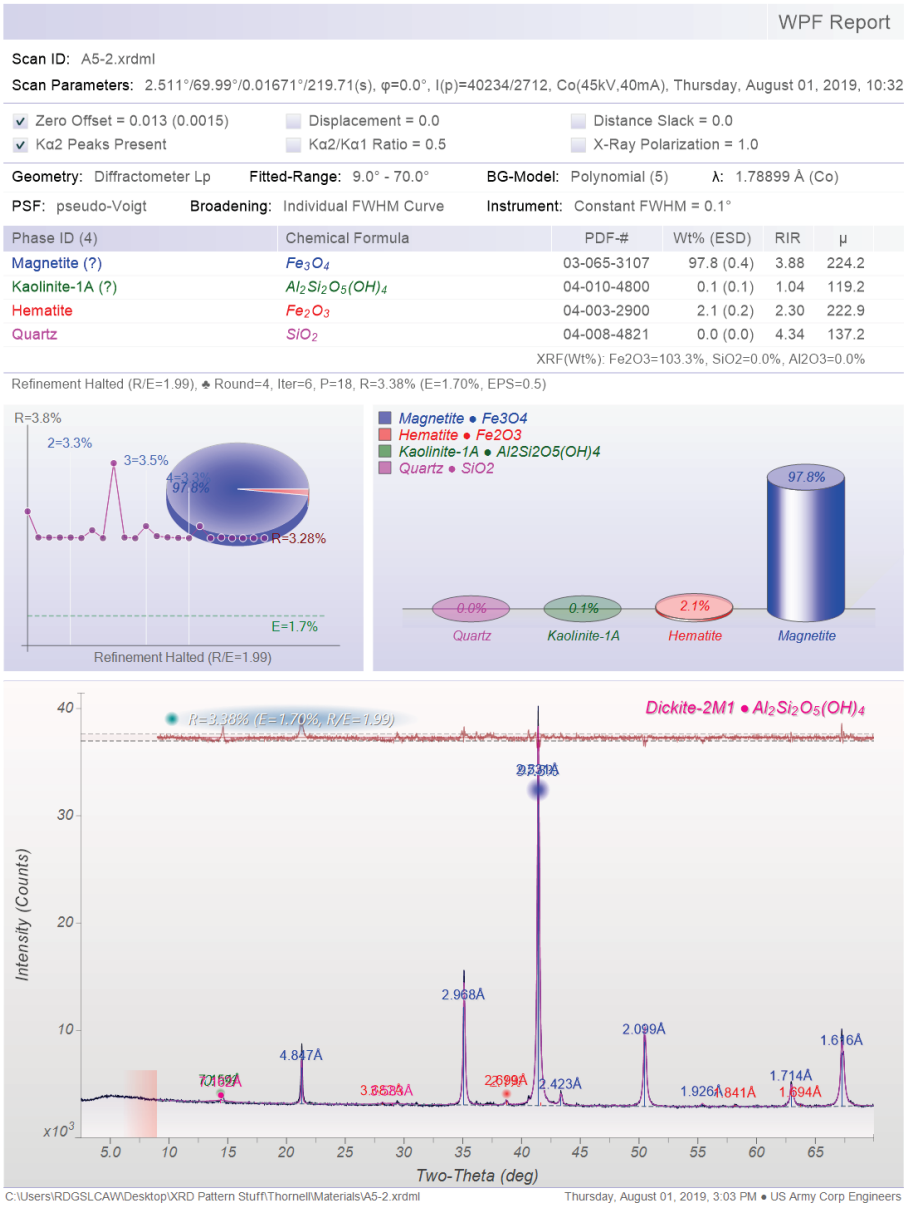

Figure A-12. XRD pattern of kaolinite.

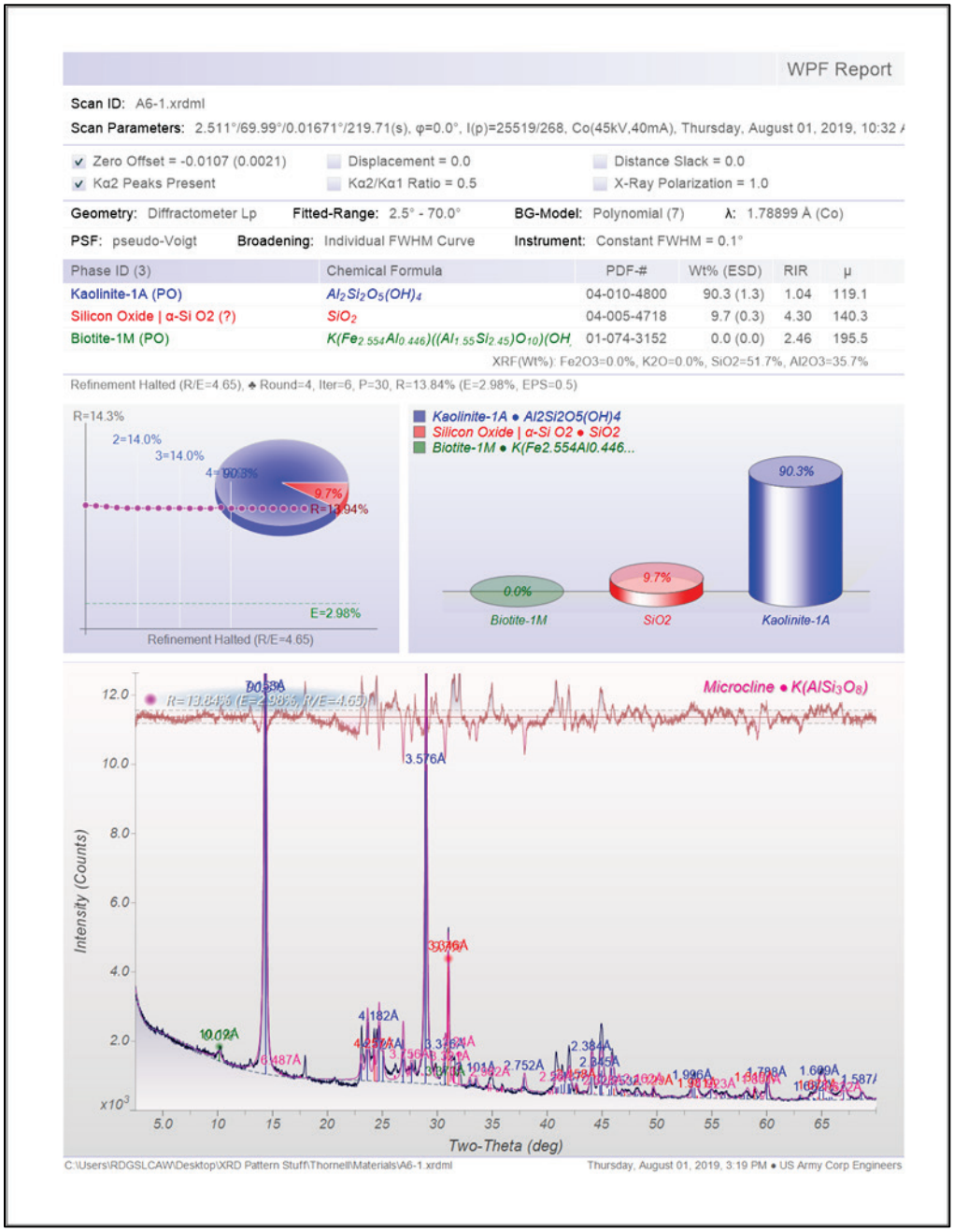

Figure A-13. XRD pattern of kaolinite.

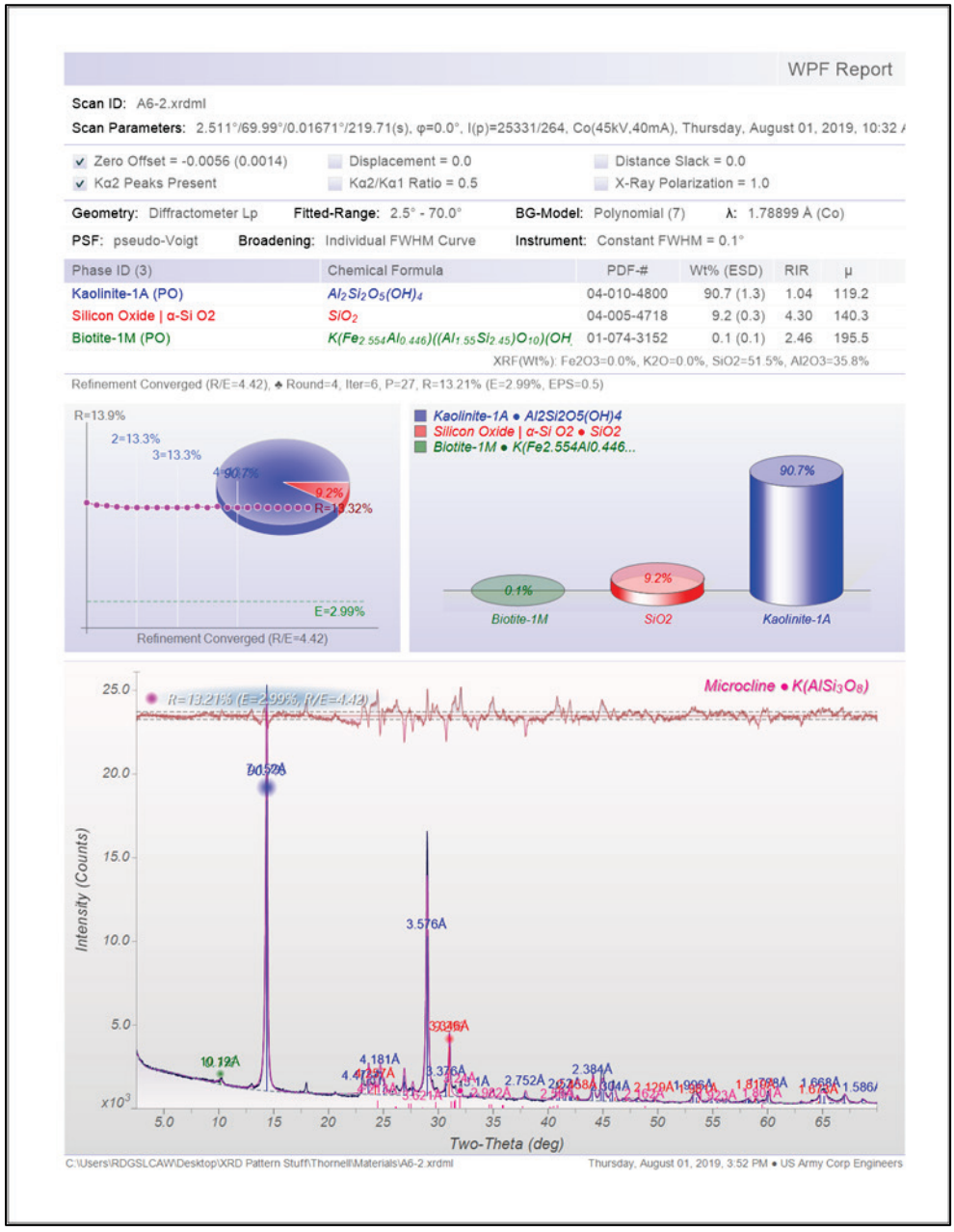

Figure A-14. XRD pattern of sand.

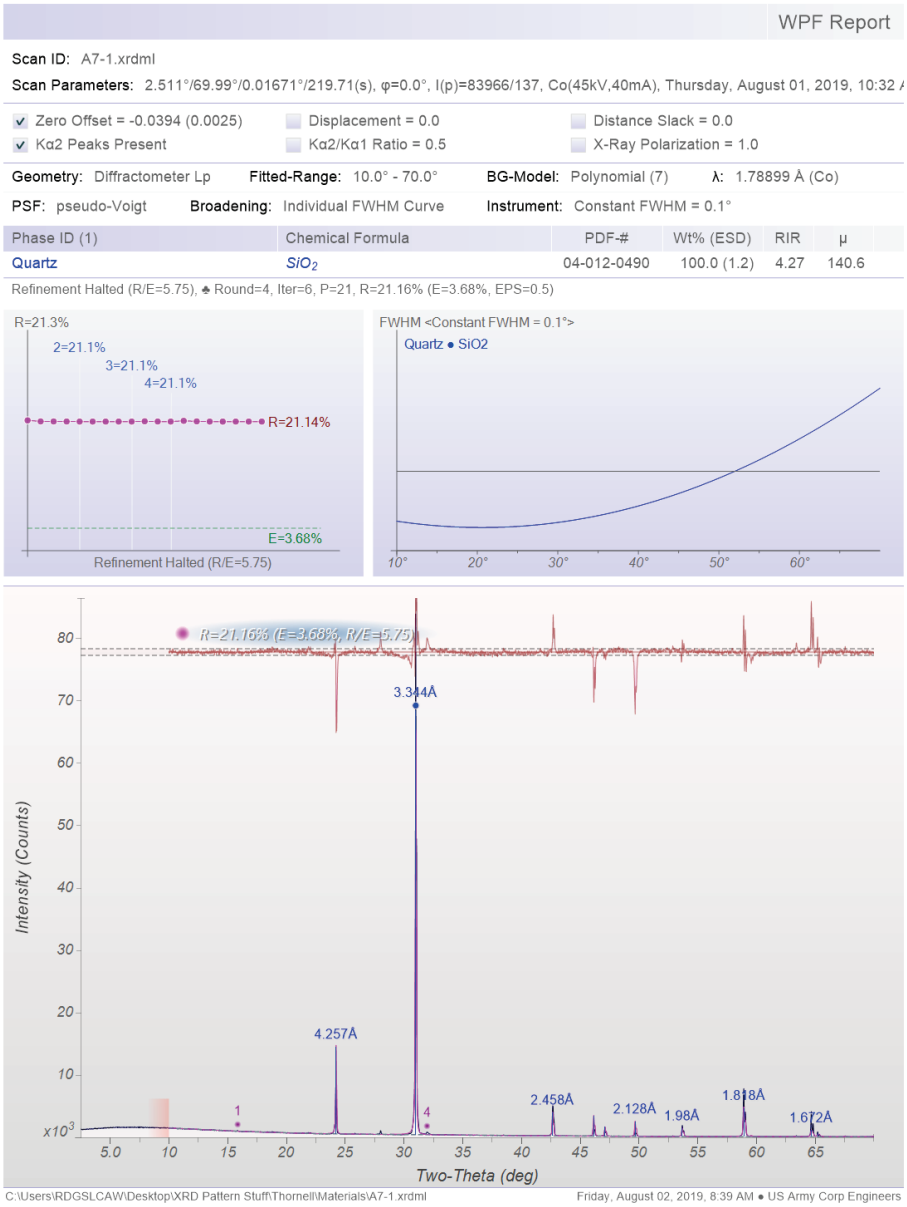

Figure A-15. XRD pattern of sand.

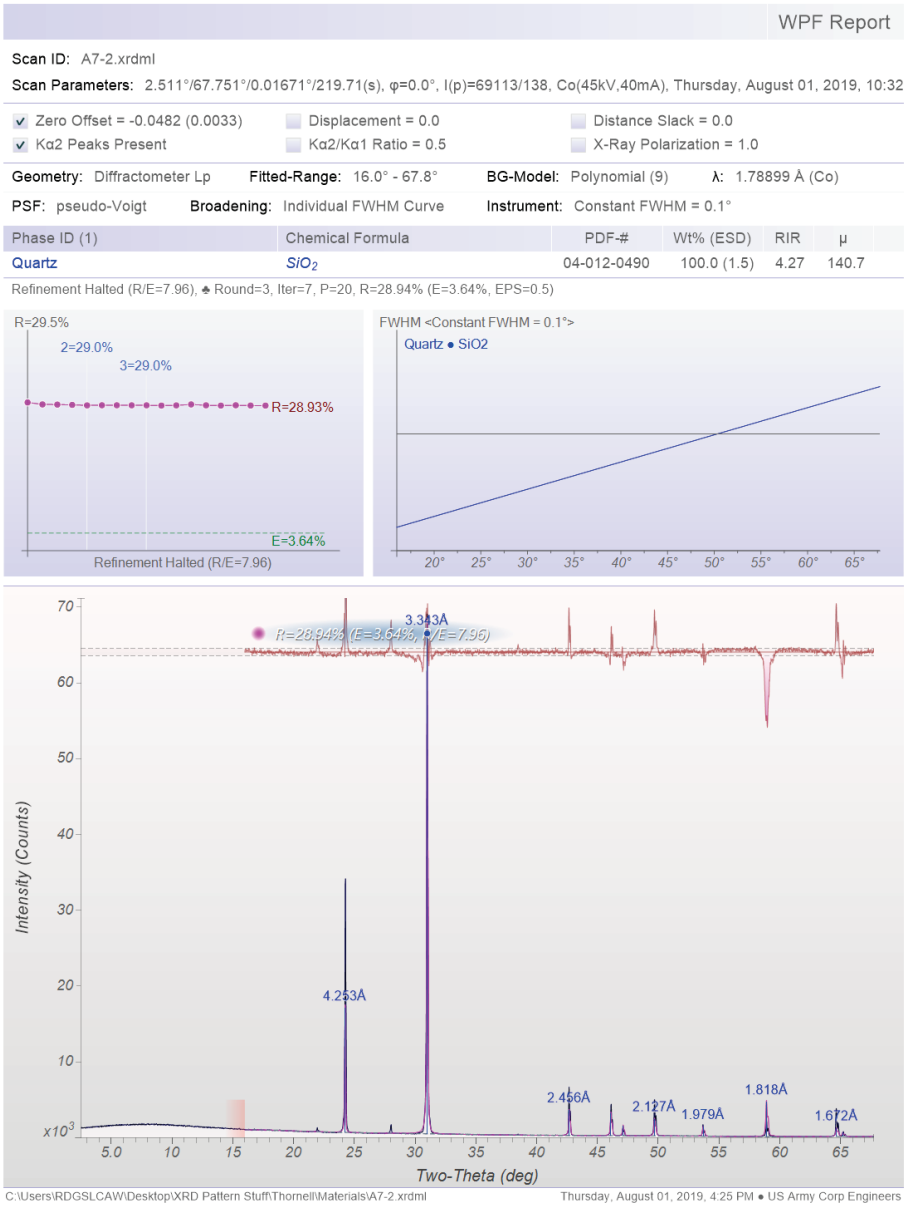

Appendix B: Slurry-Based MRCM Model Fitting

Table B-1. Fitting parameters of HB models for slurry-based MRCMs.

Slurry Composition	Magnetic Field	0 T	0.1 T	0.3 T	0.5 T	1 T
20 wt. % CIP/ 40 wt. % Kaolinite	t_y	125.48	705.98	4019.27	6421.56	10005
	K	2.49	18.93	33.08	17.47	1256.76
	n	0.98	0.87	0.74	0.91	0.21
30 wt. % CIP/ 30 wt. % Kaolinite	t_y	36.34	1172.7	5402.1	6607.1	15119
	K	1.26	0.68	39.32	8.44	26.05
	n	0.95	1.25	0.69	1.05	0.86
40 wt. % CIP/ 20 wt. % Kaolinite	t_y	4.72	1770.28	8293.65	10654.8	15440.8
	K	2.44	52.79	15.56	11.58	36.78
	n	0.73	0.39	0.86	1.08	0.76

Appendix C: X-Ray Diffraction of Untreated and Treated NIST Bauxite Samples

Figure C-1. XRD pattern of as-received Arkansas bauxite.

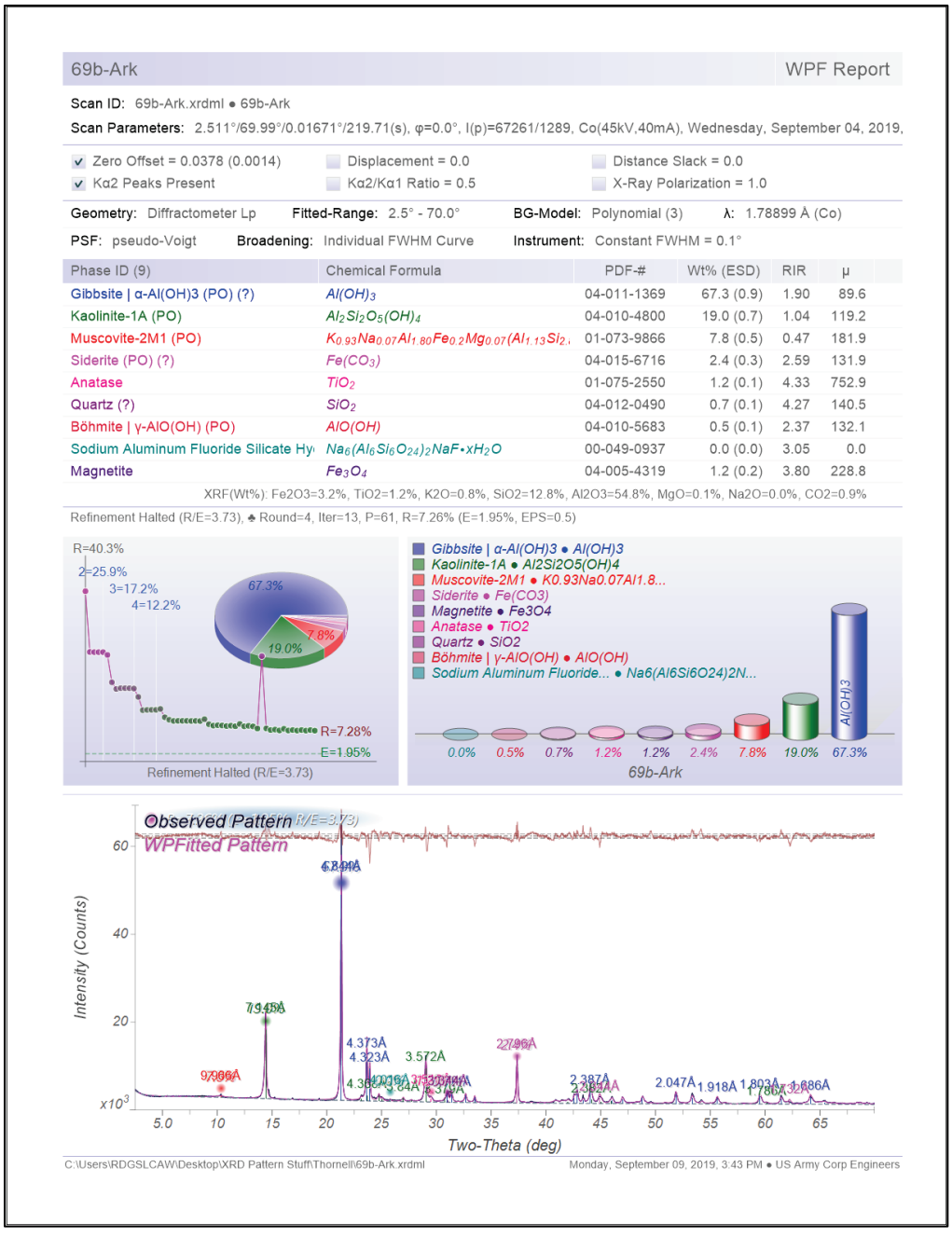

Figure C-2. XRD pattern of treated Arkansas bauxite.

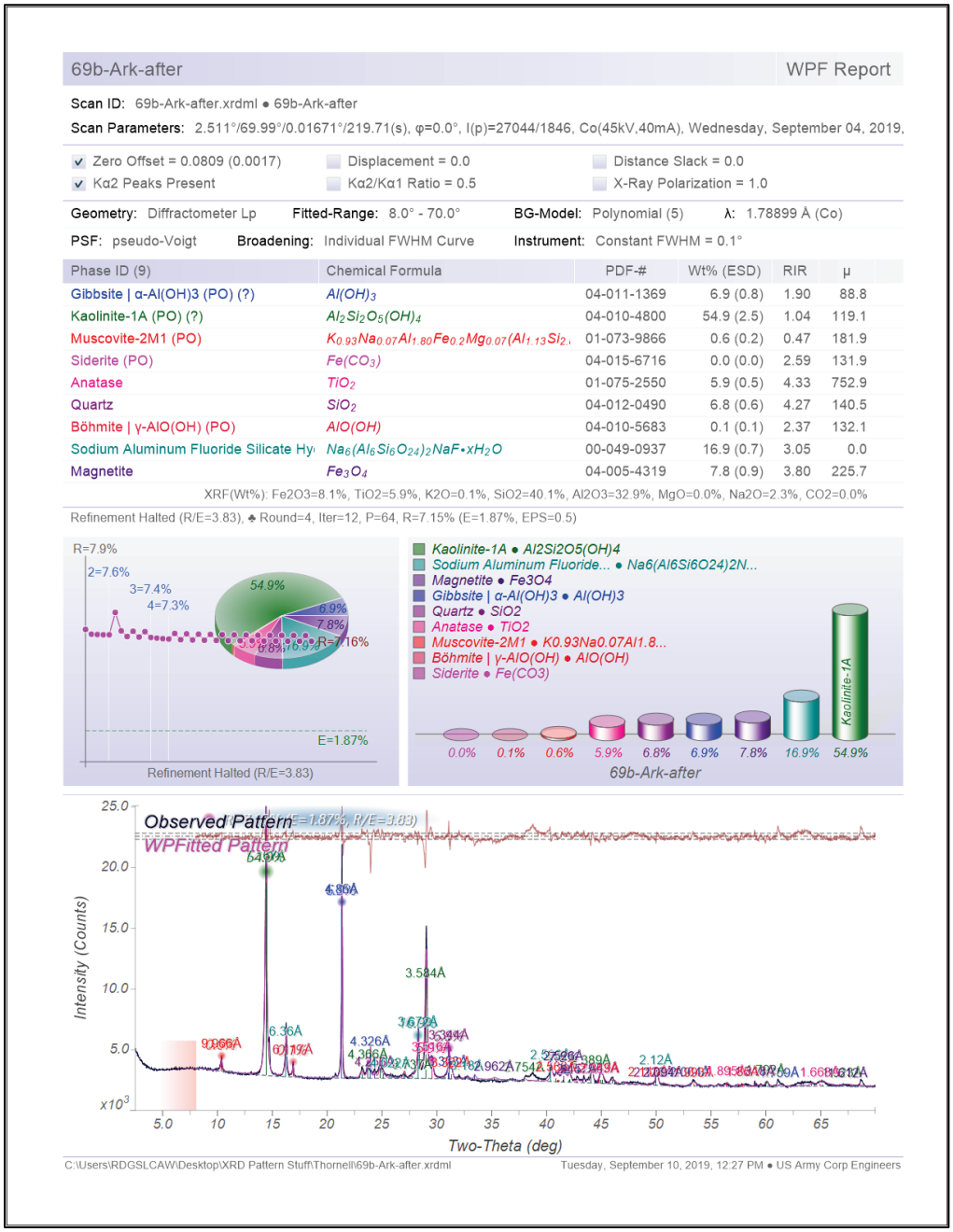

Figure C-3. XRD pattern of as-received Jamaican bauxite.

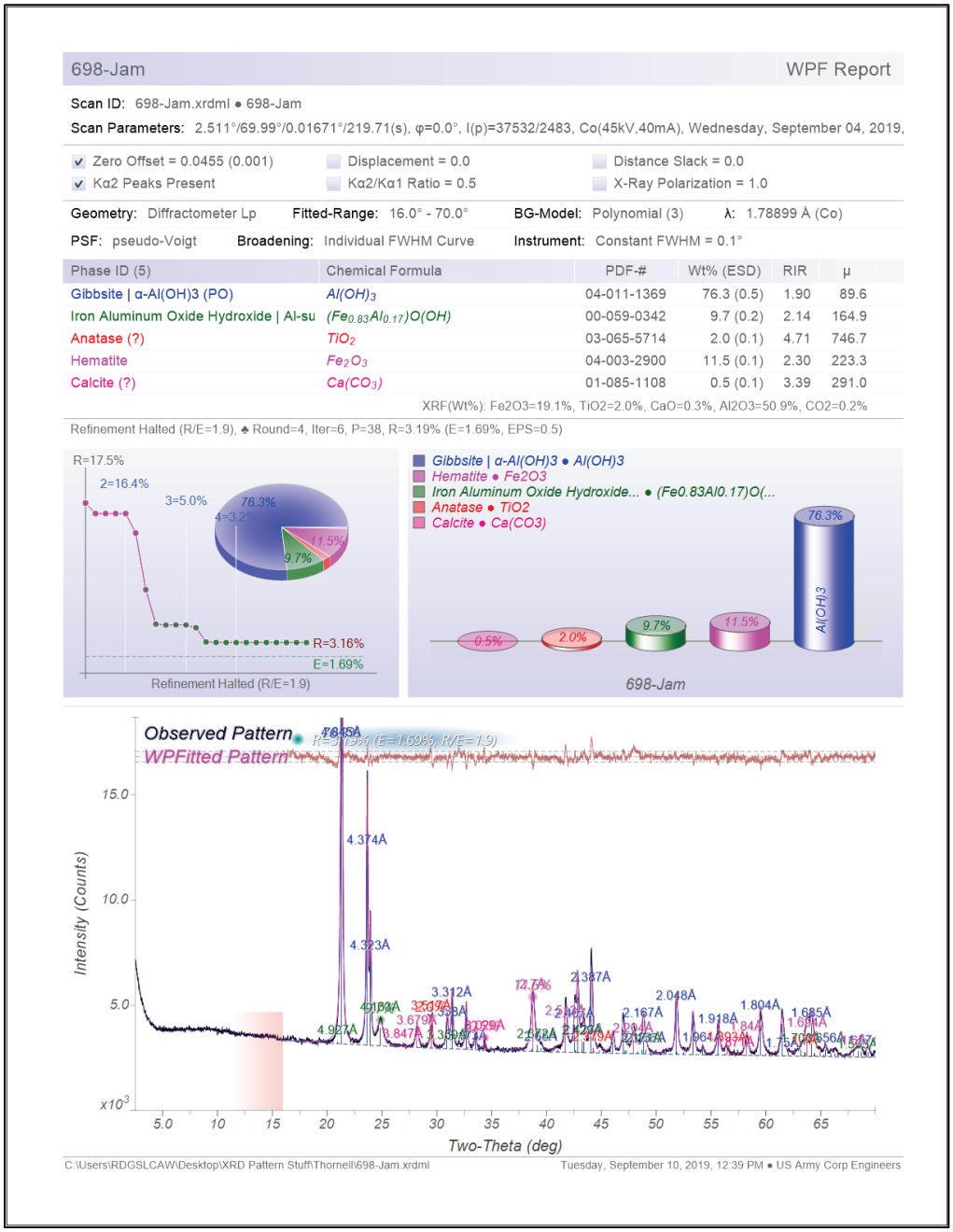

Figure C-4. XRD pattern of treated Jamaican bauxite.

Figure C-5. XRD pattern of as-received Dominican bauxite.

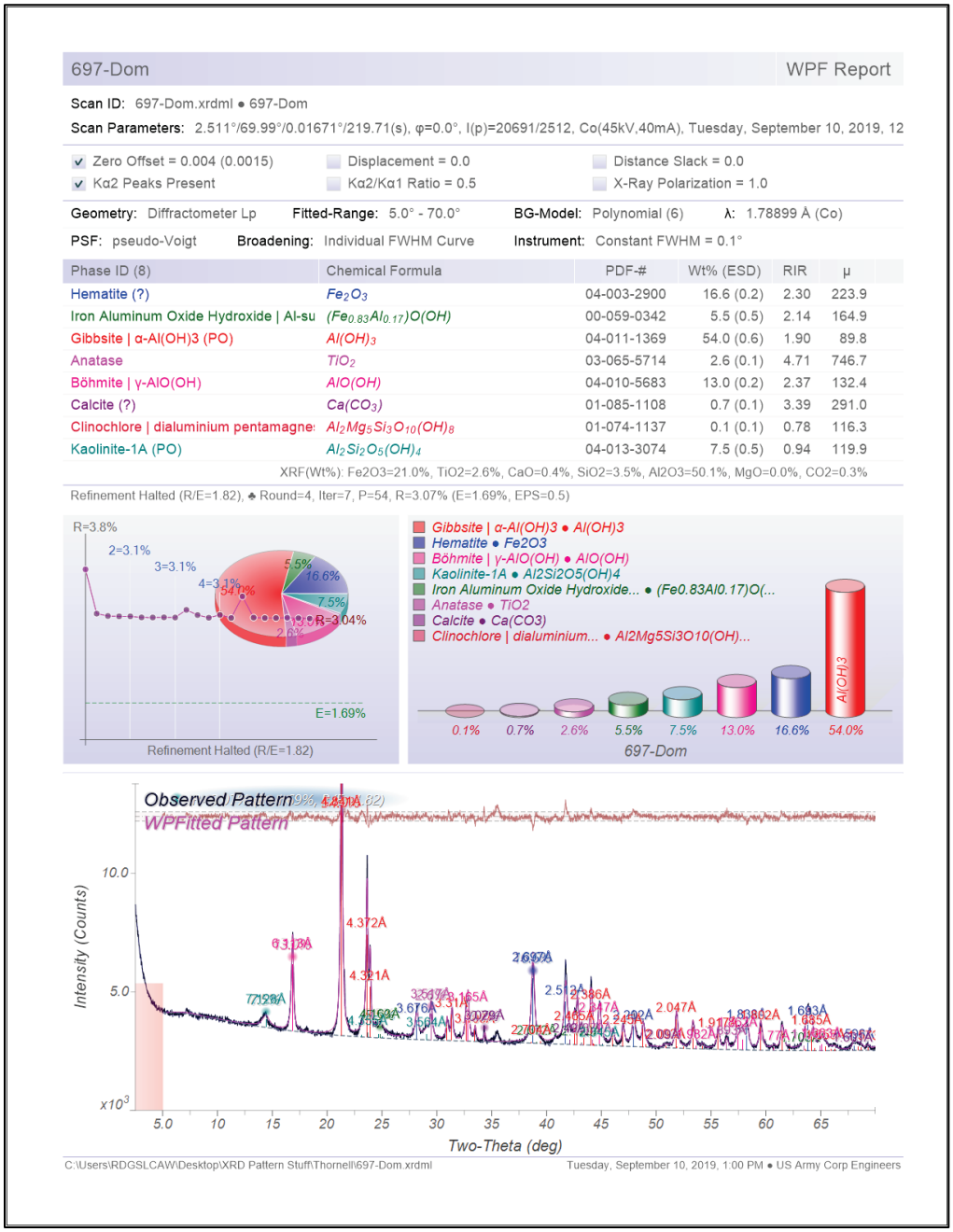

Figure C-6. XRD pattern of treated Dominican bauxite.

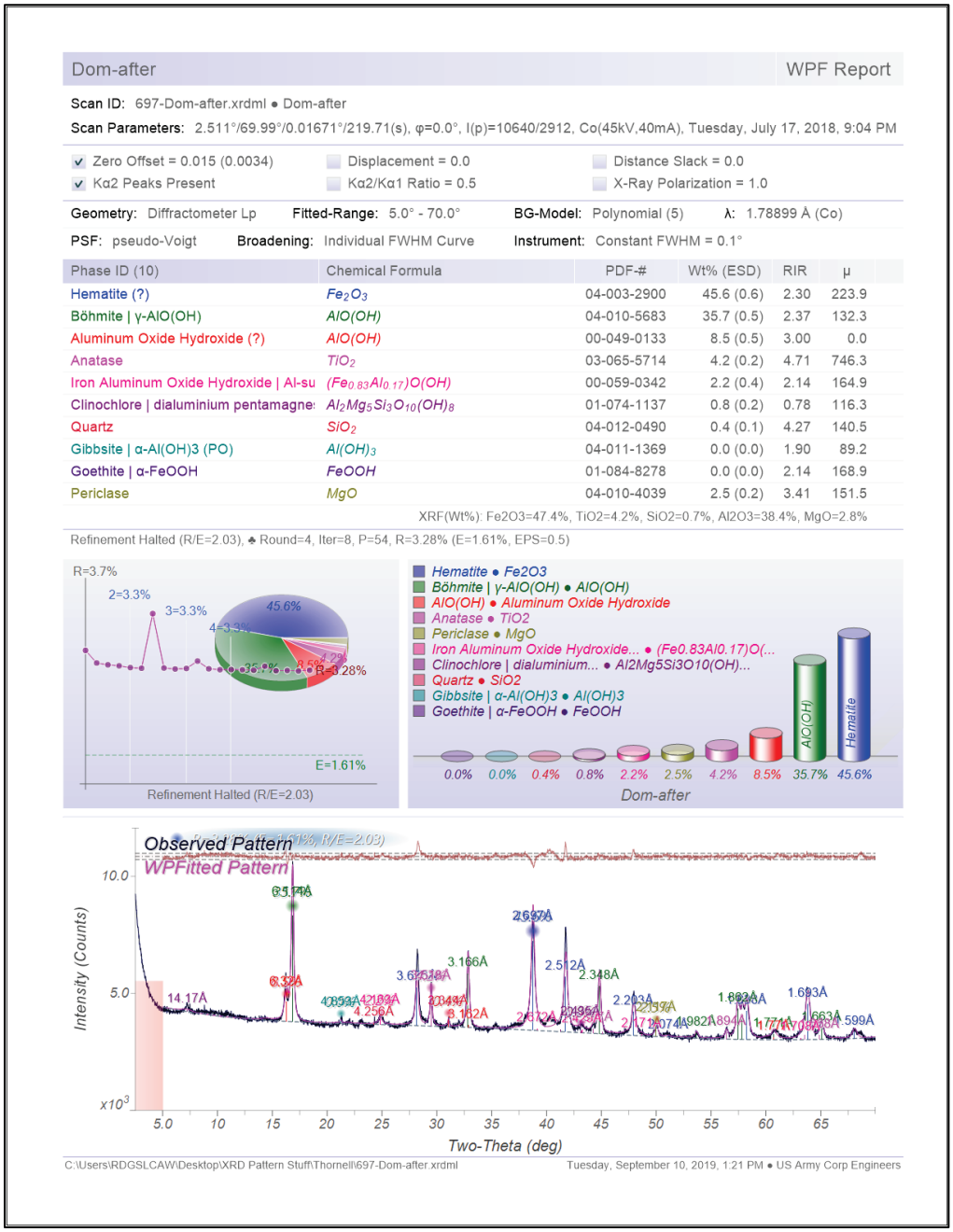

Figure C-7. XRD pattern of as-received Surinam bauxite.

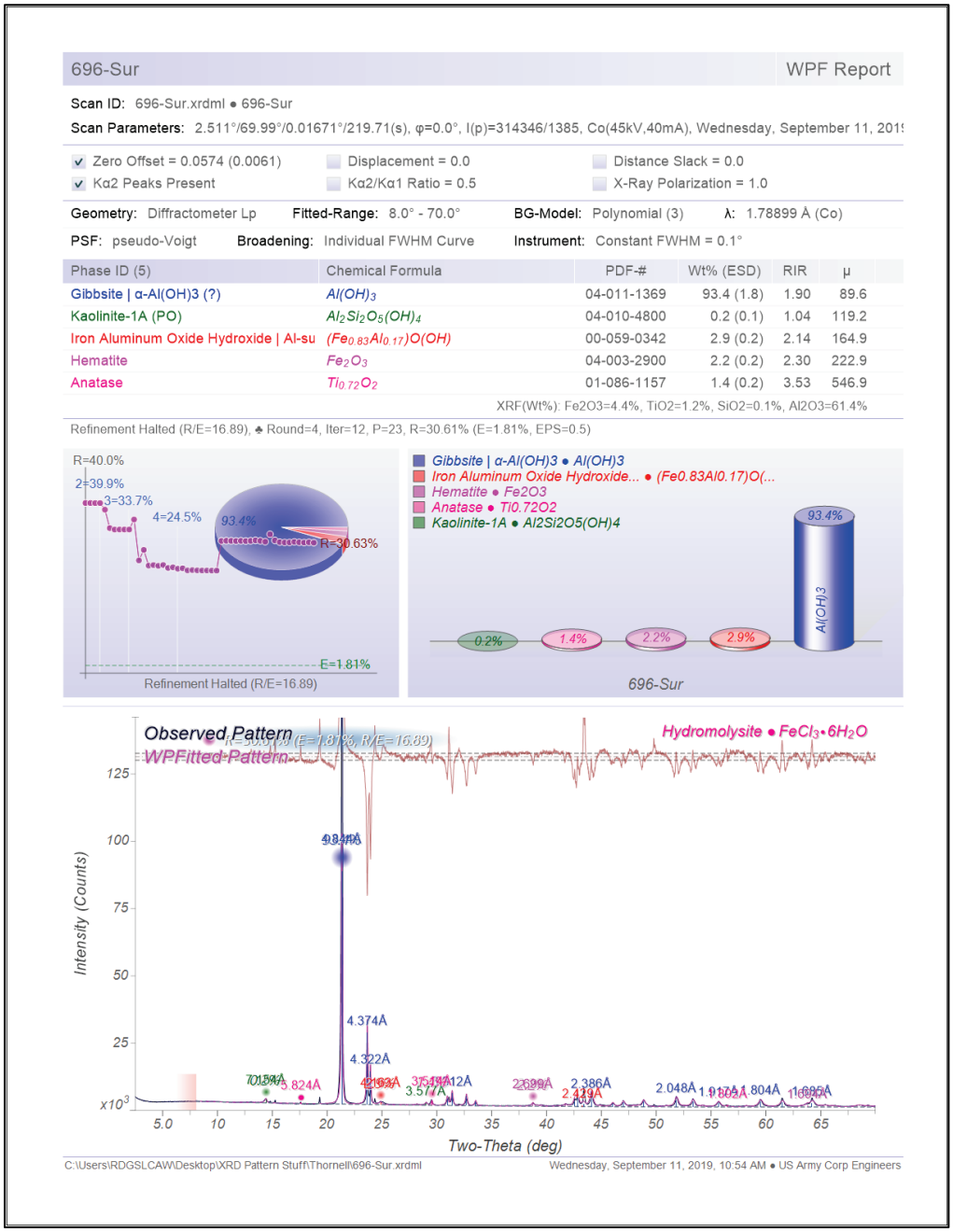

Figure C-8. XRD pattern of treated Surinam bauxite.

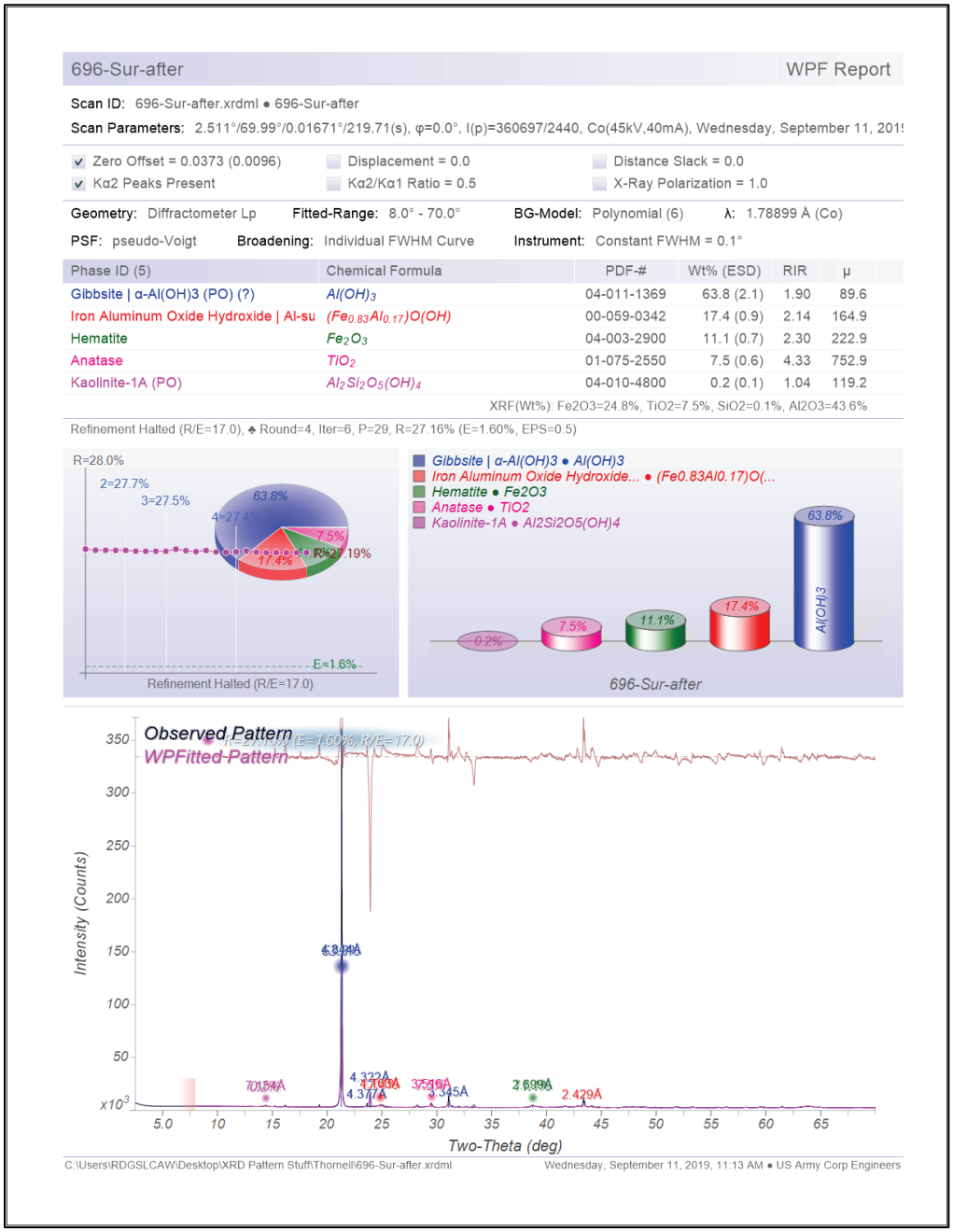

Figure C-9. XRD pattern of as-received Australian bauxite.

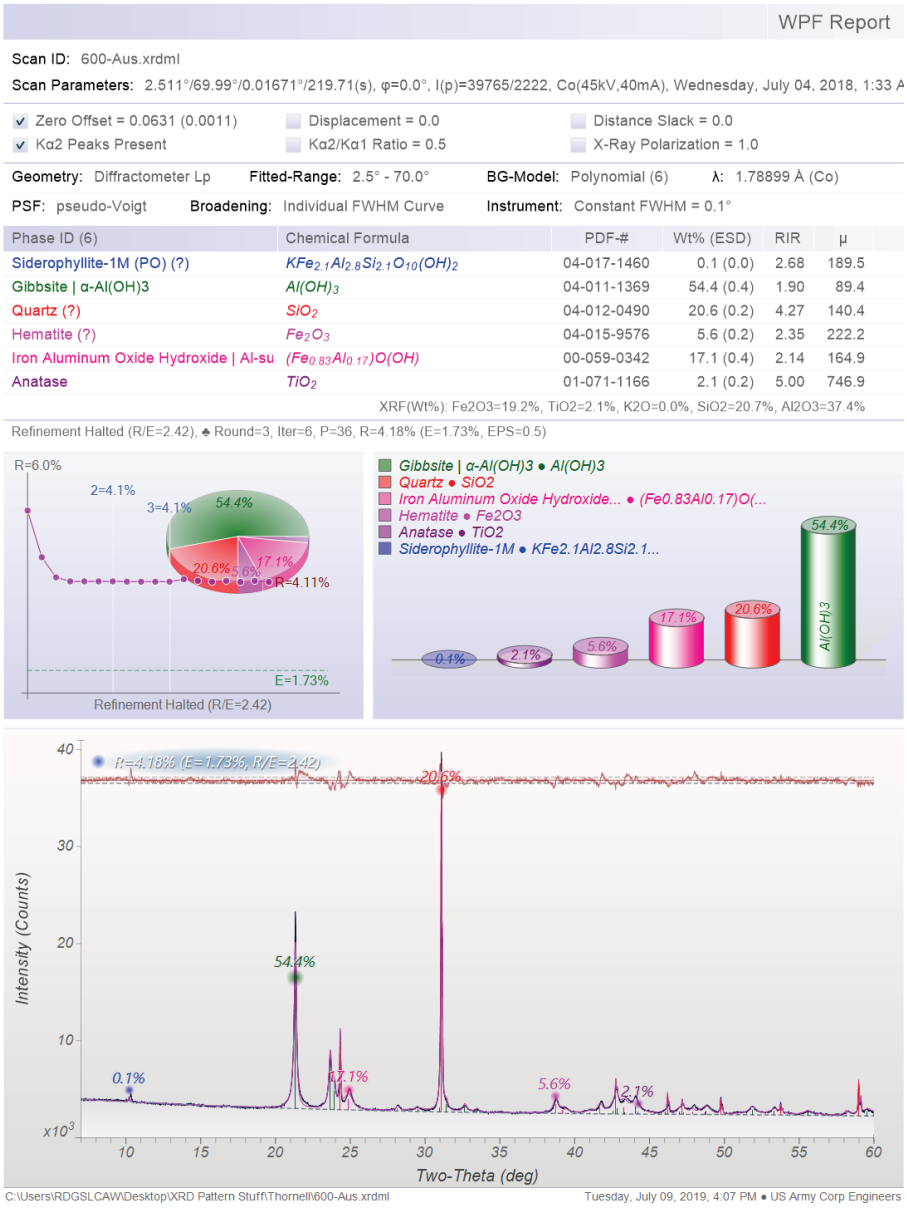

Figure C-10. XRD pattern of treated Australian bauxite.

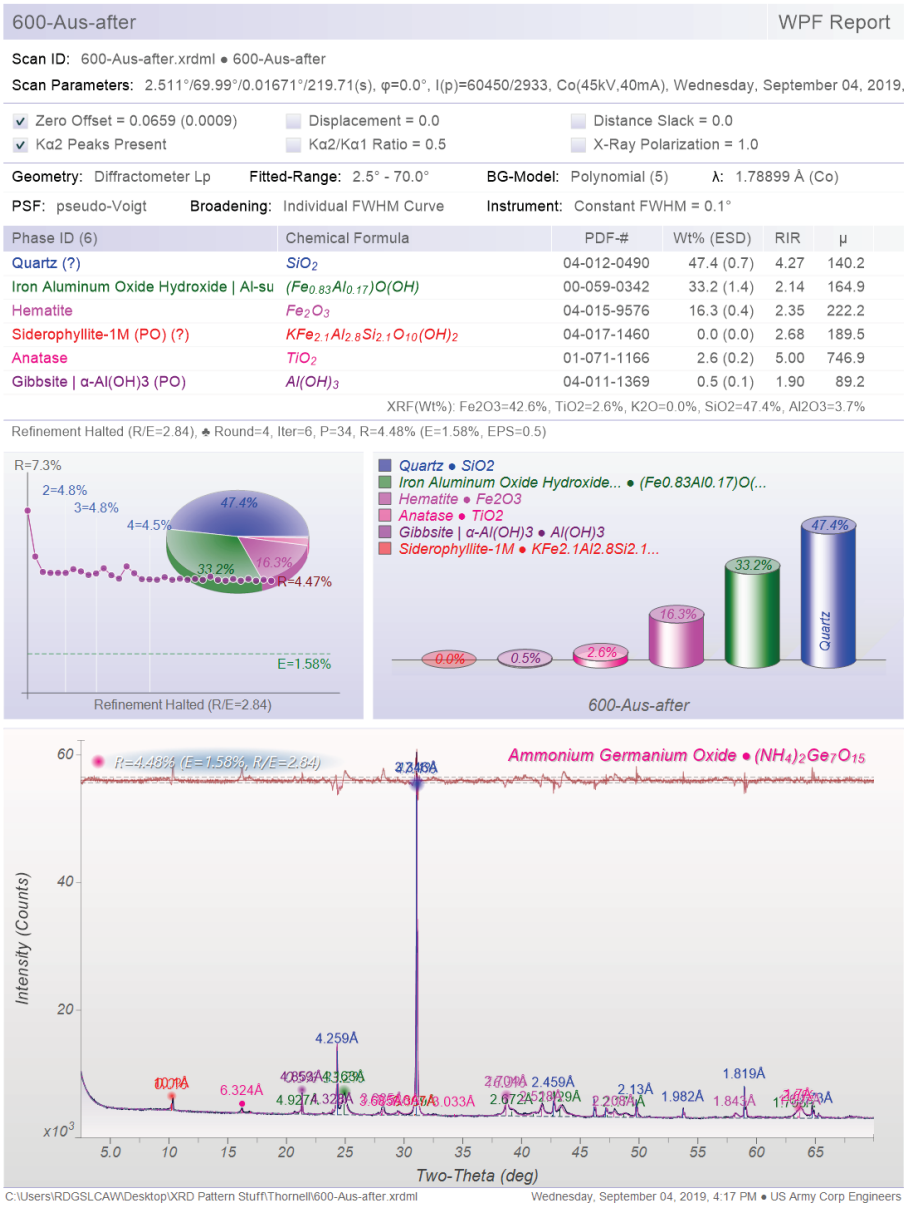

Unit Conversion Factors

Multiply	By	To Obtain
centipoises	0.001	pascal seconds
degrees Fahrenheit	(F-32)/1.8	degrees Celsius
inches	0.0254	meters
microns	1.0 E-06	meters
mils	0.0254	millimeters
pounds (force)	4.448222	newtons
pounds (force) per foot	14.59390	newtons per meter
pounds (force) per inch	175.1268	newtons per meter
pounds (force) per square foot	47.88026	pascals
pounds (force) per square inch	6.894757	kilopascals
pounds (mass)	0.45359237	kilograms
pounds (mass) per cubic foot	16.01846	kilograms per cubic meter
pounds (mass) per cubic inch	2.757990 E+04	kilograms per cubic meter
pounds (mass) per square foot	4.882428	kilograms per square meter
pounds (mass) per square yard	0.542492	kilograms per square meter
tons (force)	8,896.443	newtons
tons (force) per square foot	95.76052	kilopascals

Acronyms and Abbreviations

CIP	carbonyl iron particles
DHR	Discovery Hybrid Rheometer
emu	magnetic moment
G’	storage modulus
G”	loss modulus
HB	Herschel-Bulkley
IEP	iron electrolytic powder
IFA	iron for analysis
LVE	linear viscoelastic regime
MCRM	magnetorheological composite material
micro CT	micro-computed tomography
MR	magnetorheological
MRE	magnetorheological elastomers
NIST	National Institute of Standards and Technology
SBR	polystyrene-butadiene rubber
SEBS	styrene-ethylene-co-butylene-styrene
SEM	scanning electron microscopy
TGA	thermogravimetric analyses
VSM	vibrating sample magnetometer
XRD	X-ray diffraction

REPORT DOCUMENTATION PAGE

Form Approved
OMB No. 0704-0188

1. REPORT DATE	2. REPORT TYPE	3. DATES COVERED *(From - To)*
November 2020	Final Report	

4. TITLE AND SUBTITLE
Magnetorheological Composite Materials (MRCMs) for Instant and Adaptable Structural Control

5a. CONTRACT NUMBER

5b. GRANT NUMBER

5c. PROGRAM ELEMENT NUMBER

6. AUTHOR(S)
Travis L. Thornell, Charles A. Weiss, Jr., Sarah L. Williams,
Jennifer A. Jefcoat, Zackery B. McClelland, Todd S. Rushing, and Robert D. Moser

5d. PROJECT NUMBER
61102/T22/01

5e. TASK NUMBER

5f. WORK UNIT NUMBER

7. PERFORMING ORGANIZATION NAME(S) AND ADDRESS(ES)
Geotechnical and Structures Laboratory
U.S. Army Engineer Research and Development Center
3909 Halls Ferry Road
Vicksburg, MS 39180-6199

8. PERFORMING ORGANIZATION REPORT NUMBER
ERDC/GSL TR-20-36

9. SPONSORING/MONITORING AGENCY NAME(S) AND ADDRESS(ES)
U.S. Army Corps of Engineers
Washington, DC 20314-1000

10. SPONSOR/MONITOR'S ACRONYM(S)

11. SPONSOR/MONITOR'S REPORT NUMBER(S)

12. DISTRIBUTION/AVAILABILITY STATEMENT
Approved for public release; distribution is unlimited.

13. SUPPLEMENTARY NOTES

14. ABSTRACT
Magnetic responsive materials can be used in a variety of applications. For structural applications, the ability to create tunable moduli from relatively soft materials with applied electromagnetic stimuli can be advantageous for light-weight protection. This study investigated magnetorheological composite materials involving carbonyl iron particles (CIP) embedded into two different systems. The first material system was a model cementitious system of CIP and kaolinite clay dispersed in mineral oil. The magnetorheological behaviors were investigated by using parallel plates with an attached magnetic accessory to evaluate deformations up to 1 T. The yield stress of these slurries was measured by using rotational and oscillatory experiments and was found to be controllable based on CIP loading and magnetic field strength with yield stresses ranging from 10 to 104 Pa. The second material system utilized a polystyrene-butadiene rubber solvent-cast films with CIP embedded. The flexible matrix can stiffen and become rigid when an external field is applied. For CIP loadings of 8% and 17% vol %, the storage modulus response for each loading stiffened by 22% and 74%, respectively.

15. SUBJECT TERMS
Composite materials, Magnetic fluids, Materials—Evaluation, Materials—Magnetic properties, Smart materials

16. SECURITY CLASSIFICATION OF:			17. LIMITATION OF ABSTRACT	18. NUMBER OF PAGES	19a. NAME OF RESPONSIBLE PERSON
a. REPORT	b. ABSTRACT	c. THIS PAGE			Travis L. Thornell
Unclassified	Unclassified	Unclassified	SAR	85	19b. TELEPHONE NUMBER *(Include area code)* 601-634-4234